Radboud University Nijmegen

Faculty of Science

Probing Dark Matter Bound States at Electron-Positron Colliders

Thesis MSc Particle and Astrophysics

Author:
Colin Saba

Supervisor:
dr. S. Westhoff

Second reader:
dr. H. Schoorlemmer

August 21, 2025

Abstract

In this thesis we investigated dark matter bound states in a minimal dark sector consisting of a dark fermion and a dark photon. We introduced a kinetic mixing term in the Lagrangian allowing coupling of the dark sector to the Standard Model. From this we derived expressions for the production and decay rates of dark matter bound states in the non-relativistic limit using quantum field theory. The non-relativistic wave functions required for these rates were obtained by implementing a numerical solver for the radial Schrödinger equation with a Yukawa potential. This method was validated against known systems, including the hydrogen atom and the harmonic oscillator. We applied the formalism to the Belle II and FCC-ee experiments. For realistic benchmark parameters, we identified distinctive experimental signatures: displaced electron-positron pairs at both Belle II and FCC-ee. These results highlight the potential of future experiments to observe bound states in dark sectors.

Contents

1 Introduction

In 1933 a Swiss astronomer by the name of Fritz Zwicky was studying the Coma cluster, thousands of galaxies about 300 million lightyears away from Earth. Zwicky applied the virial theorem to the measured speed of galaxies within the cluster [1]. In this way, Zwicky could estimate the mass of the Coma cluster. He also estimated the mass by looking at the light coming from it. Using relations between mass and luminosity, he found the mass of the cluster to be smaller than that of his estimate with the virial theorem, implying there is some unseen form of mass present. In his paper from 1933 he introduced the term "dunkle Materie", which is the first mention of dark matter. After this discovery, it still took decades before the existence of dark matter was generally accepted.

The second piece of evidence came from Vera Rubin and Kent Ford, who observed that stars in spiral galaxies orbit the center with roughly the same speed regardless of their distance to the center [2]. From Newtonian physics one would predict the speed to decrease with distance. This discrepancy with Newtonian physics would be explained if there is some new unseen form of mass that extends within the galaxy to give rise to the observed rotation curves. This, again, implies the existence of dark matter, now at a much smaller scale. By the early 1980s, the concept of dark matter, being a new unseen form of matter, was generally accepted.

The true nature of dark matter is currently an open problem in physics. Perhaps one of the most pressing problems. For decades, people have been studying it. From the particle physics community there have been plenty of theories trying to describe dark matter. This often comes with the introduction of a new particle. These particles do not come out of nowhere, the possibility of being a dark matter candidate often being serendipitous. For example, the axion, which was introduced to solve the strong CP problem [3], or right-handed neutrinos, which, given the symmetries of the standard model, have no reason to be believed not to exist [4]. WIMP-like particles come from supersymmetry. These are also not just plain attempts to explain the nature of dark matter; especially WIMPs offer a compelling solution. For example, one may think of the WIMP miracle, which refers to the fact that WIMPs naturally yield the correct relic abundance observed in the universe [5].

A natural question to ask with such new particles is if it is just one, or if it is part of a new dark sector: a Standard Model–like structure that has its own particles and forces. Examples of dark sectors include models with dark photons (new U(1) gauge bosons) that mediate interactions between dark matter particles, models with dark Higgs bosons responsible for symmetry breaking in the dark sector, and hidden valley models with rich dark dynamics [6, 7]. Interestingly, such dark sectors could offer a rich new phenomenology. Just as in the standard model where we do not just have free electrons or other particles, composite particles like positronium, quarkonium and protons form. Similarly, a dark sector could also host bound states. So far, dark sector models are often not investigated for bound state effects.

In this work, we explore bound states within the context of a new dark sector. We derive a theoretical framework to compute the production and decay rates of these states in the non-relativistic limit in Section 3. To solve for the wave functions of dark matter bound states in Section 4, we employ numerical methods. We apply this framework to study bound state formation at two electron-positron colliders: Belle II (Section 6) and FCC-ee (Section 7). For these experiments, we identify characteristic experimental signatures that could guide future searches for such states.

2 The Dark Sector

To describe bound states in a dark sector, we first need to introduce such a dark sector.

2.1 A New U(1) Symmetry

The dark sector we will examine in this work exists of a new dark fermion charged under a new U(1) gauge symmetry whose force carrier is a massive vector boson. This model is interesting in the sense that it is the minimal extension of the Standard Model in which we can support bound states. The Lagrangian of this new sector is given by [8]

$$\mathcal{L} = \mathcal{L}_{SM} + \bar{\chi} i\gamma^{\mu}\left(\partial_{\mu} - ig_D\hat{V}_{\mu}\right)\chi - m_{\chi}\bar{\chi}\chi - \frac{1}{4}\hat{V}^{\mu\nu}\hat{V}_{\mu\nu} + \frac{1}{2}m_V^2\hat{V}^{\mu}\hat{V}_{\mu}. \tag{2.1}$$

The particle content of the dark sector is the fermion χ, its anti-particle $\bar{\chi}$, and the new mediator represented by $\hat{V}_{\mu}$, which is often called the dark photon. The dark photon is a massive gauge boson. The mass term of $\hat{V}_{\mu}$ in the Lagrangian is assumed to be introduced via a Higgs-mechanism or a Stueckelberg-mechanism; see, for example, Ref. [9]. We will not deal with that here, but we will simply work with the dark photon with mass $m_V \neq 0$. The hats in the Lagrangian indicate gauge eigenstates. These will turn out to be different form the mass eigenstates, which we discuss later. From the Lagrangian we may observe that the model is described by three parameters, that is, the mass of the new fermion (m_{χ}), the mass of the dark photon (m_V) and the coupling constant g_D. The latter we may write as $g_D = \sqrt{4\pi\alpha_D}$, and we will work with α_D as our third parameter.

We are interested in examining the darkonium states ($\chi\bar{\chi}$) at experiment. For this we assume a small interaction between the new dark sector and the Standard Model. This is done via kinetic mixing.

2.2 Kinetic Mixing

Kinetic mixing will allow for the dark sector to couple to the Standard Model. Consequently, darkonium can be produced directly from the collision of Standard Model particles.

To build in such an interaction we must include in our Lagrangian (Equation 2.1) a new term [8, 10]

$$\mathcal{L} \supset -\frac{\epsilon'}{2}\hat{B}^{\mu\nu}\hat{V}_{\mu\nu}. \tag{2.2}$$

This is the kinetic mixing term that allows for an interaction between the dark photon and the Standard Model. $\hat{B}^{\mu\nu}$ here is the field-strength tensor of the hypercharge gauge field, $\hat{V}^{\mu\nu}$ is that of the dark photon. Before we look at what this implies for the interactions we first note that this is the only way to include a renormalizable, gauge-invariant interaction between the Standard Model and a new abelian gauge boson. The reason is as follows. Both $\hat{B}^{\mu\nu}$ and $\hat{V}^{\mu\nu}$ correspond to field-strength tensors of $U(1)$ symmetries, $U(1)_Y$ and $U(1)_D$ in this case, where the D denotes the dark sector. As these symmetry groups are abelian, their field-strength tensors are invariant under gauge transformations of those groups. Naturally, they are invariant under the other Standard Model gauge symmetries, as the dark photon and the hypercharge gauge boson are uncharged under the other symmetries. Since the mass dimension of ϵ' is zero and this term is gauge invariant under both $U(1)_Y$ and $U(1)_D$, it is the only renormalizable interaction term that can connect the two sectors. However, this term results in off-diagonal kinetic terms, which, after electroweak symmetry breaking, lead to mixing between the dark

photon and the SM photon and Z boson. This requires a field redefinition to bring the kinetic and mass terms into canonical form.

To find out what this does for the interactions between the dark sector and the Standard Model one can follow the argument made in Appendix A of Ref. [10]. There, the explicit rotation to the mass eigenstates is constructed. The resulting, new, interaction terms after field re-definitions and electroweak symmetry breaking are the following

$$\mathcal{L} \supset -e\epsilon Q\bar{f}\gamma^{\mu}fV_{\mu} + \epsilon\tan\theta_w g_D\bar{\chi}\gamma^{\mu}\chi Z_{\mu}, \tag{2.3}$$

where $\epsilon = \epsilon'\cos\theta_w$ and θ_w the weak mixing angle. Now, V_μ, without the hat, represents the mass eigenstate, that is, the physical dark photon. In addition to all the interactions of the Standard Model, and those already present in the dark sector, the introduction of kinetic mixing also allows for a direct coupling between the charged fermions of the Standard Model and a dark photon, and between the dark fermions and the Z-boson. Both interactions are suppressed with a factor of ϵ.

2.3 Parameters of the Model

As mentioned before, the introduced dark sector is characterized by three parameters. We will be interested in the bound states that can form within this dark sector, that is, the $n^{2S+1}L_J$ states of darkonium ($\chi\bar{\chi}$). Here n is the principal quantum number, just as introduced for the hydrogen atom. S is the total spin, L the orbital angular momentum, and J the total angular momentum of the bound state. To describe such bound states, it will be essential to work in the non-relativistic limit. The reason is that this avoids having to work with the Bethe-Salpeter equation for general bound states, which even when employing approximations is difficult to do. The non-relativistic limit here means that the bound state constituents have a relative momentum $|\mathbf{k}|$ much smaller than their mass. In this non-relativistic limit the interaction of the dark sector particles can be described by a Yukawa potential

$$V(r) = -\frac{\alpha_D}{r}e^{-m_V r}. \tag{2.4}$$

To gain some intuition as to when bound states can form, we can make a crude approximation. We can demand the range of the interaction ($\sim m_V^{-1}$) to be greater than the Bohr radius of the bound state ($\sim (\alpha_D m_\chi)^{-1}$). This gives a condition

$$1 \gtrsim \frac{m_V}{\alpha_D m_\chi}. \tag{2.5}$$

The exact condition can be found by solving the Schrödinger equation with a Yukawa potential numerically. This will be important later, when the exact conditions will help determine which bound states can form at experiment. These so-called critical screening lengths are given in Table 2 in Section 4.2.2. Now we can look at the parameter space and examine where bound states can form. To avoid having to look at a three-dimensional parameter space, we fix $m_V = 100$ MeV as a benchmark. In addition to leaving a two-dimensional parameter space, this choice also allows relatively large values of ϵ that are not excluded by experiment. This means we can consider relatively large couplings to the Standard Model, and therefore relatively large production rates of dark matter particles and dark matter bound states. The excluded values of ϵ are shown in Figure 2.1[11].

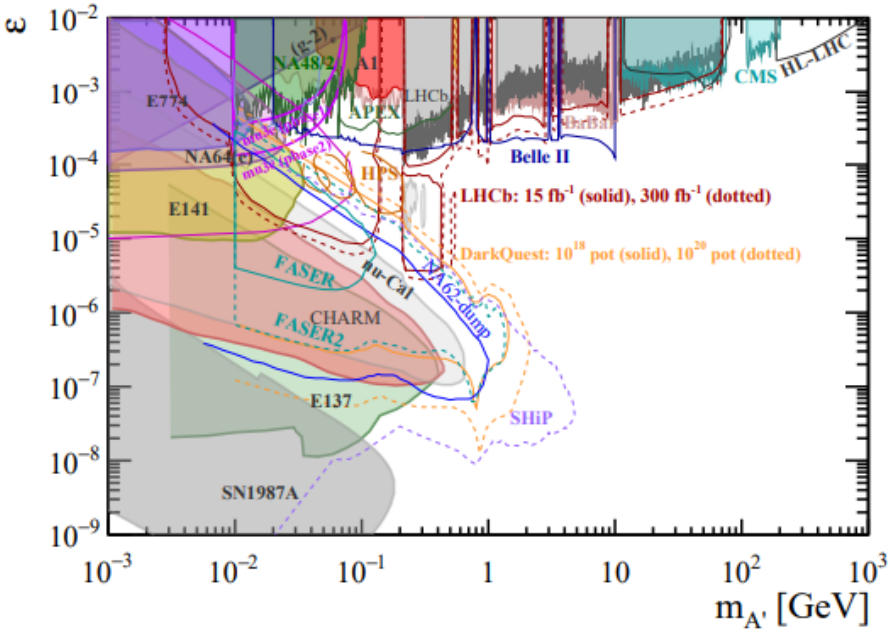

Figure 2.1: Bounds on the combination of dark photon mass ($m_{A'}$ in the figure) and ϵ. The colored areas are existing bounds from experiment. The colored curves are projections for existing and proposed experiments. Figure taken from Ref. [11].

The benchmark of $m_V = 100\,\text{MeV}$ allows us to consider $\epsilon \sim 10^{-4}$. Now, with our parameter space reduced to just two parameters, we can look at where in this parameter space the Yukawa potential supports bound states. This is shown in Figure 2.2 for bound states up to $n = 3$ and $L = 2$.

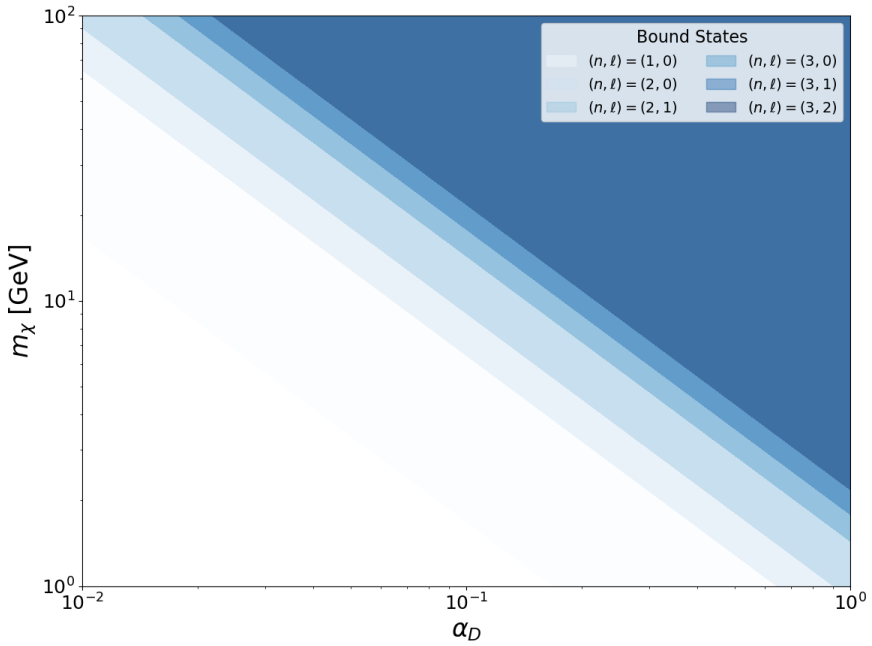

Figure 2.2: The parameter space (α_D, m_χ), with marked areas where the different bound states can form. The regions must be viewed as overlapping, that is, the lightest region extends under the darker ones.

This parameter space will guide us later when we take to experiment. The next step is to

look at how we may go about calculating the production of bound states within quantum field theory, this will be done in the next section.

3 Bound State Calculations in the Non-Relativistic Limit

As we will be interested in calculating the production and decay rates of bound states, we need to set up a framework to do so. In this section, we will set up the method of using projectors to do such calculations. The results, which we will discuss here, can be found in Ref. [12]. In this work, we will work exclusively with bound states consisting of two particles of equal mass, that is, the bound state $\chi\bar{\chi}$.

3.1 Bound State Description

To work with a bound state in calculations of production and decay amplitudes, we adopt the definition of Peskin and Schroeder [13]. In the non-relativistic limit the bound state is a superposition of product states of the two constituent particles, weighted by the non-relativistic wave function, i.e. the solution of the Schrödinger equation. The bound state consisting of two constituents for a certain spin configuration, say $|\uparrow\uparrow\rangle$ is then described by

$$|B\rangle = \sqrt{2M}\int \frac{d^3k}{(2\pi)^3}\tilde{\psi}(\mathbf{k})\frac{1}{\sqrt{2m}}\frac{1}{\sqrt{2m}}|\mathbf{k}\uparrow, -\mathbf{k}\uparrow\rangle. \tag{3.1}$$

Here we work in the bound state rest frame. M represents the bound state mass and m the mass of each of the two constituents, which are assumed to have equal mass. We will be concerned with spin 1/2 particles. For a given spin configuration of the bound state we can use the Clebsch-Gordan coefficients to project on it. The bound state for an arbitrary spin configuration (S,S_z) is then given by

$$|B\rangle = \sqrt{2M}\int \frac{d^3k}{(2\pi)^3}\tilde{\psi}(\mathbf{k})\frac{1}{\sqrt{2m}}\frac{1}{\sqrt{2m}}\sum_{s\bar{s}} C^{SS_z}_{\frac{1}{2}s\frac{1}{2}\bar{s}}|\mathbf{k}, s; -\mathbf{k}, \bar{s}\rangle. \tag{3.2}$$

Here s and $\bar{s}$ are the spin projections on the z direction of the two constituents. If we are now interested in some process involving producing such a bound state, we get, after applying Feynman rules, an amplitude of the form (see Figure 3.1(a))

$$\mathcal{M} \propto \sum_{s\bar{s}} \bar{u}(p,s)Ov(q,\bar{s})C^{SS_z}_{\frac{1}{2}s\frac{1}{2}\bar{s}}, \tag{3.3}$$

where u and v are Dirac spinors and O represents the rest of the amplitude[i]. For a decay process, we get an expression of the form (see Figure 3.1(b))

$$\mathcal{M} \propto \sum_{s\bar{s}} \bar{v}(q,\bar{s})Ou(p,s)C^{SS_z}_{\frac{1}{2}s\frac{1}{2}\bar{s}}. \tag{3.4}$$

The goal is to rewrite this sum weighted by Clebsch-Gordan coefficients as a trace over O and a spin projector.

[i]Here we write the momenta as p and q, but it is understood here that we work in the bound state rest frame.

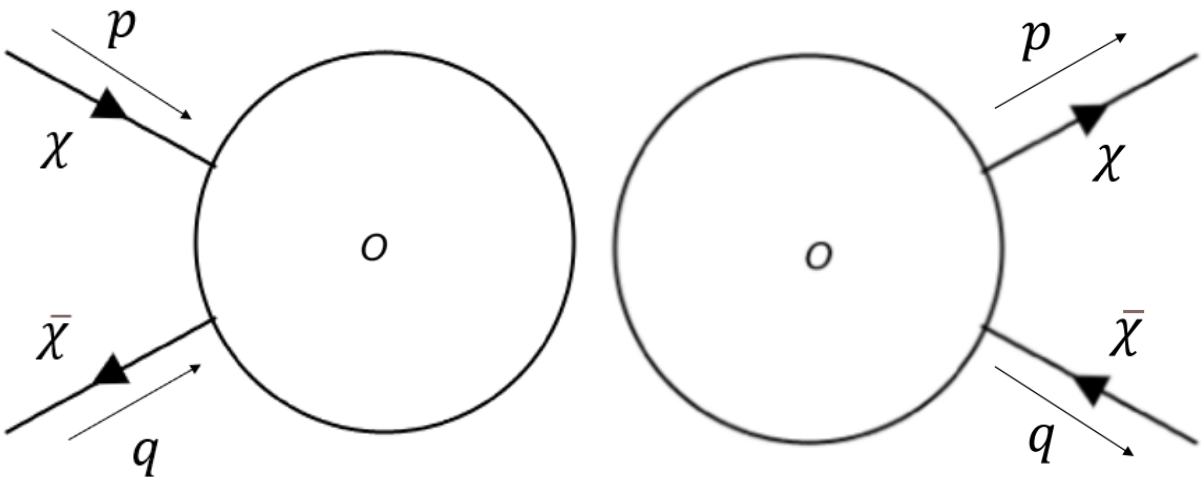

(a) (b)

Figure 3.1: General processes for the annihilation (left) and production (right) of a $\chi\bar{\chi}$ bound state. O here represents an arbitrary process, the only requirement is that the χ and $\bar{\chi}$ belong to one continuous fermion line.

3.2 Spin Projectors for Bound State Decay

We start by considering a process where a bound state decays, Figure 3.1(a). First, we rewrite the Clebsch-Gordan coefficients as

$$C^{SS_z}_{\frac{1}{2}s\frac{1}{2}\bar{s}} = \bar{u}(p,s)P_{SS_z}v(q,\bar{s}). \tag{3.5}$$

Substituting this into Equation 3.4 and applying the completeness relations for the spinors, we find

$$\sum_{s\bar{s}} \bar{v}(q,\bar{s})Ou(p,s)C^{SS_z}_{\frac{1}{2}s\frac{1}{2}\bar{s}} = \mathrm{Tr}\left((\not{q}-m)O(\not{p}+m)P_{SS_z}\right). \tag{3.6}$$

Next, we need to find the form of P_{SS_z} such that Equation 3.5 is satisfied. We start by looking at the form of the canonical solutions of the Dirac equation. As we are working in the bound state rest frame, we only have to deal with the relative momentum between the constituent particles. For now, we choose this momentum along the z direction, resulting in solutions to the Dirac equation that have a clear spin interpretation; these are eigenstates of the $\hat{s}_z$ operator for the individual constituents. The four solutions are then given by (see [14])

$$u(p,\uparrow) = \sqrt{E+m}\begin{pmatrix}1\\0\\\frac{p}{E+m}\\0\end{pmatrix},\ u(p,\downarrow) = \sqrt{E+m}\begin{pmatrix}0\\1\\0\\\frac{-p}{E+m}\end{pmatrix}, \tag{3.7}$$

for positive energy solutions and

$$v(p,\uparrow) = \sqrt{E+m}\begin{pmatrix}0\\\frac{-p}{E+m}\\0\\1\end{pmatrix},\ v(p,\downarrow) = -\sqrt{E+m}\begin{pmatrix}\frac{p}{E+m}\\0\\1\\0\end{pmatrix}, \tag{3.8}$$

for negative energy solutions[ii]. The matrices P_{SS_z} that satisfy Equation 3.5 are now easily found by inspection. We find

$$\begin{aligned}
P_{00} &= \frac{1}{\sqrt{2}}\frac{1}{\sqrt{E_p+m}}\frac{1}{\sqrt{E_q+m}}\begin{pmatrix}0&0&-1&0\\0&0&0&-1\\0&0&0&0\\0&0&0&0\end{pmatrix};\\
P_{11} &= \frac{1}{\sqrt{E_p+m}}\frac{1}{\sqrt{E_q+m}}\begin{pmatrix}0&0&0&1\\0&0&0&0\\0&0&0&0\\0&0&0&0\end{pmatrix};\\
P_{10} &= \frac{1}{\sqrt{2}}\frac{1}{\sqrt{E_p+m}}\frac{1}{\sqrt{E_q+m}}\begin{pmatrix}0&0&-1&0\\0&0&0&1\\0&0&0&0\\0&0&0&0\end{pmatrix};\\
P_{1-1} &= \frac{1}{\sqrt{E_p+m}}\frac{1}{\sqrt{E_q+m}}\begin{pmatrix}0&0&0&0\\0&0&-1&0\\0&0&0&0\\0&0&0&0\end{pmatrix}.
\end{aligned} \tag{3.9}$$

Decomposing these matrices in terms of the basis $\{I_4, \gamma^5, \gamma^\mu, \gamma^\mu\gamma^5, \sigma^{\mu\nu}\}$ we get our final result

$$\begin{aligned}
P_{00} &= \frac{1}{\sqrt{E_p+m}}\frac{1}{\sqrt{E_q+m}}\frac{1+\gamma^0}{2\sqrt{2}}(-\gamma^5);\\
P_{1S_z} &= \frac{1}{\sqrt{E_p+m}}\frac{1}{\sqrt{E_q+m}}\frac{1+\gamma^0}{2\sqrt{2}}(-\not{\epsilon}^*_{(S_z)}),
\end{aligned} \tag{3.10}$$

where

$$\epsilon^\mu_{(S_z)} = \begin{cases}\begin{pmatrix}0&0&0&-1\end{pmatrix}^\top & \text{if } S_z = 0\\ \begin{pmatrix}0&\pm1&-i&0\end{pmatrix}^\top/\sqrt{2} & \text{if } S_z = \pm1\end{cases}. \tag{3.11}$$

The matrix P_{SS_z} can now be used in Equation 3.6 to project the bound state on the total spin S and projection on the z axis S_z. From our bound state definition, we have an integral over the relative momentum $\mathbf{k}$. This means that we cannot just assume the relative momentum to be aligned with the z-axis, as assumed so far. However, as we are working in the non-relativistic limit, the momentum components of the spinors, which scale like p/m, are negligible. Therefore, the projection operators hold for all directions of the relative momentum $\mathbf{k}$. In other words, the spinor solutions are always eigenstates of the $\hat{s}_z$ operator in the non-relativistic limit. Meaning we can keep our interpretation of $s = \pm 1/2$ along the z-axis.

The recipe for doing a bound-state decay rate calculation is now easy. First, we calculate the amplitude for the process for the constituents. Then we incorporate the sum over spins by using Equation 3.6 together with the desired spin projector. There is one caveat, which is the integral over the relative momentum $\mathbf{k}$ and the wave function that appears in the definition of the bound state. We will come back to this later.

3.3 Spin Projectors for Bound State Production

The next step is to see if and how the projection operators change if we are interested in a bound state production process rather than decay, see Figure 3.1(b). As mentioned earlier, for

[ii] We work in the Dirac representation and for the spinors use the normalization condition $u^\dagger u = 2E$.

the amplitude we get an expression of the form

$$\mathcal{M} \propto \sum_{s\bar{s}} \bar{u}(p,s) O v(q,\bar{s}) C^{SS_z}_{\frac{1}{2}s\frac{1}{2}\bar{s}}.$$

This suggests that we should write the Clebsch-Gordan coefficients as

$$C^{SS_z}_{\frac{1}{2}s\frac{1}{2}\bar{s}} = \bar{v}(q,\bar{s}) P'_{SS_z} u(p,s) \tag{3.12}$$

such that we can apply the completeness relations of the spinors again. This will result in the following equation

$$\sum_{s\bar{s}} \bar{u}(p,s) O v(q,\bar{s}) C^{SS_z}_{\frac{1}{2}s\frac{1}{2}\bar{s}} = \mathrm{Tr}\left((\not{p}+m) O (\not{q}-m) P'_{SS_z}\right). \tag{3.13}$$

As the Clebsch-Gordan coefficients are real numbers, we can write

$$(\bar{v}(q,\bar{s}) P'_{SS_z} u(p,s))^* = \bar{u}(p,s) P_{SS_z} v(q,s), \tag{3.14}$$

which, when using that complex conjugation and hermitian conjugation are the same for a complex number, results in a relation between P'_{SS_z} and P_{SS_z},

$$P'_{SS_z} = \gamma^0 P^\dagger_{SS_z} \gamma^0. \tag{3.15}$$

Concretely, the projection operators for bound state production are given by

$$\begin{aligned} P'_{00} &= \frac{1}{\sqrt{E_p+m}} \frac{1}{\sqrt{E_q+m}} \gamma^5 \frac{1+\gamma^0}{2\sqrt{2}}; \\ P'_{1S_z} &= \frac{1}{\sqrt{E_p+m}} \frac{1}{\sqrt{E_q+m}} (-\not{\epsilon}_{(S_z)}) \frac{1+\gamma^0}{2\sqrt{2}}, \end{aligned} \tag{3.16}$$

where $\not{\epsilon}_{(S_z)}$ is again given by Equation 3.11. For the spin 0 case, we now have the factor $\frac{1+\gamma^0}{2\sqrt{2}}$ to the right of the γ^5 and an additional minus sign, compared to the decay case. For the spin 1 case, we also have the factor $\frac{1+\gamma^0}{2\sqrt{2}}$ on the right, and the polarization vector is complex conjugated with respect to the decay projectors.

3.4 Alternative Spin Projectors

In the literature one often sees a different set of projectors being used, see Ref. [15]. To reproduce the Clebsch-Gordan coefficients in Equation 3.5, there is a choice for the projection operators different from those given in Equation 3.9. These, we could have also found by immediately neglecting the p/m components in the spinors. We can choose the following projectors

$$\begin{aligned} P_{00} &= \frac{1}{\sqrt{2}} \frac{1}{\sqrt{E_p+m}} \frac{1}{\sqrt{E_q+m}} (-\gamma^5); \\ P_{10} &= \frac{1}{\sqrt{2}} \frac{1}{\sqrt{E_p+m}} \frac{1}{\sqrt{E_q+m}} (-\gamma^3); \\ P_{11} &= \frac{1}{\sqrt{2}} \frac{1}{\sqrt{E_p+m}} \frac{1}{\sqrt{E_q+m}} \left(\frac{1}{\sqrt{2}}\gamma^1 + \frac{i}{\sqrt{2}}\gamma^2\right); \\ P_{1-1} &= \frac{1}{\sqrt{2}} \frac{1}{\sqrt{E_p+m}} \frac{1}{\sqrt{E_q+m}} \left(-\frac{1}{\sqrt{2}}\gamma^1 + \frac{i}{\sqrt{2}}\gamma^2\right). \end{aligned} \tag{3.17}$$

$\left\|\frac{1}{2},m_1\right\rangle \otimes \left\|\frac{1}{2},m_2\right\rangle$	$\|1,1\rangle$	$\|1,0\rangle$	$\|1,-1\rangle$	$\|0,0\rangle$
$\left\|\frac{1}{2},\frac{1}{2}\right\rangle \otimes \left\|\frac{1}{2},\frac{1}{2}\right\rangle$	$1+\frac{k^2}{(E+m)^2}$	0	0	0
$\left\|\frac{1}{2},\frac{1}{2}\right\rangle \otimes \left\|\frac{1}{2},-\frac{1}{2}\right\rangle$	0	$\frac{1}{\sqrt{2}}(1-\frac{k^2}{(E+m)^2})$	0	$\frac{1}{\sqrt{2}}(1+\frac{k^2}{(E+m)^2})$
$\left\|\frac{1}{2},-\frac{1}{2}\right\rangle \otimes \left\|\frac{1}{2},\frac{1}{2}\right\rangle$	0	$\frac{1}{\sqrt{2}}(1-\frac{k^2}{(E+m)^2})$	0	$-\frac{1}{\sqrt{2}}(1+\frac{k^2}{(E+m)^2})$
$\left\|\frac{1}{2},-\frac{1}{2}\right\rangle \otimes \left\|\frac{1}{2},-\frac{1}{2}\right\rangle$	0	0	$1+\frac{k^2}{(E+m)^2}$	0

Table 1: Spin-sum coefficients for the addition of the spins of the bound state constituents $\frac{1}{2}\otimes\frac{1}{2}$. In the non-relativistic limit, where $\frac{k^2}{(E+m)^2} \ll 1$ these reduce to the correct Clebsch-Gordan coefficients.

For the relative momentum direction along z, these projectors result in the spin-sum coefficients given in Table 1. In the non-relativistic limit where $\frac{k^2}{(E+m)^2} \ll 1$, these projectors result in the correct Clebsch-Gordan coefficients. Since our bound state definition is already non-relativistic, as we describe it using the non-relativistic Schrödinger wave function, these projectors are equally valid.

To determine the projectors for bound state production we can still use Equation 3.15. In this case, we find

$$\begin{aligned}
P'_{00} &= \frac{1}{\sqrt{2}}\frac{1}{\sqrt{E_p+m}}\frac{1}{\sqrt{E_q+m}}(\gamma^5);\\
P'_{10} &= \frac{1}{\sqrt{2}}\frac{1}{\sqrt{E_p+m}}\frac{1}{\sqrt{E_q+m}}(-\gamma^3);\\
P'_{11} &= \frac{1}{\sqrt{2}}\frac{1}{\sqrt{E_p+m}}\frac{1}{\sqrt{E_q+m}}(\frac{1}{\sqrt{2}}\gamma^1-\frac{i}{\sqrt{2}}\gamma^2);\\
P'_{1-1} &= \frac{1}{\sqrt{2}}\frac{1}{\sqrt{E_p+m}}\frac{1}{\sqrt{E_q+m}}(-\frac{1}{\sqrt{2}}\gamma^1-\frac{i}{\sqrt{2}}\gamma^2).
\end{aligned} \tag{3.18}$$

If we introduce again the polarization vectors of Equation 3.11, we can write these projectors in a more compact form as

$$\begin{aligned}
P'_{00} &= \frac{1}{\sqrt{8m^2}}(\gamma^5);\\
P'_{1S_z} &= \frac{1}{\sqrt{8m^2}}(-\not{\epsilon}'_{S_z}),
\end{aligned} \tag{3.19}$$

where we used that in the non-relativistic limit $E \approx m$. If we take into account the momentum terms as given in the right hand side of Equation 3.13, and we absorb the factor $\frac{\sqrt{2M}}{2m} \approx \frac{1}{\sqrt{m}}$ from the bound state definition into the projectors, we find, up to a minus sign for the spin 1 case, the projectors as often used in the literature, see for example Ref. [15]. The minus sign stems from a different convention for the polarization vectors.

3.5 Towards a Matrix Element for Bound State Processes

Now that we have two sets of projectors that allow us to project on the correct spin configurations of the bound, we can work towards finding an expression for the matrix element for bound state production and decay. The derivation we do is valid for both sets. Later, however, when we start calculating in sections 5 and onward, we will use the sets of equations 3.17 and 3.19. The first step is to expand the trace expressions we found earlier, equations 3.6 and 3.13,

as a power series in the relative momentum divided by the constituent mass. We start with the bound state production, the bound state decay case is nearly identical.

Earlier we found the trace expression

$$\sum_{s\bar{s}} \bar{u}(p,s) O v(q,\bar{s}) C^{SS_z}_{\frac{1}{2}s\frac{1}{2}\bar{s}} = \mathrm{Tr}\left(f(k) P'_{SS_z}\right),$$

here we define

$$f(k) \equiv (\not{p} + m) O (\not{q} - m). \tag{3.20}$$

Remembering we are working in the bound state rest frame, we write

$$P = \begin{pmatrix} M \\ 0 \\ 0 \\ 0 \end{pmatrix} \text{ and } k = \begin{pmatrix} 0 \\ \mathbf{k} \end{pmatrix},$$

where P is the bound state momentum and we have $p = P/2 + k$ and $q = P/2 - k$. We want to expand our function $f(k)$ in the small parameter k/m in order to be able to perform the integral over the relative momentum later. We start by taking out a factor m^2 of $f(k)$ in which case it is more obvious it is a function of $\lambda \equiv k/m$. We define $f(\lambda) \equiv f(k)/m^2$. In this case, we can write the expansion of $f(k)$ as

$$f(k) = \frac{1}{m^2} \sum_{n=0}^{\infty} \frac{1}{n!} \left. \frac{\partial^n f(\lambda)}{\partial\lambda^{\mu_1}\partial\lambda^{\mu_2}\cdots\partial\lambda^{\mu_n}} \right|_{\lambda=0} \lambda^{\mu_1}\lambda^{\mu_2}\cdots\lambda^{\mu_n}. \tag{3.21}$$

Now we recall that we defined the bound state according to Equation 3.2,

$$|B\rangle = \sqrt{2M} \int \frac{d^3\mathbf{k}}{(2\pi)^3} \tilde{\psi}(\mathbf{k}) \frac{1}{\sqrt{2m}} \frac{1}{\sqrt{2m}} \sum_{s\bar{s}} C^{SS_z}_{\frac{1}{2}s\frac{1}{2}\bar{s}} |\mathbf{k}, \mathbf{s}; -\mathbf{k}, \bar{\mathbf{s}}\rangle,$$

where $\tilde{\psi}(\mathbf{k})$ is the Fourier transform of the spatial Schrödinger wave function $\psi(\mathbf{r})$. For a given bound state $^{2S+1}L_J$ the wave function is given by

$$\psi(\mathbf{r}) = \sum_{M_L M_S} C^{JM_J}_{LM_L SM_S} \psi_{nLM_L}(\mathbf{r}). \tag{3.22}$$

Here $C^{JM_J}_{LM_L SM_S}$ are the Clebsch-Gordan coefficients to form a total angular momentum state from the total spin and orbital angular momentum of the bound state. The spin part of the wave function is contained in the bound state definition. The wave function $\psi_{nLM_L}(\mathbf{r})$ is the solution of the Schrödinger equation corresponding to the nth energy level and angular momentum quantum numbers L and M_L. We will discuss these in Section 4 when we discuss the Schrödinger equation with a Yukawa potential. The Fourier transform is then given by

$$\tilde{\psi}(\mathbf{k}) = \int d^3\mathbf{r} e^{i\mathbf{k}\cdot\mathbf{r}} \sum_{M_L M_S} C^{JM_J}_{LM_L SM_S} \psi_{nLM_L}(\mathbf{r}). \tag{3.23}$$

Combining this with the bound state definition we find

$$|B\rangle = \frac{\sqrt{2M}}{2m} \int \frac{d^3\mathbf{k}}{(2\pi)^3} \left(\int d^3\mathbf{r} e^{i\mathbf{k}\cdot\mathbf{r}} \sum_{M_L M_S} C^{JM_J}_{LM_L SM_S} \psi_{nLM_L}(\mathbf{r}) \right) \sum_{s\bar{s}} C^{SM_S}_{\frac{1}{2}s\frac{1}{2}\bar{s}} |\mathbf{k}, \mathbf{s}; -\mathbf{k}, \bar{\mathbf{s}}\rangle. \tag{3.24}$$

Now for an arbitrary process $1+2+\cdots+n \to (n+1)+(n+2)+\cdots+(n+m)+B$ we can write

$$\langle \mathbf{p}_{n+1}\cdots\mathbf{p}_{n+m}\mathbf{p}_{BS}|i\mathcal{T}|\mathbf{p}_1\cdots\mathbf{p}_n\rangle = (2\pi)^4\delta^4\left(\sum p_i - \sum p_f\right) i\mathcal{M}\left(p_i\cdots p_n \to p_{n+1}\cdots p_{n+m}p_{BS}\right) \tag{3.25}$$

, where $\sum p_i$ and $\sum p_f$, are sums over initial and final momenta, respectively. $\mathcal{T}$ follows from $\mathcal{S} = 1 + i\mathcal{T}$, see Ref. [13]. The left hand side of Equation 3.25 can be worked out using the bound state definition in Equation 3.24 to yield

$$\begin{aligned}(2\pi)^4\delta^{(4)}\left(\Sigma p_i - \Sigma p_f\right)\mathcal{M}_{BS} = \frac{\sqrt{2M}}{2m}\int\frac{d^3\mathbf{k}}{(2\pi)^3}\left(\int d^3\mathbf{r}e^{-i\mathbf{k}\cdot\mathbf{r}}\sum_{M_LM_S} C^{JM_J}_{LM_LSM_S}\psi^*_{nLM_L}(\mathbf{r})\right)\\ \cdot\sum_{s\bar{s}} C^{SM_S}_{\frac{1}{2}s\frac{1}{2}\bar{s}}\langle\mathbf{k},s;-\mathbf{k},\bar{s};\mathbf{p_{n+1}},m_{s_{n+1}};\cdots;\mathbf{p_{n+m}},m_{s_{n+m}}|i\mathcal{T}|\mathbf{p_1},m_{s_1};\cdots;\mathbf{p_n},m_{s_n}\rangle,\end{aligned} \tag{3.26}$$

where $\mathcal{M}_{BS}$ represents the matrix element for producing the Bound State. The complex conjugation of the bound state definition comes from using a bra in Equation 3.25. We can simplify our expression to

$$\begin{aligned}(2\pi)^4\delta^{(4)}\left(\Sigma p_i - \Sigma p_f\right)\mathcal{M}_{BS} =&\frac{\sqrt{2M}}{2m}\int\frac{d^3\mathbf{k}}{(2\pi)^3}\left(\int d^3\mathbf{r}e^{-i\mathbf{k}\cdot\mathbf{r}}\sum_{M_LM_S} C^{JM_J}_{LM_LSM_S}\psi^*_{nLM_L}(\mathbf{r})\right)\\ &\cdot\sum_{s\bar{s}} C^{SM_S}_{\frac{1}{2}s\frac{1}{2}\bar{s}}(2\pi)^4\delta^{(4)}(\Sigma p_i - \Sigma p_f)\mathcal{M}_C(\mathbf{k},s,\bar{s}),\end{aligned} \tag{3.27}$$

where $\mathcal{M}_C(\mathbf{k},s,\bar{s})$ represents the matrix element for producing the bound state constituents at momentum $\mathbf{k}$ in the bound state rest frame and spin configuration $s,\bar{s}$[iii]. Canceling the delta functions and factors $(2\pi)^4$, and using the trace formula, eqaution 3.13 for $\sum C^{SM_S}_{\frac{1}{2}s\frac{1}{2}\bar{s}}\mathcal{M}_C(\mathbf{k},s,\bar{s})$ we find an expression for the matrix element of producing the bound state in terms of that of producing the constituents

$$\begin{aligned}\mathcal{M}_{BS} =&\frac{\sqrt{2M}}{2m}\int\frac{d^3\mathbf{k}}{(2\pi)^3}\left(\int d^3\mathbf{r}e^{-i\mathbf{k}\cdot\mathbf{r}}\sum_{M_LM_S} C^{JM_J}_{LM_LSM_S}\psi^*_{LM_L}(\mathbf{r})\right)\\ &\cdot\mathrm{Tr}\left(\frac{1}{m^2}\sum_{n=0}^{\infty}\frac{1}{n!}\left.\frac{\partial^n f(\lambda)}{\partial\lambda^{\mu_1}\partial\lambda^{\mu_2}\cdots\partial\lambda^{\mu_n}}\right|_{\lambda=0}\lambda^{\mu_1}\lambda^{\mu_2}\cdots\lambda^{\mu_n}P_{SM_S}\right).\end{aligned} \tag{3.28}$$

Here $f(\lambda)$ represents a process-specific function of λ that appears inside the trace. We suppressed the quantum number n of the wave function ψ_{nL} to avoid confusion with the dummy variable in the sum. Using linearity of the trace we can write

$$\begin{aligned}\mathcal{M}_{BS} =&\frac{\sqrt{2M}}{2m}\frac{1}{m^2}\sum_{n=0}^{\infty}\frac{1}{n!}\sum_{M_LM_S} C^{JM_J}_{LM_LSM_S}\mathrm{Tr}\left(\left.\frac{\partial^n f(\lambda)}{\partial\lambda^{\mu_1}\partial\lambda^{\mu_2}\cdots\partial\lambda^{\mu_n}}\right|_{\lambda=0}P_{SM_S}\right)\\ &\cdot\int\frac{d^3\mathbf{k}}{(2\pi)^3}\left(\int d^3\mathbf{r}\lambda^{\mu_1}\lambda^{\mu_2}\cdots\lambda^{\mu_n}e^{-i\mathbf{k}\cdot\mathbf{r}}\psi^*_{LM_L}(\mathbf{r})\right).\end{aligned} \tag{3.29}$$

The λ^{μ_i} can be taken out of the $\mathbf{r}$ integral, the $\mathbf{r}$ integral is then the complex conjugate Fourier transform of $\psi_{nLM_L}(\mathbf{r})$,

$$\begin{aligned}\mathcal{M}_{BS} =&\frac{\sqrt{2M}}{2m}\frac{1}{m^2}\sum_{n=0}^{\infty}\frac{1}{n!}\sum_{M_LM_S} C^{JM_J}_{LM_LSM_S}\mathrm{Tr}\left(\left.\frac{\partial^n f(\lambda)}{\partial\lambda^{\mu_1}\partial\lambda^{\mu_2}\cdots\partial\lambda^{\mu_n}}\right|_{\lambda=0}P_{SM_S}\right)\\ &\cdot\left(\int\frac{d^3\mathbf{k}}{(2\pi)^3}\lambda^{\mu_1}\lambda^{\mu_2}\cdots\lambda^{\mu_n}\psi^*_{LM_L}(\mathbf{k})\right).\end{aligned} \tag{3.30}$$

[iii]Here we ignored all the momenta and spins of the other particles in the process, these are implicit here.

It can be shown that only the term $n = L$ contributes, which gives the final result

$$\begin{aligned}\mathcal{M}_{BS} =& \frac{\sqrt{2M}}{2m}\frac{1}{L!}\sum_{M_L M_S} C^{JM_J}_{LM_L SM_S}\mathrm{Tr}\left(\left.\frac{\partial^L f(k)}{\partial k^{\mu_1}\partial k^{\mu_2}\cdots\partial k^{\mu_L}}\right|_{k=0} P_{SM_S}\right) \\ & \cdot \frac{1}{4\pi i^L}\frac{\Gamma(L+\frac{3}{2})2^{1+L}}{\sqrt{\pi}\Gamma(1+L)}\left.\frac{d^L}{dr^L}R^*_{nL}(r)\right|_{r=0}\left(2\sqrt{\frac{\pi}{3}}\right)^L \\ & \cdot \sum_{m_1=-1}^{1}\cdots\sum_{m_L=-1}^{1}\epsilon^{\mu_1}_{(m_1)}\cdots\epsilon^{\mu_L}_{(m_L)}\int d\Omega Y_1^{m_1}(\theta,\phi)\cdots Y_1^{m_L}(\theta,\phi)Y_L^{M_L *}(\theta,\phi),\end{aligned} \tag{3.31}$$

here, $R_{nL}(r)$ is the radial part of the wave function $\psi_{nL}(\mathbf{r})$, $Y_L^{M_L}(\theta,\phi)$ the angular part, and Γ is the gamma function. We have reintroduced the principal quantum number n on the wave function and expressed everything again in terms of k^{μ_i}. The derivation of only the $n = L$ term contributing and the method of working out the remaining integral over $\mathbf{k}$ are given in Appendix A.

This formula is easily generalized to bound state decay. Repeating the same derivation for the bound state decay results in the following matrix element

$$\begin{aligned}\mathcal{M}_{BS} =& \frac{\sqrt{2M}}{2m}\frac{1}{L!}\sum_{M_L M_S} C^{JM_J}_{LM_L SM_S}\mathrm{Tr}\left(\left.\frac{\partial^L f(k)}{\partial k^{\mu_1}\partial k^{\mu_2}\cdots\partial k^{\mu_L}}\right|_{k=0} P_{SM_S}\right) \\ & \cdot \frac{1}{4\pi i^L}\frac{\Gamma(L+\frac{3}{2})2^{1+L}}{\sqrt{\pi}\Gamma(1+L)}\left.\frac{d^L}{dr^L}R_{nL}(r)\right|_{r=0}\left(-2\sqrt{\frac{\pi}{3}}\right)^L \\ & \cdot \sum_{m_1=-1}^{1}\cdots\sum_{m_L=-1}^{1}\epsilon^{\mu_1 *}_{(m_1)}\cdots\epsilon^{\mu_L *}_{(m_L)}\int d\Omega Y_1^{m_1 *}(\theta,\phi)\cdots Y_1^{m_L *}(\theta,\phi)Y_L^{M_L}(\theta,\phi).\end{aligned} \tag{3.32}$$

It needs to be noted that the meaning of $f(k)$ and P_{SM_S} are different than in the case of bound state production. Here

$$f(k) = (\not{q} - m)O(\not{p} + m)$$

and the projectors are those of Equation 3.17.

The equations 3.31 and 3.32 will be the formulae we will use to do the bound state production and decay calculations in the rest of this work. Then we will also simplify the matrix element formulae for specific cases of L.

The next step is to discuss the wave function of the bound state, as this plays an important role in our matrix elements.

4 The Schrödinger Equation With a Yukawa Potential

As was discussed before, and as can be seen in equations 3.32 and 3.31, we need to know the wave function of the bound state. In this section we will set up the problem of finding the wave function, which is a solution to the Schrödinger equation with a Yukawa potential. We will also develop a numerical approach to solve the problem. We start with setting up the problem.

4.1 Setting up the Radial Equation

4.1.1 Separation of Variables

Solving the Schrödinger equation for a spherically symmetric potential is something that is treated in almost all textbooks on quantum mechanics; see, for example, [16]. Here we include it for completeness and analyze the behavior of the solution near the origin, as this will become important later. In spherical coordinates, the Schrödinger equation becomes (setting $\hbar = 1$)

$$-\frac{1}{2\mu}\left(\frac{1}{r^2}\frac{\partial}{\partial r}\left(r^2\frac{\partial\psi}{\partial r}\right)+\frac{1}{r^2\sin\theta}\frac{\partial}{\partial\theta}\left(\sin\theta\frac{\partial\psi}{\partial\theta}\right)+\frac{1}{r^2\sin^2\theta}\left(\frac{\partial^2\psi}{\partial\phi^2}\right)\right)+V(r)\psi=E\psi, \tag{4.1}$$

here, μ is the reduced mass and $\mu = m_\chi/2$ for a $\chi\bar{\chi}$ bound state.

Now we assume a solution of the form

$$\psi(r,\theta,\phi) = R(r)Y(\theta,\phi). \tag{4.2}$$

Such an assumption leads to the following equation

$$\left(\frac{1}{R}\frac{\mathrm{d}}{\mathrm{d}r}\left(r^2\frac{\mathrm{d}R}{\mathrm{d}r}\right)-2\mu r^2\left[V(r)-E\right]\right)+\frac{1}{Y}\left(\frac{1}{\sin\theta}\frac{\partial}{\partial\theta}\left(\sin\theta\frac{\partial Y}{\partial\theta}\right)+\frac{1}{\sin^2\theta}\frac{\partial^2 Y}{\partial\phi^2}\right)=0. \tag{4.3}$$

Now we can separate this into two equations. Both terms on the left-hand side of Equation 4.3 are equal to a constant. If not both were constant, the term dependent only on r would change when we change θ or ϕ, contradicting the fact that the left term depends only on r, and vice versa. Following the standard literature, we introduce the separation constant $l(l+1)$, such that we get

$$\frac{1}{R}\frac{\mathrm{d}}{\mathrm{d}r}\left(r^2\frac{\mathrm{d}R}{\mathrm{d}r}\right)-2\mu r^2\left[V(r)-E\right]=l(l+1); \tag{4.4}$$

$$\frac{1}{Y}\left(\frac{1}{\sin\theta}\frac{\partial}{\partial\theta}\left(\sin\theta\frac{\partial Y}{\partial\theta}\right)+\frac{1}{\sin^2\theta}\frac{\partial^2 Y}{\partial\phi^2}\right)=-l(l+1). \tag{4.5}$$

We will not be bothered with solving the angular equation, the solutions are well known and are discussed in nearly all textbooks on quantum mechanics. The solutions are the spherical harmonics [16]

$$Y_l^m(\theta,\phi)=\sqrt{\frac{(2l+1)}{4\pi}\frac{(l-m)!}{(l+m)!}}e^{im\phi}P_l^m(\cos\theta), \tag{4.6}$$

where P_l^m are the associated Legendre polynomials. For the radial part $R(r)$, we are interested in solving it explicitly, because it contains information about the potential. We start by making the substitution $u(r) = rR(r)$ which simplifies the equation to

$$-\frac{1}{2\mu}\frac{d^2u(r)}{dr^2}+\left(V(r)+\frac{\hbar^2}{2\mu}\frac{l(l+1)}{r^2}\right)u(r)=Eu(r). \tag{4.7}$$

This is the radial equation. It has exactly the form of the one-dimensional Schrödinger equation with an effective potential given by

$$V_{\text{eff}}(r)=V(r)+\frac{1}{2\mu}\frac{l(l+1)}{r^2}. \tag{4.8}$$

4.1.2 The Yukawa Potential

In this work we are interested in dark matter bound states. When we consider them in the non-relativistic case, the interaction between the two constituents of the bound state can, as mentioned before, be described by the Schrödinger equation with a Yukawa potential [17],

$$V(r) = -\frac{\alpha}{r}e^{-mr}, \tag{4.9}$$

where α gives the strength of the interaction and m is the mass of the mediator particle. For production and decay rate calculations of such bound states, we need $|R(0)|^2$ and its derivatives at the origin. Section 4.2 will discuss the numerical approach taken in this work to approximate these quantities. However, we can already say something about this without doing the explicit calculation. Consider the limit as $r \to 0$. If the power series expansion of the potential contains no terms r^n with powers $n < -1$, which is the case for the Yukawa potential, it will be the centrifugal term that dominates near the origin. The potential and energy terms will be negligible:

$$\frac{\mathrm{d}^2u(r)}{\mathrm{d}r^2} \approx \frac{l(l+1)}{r^2}u(r), \tag{4.10}$$

which has the solution

$$u(r) = Ar^{l+1} + Br^{-l}. \tag{4.11}$$

The second term is unphysical as it blows up near the origin, therefore, we know that near the origin the solutions will behave as $u(r) \sim r^{l+1}$. Using $u(r) = rR(r)$ we find $R(r) \sim r^l$ near the origin. From this we can conclude that $|R(0)|^2 = 0$ if $l \neq 0$. Similarly, we can already say $\frac{\mathrm{d}^k R}{\mathrm{d}r^k}|_{r=0} = 0$ if $k < l$.

4.1.3 Parameter Dependence of the Energy Eigenvalues

Without working out the exact solution, we can already say something about the behavior of the energy of bound states as we change the parameters of our system, that is m, α and μ. The derivative of the energy with respect to a variable is easily calculated as the expectation value of the derivative of the Hamiltonian with respect to the parameter of interest, as stated by the Feynman-Hellmann theorem [18]

$$\frac{\partial E}{\partial \lambda} = \left\langle \frac{\partial \hat{H}}{\partial \lambda} \right\rangle, \tag{4.12}$$

which can be easily shown by using the normalization of the wave function and the chain rule for derivatives. λ represents an arbitrary parameter. To see how E changes with our parameters we just replace λ. For μ this gives

$$\begin{aligned}
\frac{\partial E}{\partial \mu} &= \left\langle \frac{\partial}{\partial \mu}\left(-\frac{\hat{\mathbf{p}}^2}{2\mu} + V(\hat{r})\right)\right\rangle \\
&= \left\langle \frac{\hat{\mathbf{p}}^2}{2\mu^2} \right\rangle \\
&= -\frac{1}{\mu}\left\langle \left(\hat{H} - V(\hat{r})\right)\right\rangle \\
&= -\frac{1}{\mu}\overbrace{(E - \langle V(\hat{r})\rangle)}^{\langle \hat{T}\rangle} < 0,
\end{aligned} \tag{4.13}$$

where we used the linearity of the expectation value in the penultimate step. When we consider different values for μ, this implies that for larger μ the system becomes more bound.

When we change the mediator mass m, we get

$$\frac{\partial E}{\partial m} = \left\langle \frac{\partial \hat{V}}{\partial m} \right\rangle = \left\langle -r \left(-\frac{\alpha}{r} \right) e^{-mr} \right\rangle = \alpha \left\langle e^{-mr} \right\rangle > 0. \tag{4.14}$$

This means that if we make the mediator mass larger, the state becomes less bound. This agrees with what one would think intuitively, as m increases, the range of the Yukawa potential becomes smaller. If we decrease m the range of the Yukawa potential becomes larger and the energy becomes greater. Corresponding to a stronger bound system, as the binding energy is given by $-E$.

Lastly we consider the change of energy with the parameter α, that is the strength of the interaction. The derivative becomes

$$\frac{\partial E}{\partial \alpha} = \left\langle \frac{\partial \hat{V}}{\partial \alpha} \right\rangle = \left\langle -\frac{1}{r} e^{-mr} \right\rangle = \frac{1}{\alpha} \left\langle \hat{V} \right\rangle < 0, \tag{4.15}$$

which again agrees with intuition. As α becomes larger, the interaction is stronger. $\frac{\partial E}{\partial \alpha}$ is then negative, meaning the energy becomes smaller, that is, more negative.

These three derivatives tell us a lot about the qualitative behavior of the system. This will provide a useful check for the numerical solutions that will be constructed as explained in Section 4.2.

4.2 Numerical Solution to the Radial Equation

Now we can start solving for the radial wave function $R(r)$.

4.2.1 Discretizing the Problem

We are now tasked with solving the radial Equation 4.7 for our Yukawa potential, that is

$$-\frac{1}{2\mu} \frac{d^2 u(r)}{dr^2} + \left(V(r) + \frac{\hbar^2}{2\mu} \frac{l(l+1)}{r^2} \right) u(r) = E u(r). \tag{4.16}$$

Solving the problem analytically is a difficult task. There are exact solutions in terms of power series using hidden supersymmetry of the Yukawa potential, see Ref. [19]. We will not go down this path. Instead, the solution will be calculated numerically. To do so, the radial interval $r \in [0, \infty)$ is discretized. This is done by introducing a small step size $a = \frac{r_{max}}{N}$ between lattice points. Instead of the continuous interval, we now get a set of lattice points $\{0, a, 2a, 3a, \cdots, Na, (N+1)a\}$. The point $r = (N+1)a$ will take the role of the point at infinity. This point will be used to impose the appropriate boundary conditions. The value of r_{max} must be chosen such, that we can impose the boundary condition properly. This will be made more precise later on. For a visual representation of this discretization procedure, see Figure 4.1.

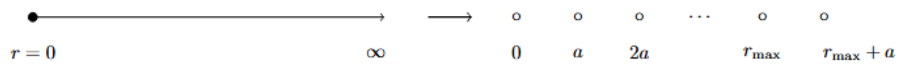

Figure 4.1: A visual representation of the discretization procedure of the radial distance. The point $r_{max} + a$ will play the role of the point at infinity.

Before looking at what such a discretization procedure does to $u(r)$ and the radial equation, we need to consider the boundary conditions on $u(r)$. First, since $u(r) = rR(r)$ we have

$u(0) = 0$. Second, from the normalization of $R(r)$ we find

$$1 = \int_0^\infty r^2 |R(r)|^2 \mathrm{d}r = \int_0^\infty |rR(r)|^2 \mathrm{d}r = \int_0^\infty |u(r)|^2 \mathrm{d}r.$$

The factor r^2 comes from the spherical volume element. From this we conclude that $u(r)$ must be square integrable. As we consider bound states, a nonvanishing probability density at infinite distance is unphysical. Therefore, the second boundary condition is $\lim_{r\to\infty} u(r) = 0$.

Using the discretization of the radial distance and the boundary conditions, we can look what this does to the wave function. Instead of a continuous function, the wave function now becomes a $N + 2$ component vector:

$$u(r) \mapsto \begin{pmatrix} u(0) \\ u(a) \\ u(2a) \\ \vdots \\ u(r_{max}) \\ u(r_{max} + a) \end{pmatrix}, \tag{4.17}$$

which we call again $u(r)$, but this time it is only defined at the lattice points. The boundary conditions now imply that the first and last component of $u(r)$ are zero. We exclude these points from our vector, so we are left with a N component vector. For a general $u_i \equiv u(r_i) = u(ia)$ the radial equation becomes

$$-\frac{1}{2\mu}\left(\frac{d^2u_i}{dr^2} - \frac{l(l+1)}{r_i^2}u_i\right) - \frac{\alpha}{r_i}e^{-mr_i} = Eu_i. \tag{4.18}$$

Only the second derivative still needs to be replaced by a discrete analogue. To find such an expression for the second derivative of u_i we can look at the Taylor expansion of $u(r_i + a)$ and $u(r_i - a)$ around $r = r_i$ [20],

$$u(r_i + a) = u(r_i) + \frac{du(r_i)}{dr}a + \frac{1}{2}\frac{d^2u(r_i)}{dr^2}a^2 + \mathcal{O}(a^3); \tag{4.19}$$

$$u(r_i - a) = u(r_i) - \frac{du(r_i)}{dr}a + \frac{1}{2}\frac{d^2u(r_i)}{dr^2}a^2 + \mathcal{O}(a^3). \tag{4.20}$$

Adding the two equations and solving for $\frac{d^2u(r_i)}{dr^2}$ gives a discrete expression for the second derivative:

$$\frac{d^2u(r_i)}{dr^2} \approx \frac{u_{i+1} - 2u_i + u_{i-1}}{a^2}, \tag{4.21}$$

where the error is on the order of a^2, as the third derivatives cancel when adding the two Taylor expansions.[iv] The problem to be solved is now reduced to solving

$$\left(-\frac{1}{2\mu}\left(-\frac{2}{a^2} - \frac{l(l+1)}{r_i^2}\right) - \frac{\alpha}{r_i}e^{-mr_i}\right)u_i - \frac{1}{2\mu a^2}u_{i+1} - \frac{1}{2\mu a^2}u_{i-1} = Eu_i, \tag{4.22}$$

which is actually a system of equations:

$$\left(\mathrm{diag}\left(-\frac{1}{2\mu}\left(-\frac{2}{a^2} - \frac{l(l+1)}{r_i^2}\right) - \frac{\alpha}{r_i}e^{-mr_i}\right)_{i=1}^{N} - \frac{1}{2\mu a^2}\begin{pmatrix} 0 & 1 & 0 & 0 & \cdots & 0 \\ 1 & 0 & 1 & 0 & \cdots & 0 \\ 0 & 1 & 0 & 1 & \cdots & 0 \\ 0 & 0 & 1 & 0 & \cdots & 0 \\ \vdots & \vdots & \vdots & \vdots & \ddots & 1 \\ 0 & 0 & 0 & \cdots & 1 & 0 \end{pmatrix}\right)\begin{pmatrix} u_1 \\ u_2 \\ \vdots \\ u_N \end{pmatrix} = E\begin{pmatrix} u_1 \\ u_2 \\ \vdots \\ u_N \end{pmatrix}. \tag{4.23}$$

[iv] This is, because the fourth derivatives are of order $\mathcal{O}(a^4)$ and we divide by a^2.

The discretized problem is now that of solving for the eigenvalues and corresponding eigenvectors of the matrix on the left hand side of Equation 4.23. The eigenvectors are normalized according to

$$1 = \int_0^\infty |u(r)|^2 \mathrm{d}r \approx \sum_{i=1}^{N} |u_i|^2 \Delta r = \sum_{i=1}^{N} |u_i|^2 a. \tag{4.24}$$

Later we will be interested in calculating production and decay rates of bound states. For this we need the quantities $|R(0)|^2$ and $|R'(0)|^2$ (and higher derivatives for D-wave, F-wave states etc.), so it is important to see how these follow from the numerical solution. As $R(r) = u(r)/r$, it is problematic to evaluate this at the origin. We approximate this by

$$|R(0)|^2 \approx \frac{|u_1|^2}{r_1^2}, \tag{4.25}$$

which becomes a better approximation for larger N, as $\lim_{N\to\infty} r_1 = 0$. For the derivative evaluated at the origin, we use the forward derivative, which yields [20]

$$|R'(0)|^2 \approx \left|\frac{u_1}{r_1 a}\right|^2. \tag{4.26}$$

The Python code implementing this numerical approach to solving the Schrödinger equation is given in Appendix B.

4.2.2 Exact Solutions with a Yukawa Potential

An analysis of how the results from the code compare to the solutions to known problems (the hydrogen atom and harmonic oscillator) is given in Appendix C. Now we will check the results of the discretization approach against the exact solution as presented in Ref. [19]. There, hidden supersymmetry of the Yukawa potential is used to find the exact wave functions and energy levels as a power series in the parameter $\delta = \frac{m}{\mu\alpha}$. The wave function is given by

$$\psi_{nlm}(\mathbf{r}, \delta, k) = \sqrt{\left(\frac{2}{na_0}\right)^3 \frac{(n-l-1)!}{(n+l)!2n}} \rho^l e^{-\rho/2} N_{n-l-1}^{2l+1}(\rho, \delta, k) Y_l^m(\theta, \phi), \tag{4.27}$$

where $\rho = \frac{2r}{na_0}$ and a_0 the Bohr radius which depends on the parameters of the problem, $a_0 = \frac{1}{\mu\alpha}$. $N_{n-l-1}^{2l+1}(\rho, \delta, k)$ is a polynomial in δ that reduces to the associated Laguerre polynomials in the case $\delta = 0$. These polynomials are given to order k in δ. For the first few energy states these polynomials are given explicitly in Ref. [19] up to order $k = 5$. As for the energy levels, they are also a power series in δ, which is given in the same paper up to order $k = 10$. As these formulas are very long and little illuminating, they are not repeated here. An important note is that, as we consider only the solution up to order $k = 5$, we need to be sure that higher powers of δ are negligible, when compared to our numerical solution. For each energy level, the critical screening length δ_{nl} indicates when we approach the continuum. The critical screening lengths as calculated in Ref. [19] are given in Table 2. As we only consider up to order $k = 5$, the normalization factor of Equation 4.27 is only valid sufficiently far away from the critical screening length, where higher order terms are negligible. When we approach the critical screening length, this normalization no longer normalizes the wave function and the power series is no longer accurate. This we need to take into account when comparing the numerical approach to these power series.

First, we compare the radial probability densities as calculated from the analytical solution to order $k = 5$ to those as found from the numerical calculation. The result is given in Figure 4.2.

n	l	δ_{nl}	n	l	δ_{nl}
1	0	1.1906124207 (2)	7	0	0.02586938 (2)
2	0	0.3102092834 (2)		1	0.024026435 (1)
	1	0.220118 (1)		2	0.0221591 (1)
3	0	0.139450295 (1)		3	0.02034124 (1)
	1	0.11265 (1)		4	0.01864606 (1)
	2	0.0913384 (2)		5	0.017095093 (1)
4	0	0.0788281106 (1)		6	0.015691075 (2)
	1	0.067827 (1)	8	0	0.0198221 (1)
	2	0.058099 (1)		1	0.01862667 (2)
	3	0.049830665 (4)		2	0.01738685 (4)
5	0	0.0505831707 (2)		3	0.01615594 (4)
	1	0.045155 (1)		4	0.01498071 (1)
	2	0.0400197 (1)		5	0.01388348 (1)
	3	0.0353883 (1)		6	0.012871446 (2)
	4	0.031343456 (1)		7	0.011944528 (1)
6	0	0.035183478 (1)	9	0	0.0156708 (1)
	1	0.0321562 (2)		1	0.0148561 (1)
	2	0.0291623 (2)		2	0.01399716 (1)
	3	0.02635015 (2)		3	0.01312892 (2)
	4	0.02379897 (2)		4	0.01228586 (1)
	5	0.021524523 (3)		5	0.011485698 (1)
				6	0.010736127 (1)
				7	0.0100397512 (1)
				8	0.0093959992 (1)

Table 2: Critical screening lengths δ_{nl} for the first 9 values of n and corresponding l values [19].

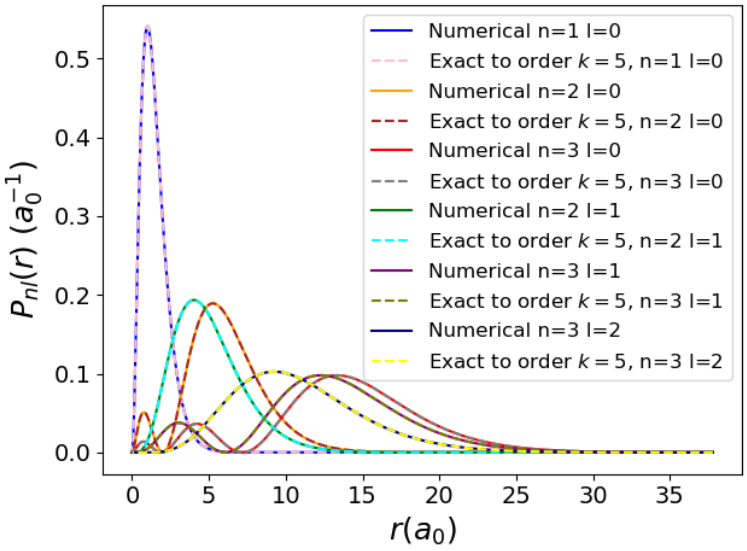

Figure 4.2: The radial probability densities $r^2|R_{nl}(r)|^2$ from the numerical calculation and the analytical calculation to order $k = 5$ overlain for $\delta = 0.0274$.

Here we see a good agreement between the numerical approach and the exact solution. In this plot the parameters were chosen as follows: $m = m_e/5000$, $\mu = m_e$ and $\alpha = 1/137$, which gives $\delta \approx 0.0274$. These values were chosen such that the Yukawa potential supports bound states up to $n = 3, l = 2$. They have no physical significance. If we compare with Table 2, we see that, indeed, for the first three n states the exact solution to order $k = 5$ to be a good approximation. Some more comparisons between the approximate and exact solution are given in Appendix D. δ is varied by varying one of the three parameters α, m and μ. There we see a divergence between the exact and numerical solution for increasing δ.

To quantify the accuracy of the numerical calculation better, we look at the relative error between the two methods. Only the small δ regime is considered as this is where the wave function 4.27 is accurate to order $k = 5$. The result for two choices of δ are shown in the figures 4.3 and 4.4.

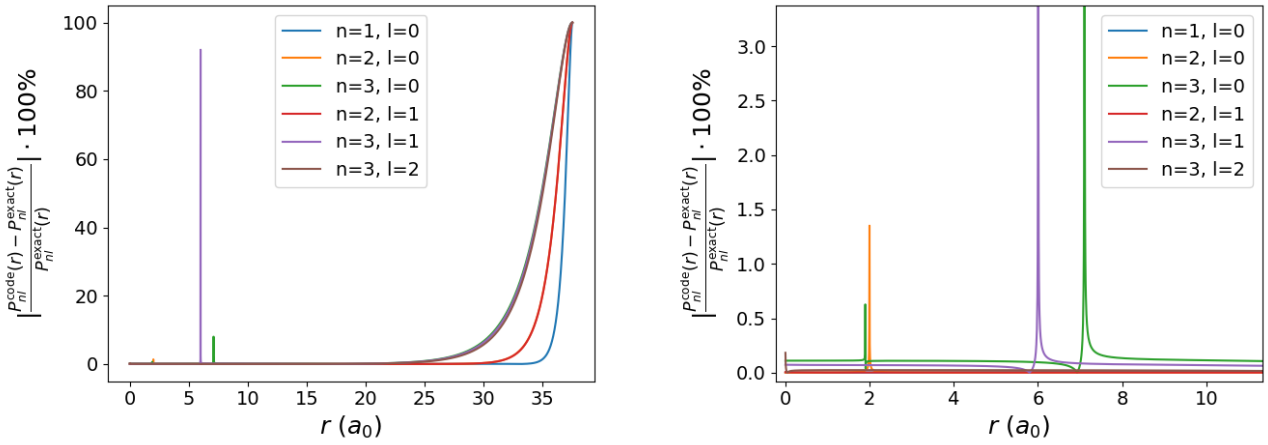

(a) (b)

Figure 4.3: Relative error $\left(\left|\frac{P_{nl}^{Code}(r)-P_{nl}^{Exact}(r)}{P_{nl}^{Exact}(r)}\right| \cdot 100\%\right)$ in the radial probability density for the exact and numerical approach. Here $\delta = 0.0069$ and $N = 6000$. The right plot is a zoom-in of the left plot.

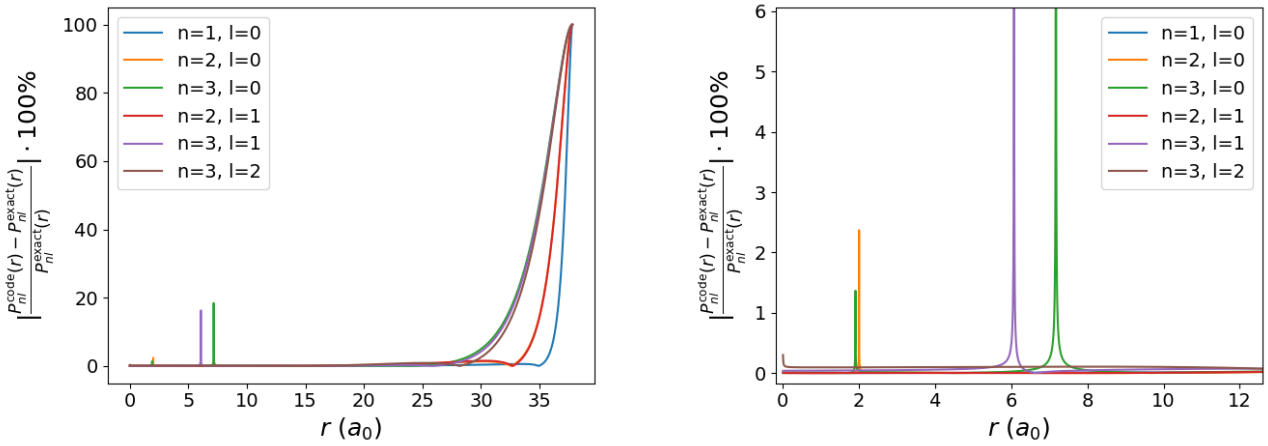

(a) (b)

Figure 4.4: Relative error ($\left|\frac{P_{nl}^{Code}(r)-P_{nl}^{Exact}(r)}{P_{nl}^{Exact}(r)}\right| \cdot 100\%$) in the radial probability density for the exact and numerical approach. Here $\delta = 0.0274$ and $N = 6000$. The right plot is a zoom-in of the left plot.

In both cases we see the same behavior as shown in Appendix C for the hydrogen and harmonic oscillator cases. For large r, where the wave functions are approximately zero, the error becomes large due to the comparison of such small numbers, we run in to problems of the accuracy of numerical calculation. In both cases we also see narrow peaks again, these again correspond to the zeroes of the probability densities, as before. Close to the origin, the error for the $n = 3, l = 2$ state grows. The origin is the same as before. Apart from these cases, the numerical calculation does a very good job.

Lastly, we compare the numerically calculated energies to those given by the exact formula in Ref. [19]. The energy as function of δ, where δ is varied by varying one of the parameters m, μ or α, is given in figures 4.5, 4.6 and 4.7.

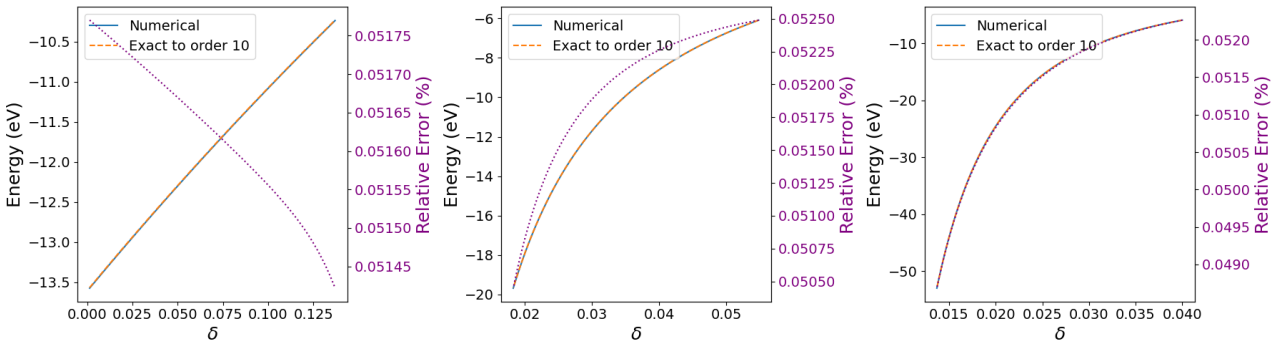

Figure 4.5: Bound state energy for $n = 1$ and $l = 0$ as calculated by the exact (orange dashed line) and numerical (blue line) approach. In purple the relative error between the two is shown. From left to right, δ is varied by varying m, μ and α, respectively.

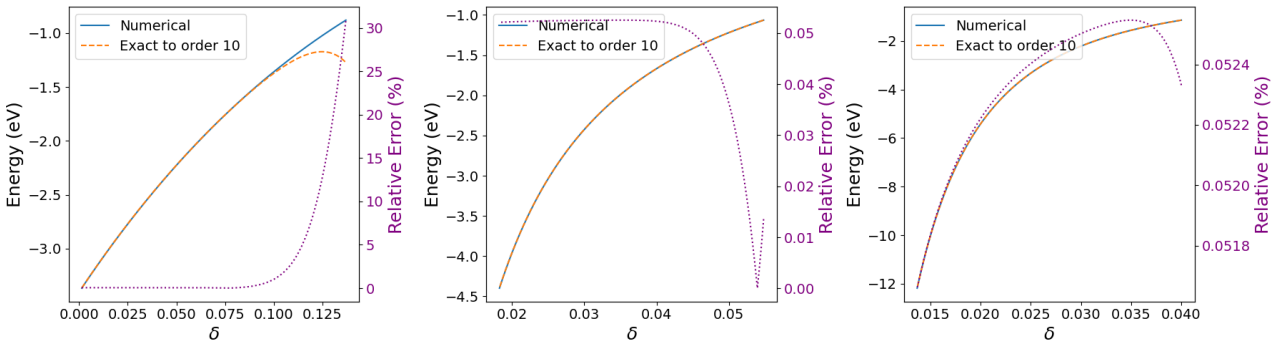

Figure 4.6: Bound state energy for $n = 2$ and $l = 0$ as calculated by the exact (orange dashed line) and numerical (blue line) approach. In purple the relative error between the two is shown. From left to right, δ is varied by varying m, μ and α, respectively.

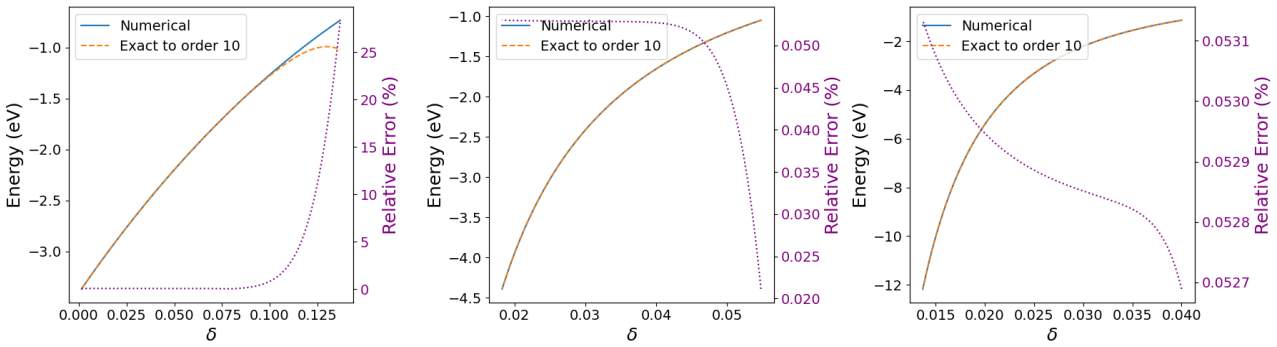

Figure 4.7: Bound state energy for $n = 2$ and $l = 1$ as calculated by the exact (orange dashed line) and numerical (blue line) approach. In purple the relative error between the two is shown. From left to right, δ is varied by varying m, μ and α, respectively.

As can be seen from these figures, in the regime of small δ, where the exact formula to order $k = 10$ can be expected to be valid, the numerical calculation agrees very well with the exact solution. For the numerical calculation $N = 6000$ was taken. A nice qualitative check is to realize that the results from these figures behave as was expected from the Feynman-Hellmann theorem, equations 4.15, 4.14 and 4.13. As m increases, δ increases as well, and we see from the figures that E becomes less negative, i.e. $\frac{\partial E}{\partial m} > 0$. For μ and α, an increase in these parameters correspond to decreasing δ. Again, in the corresponding plots we see that for decreasing δ, E becomes more negative, i.e. $\frac{\partial E}{\partial \mu} < 0$ and $\frac{\partial E}{\partial \alpha} < 0$.

All these checks we have done give the confidence to use the numerical calculation as an accurate approximation to the probability densities and corresponding energy eigenvalues for a system governed by the Yukawa potential with arbitrary parameters m, α and μ.

4.2.3 Energy Levels with a Yukawa Potential

Now, with the numerical approach at hand, we can have a look at the structure of the energy levels in a Yukawa potential. In this section, we will use the following values for the parameters: $\alpha = \frac{1}{137}$, $m = 0.511\text{KeV}$ and $\mu = 0.511\text{MeV}$. These values are chosen arbitrarily and have no significance. These are merely used to show the behavior of the energy levels. We will keep two of these parameters constant and vary just one at a time.

Varying the value of α gives the energy levels as shown in Figure 4.8. Here we see that

when we increase α the energy levels become more negative, in agreement with Equation 4.15. The spacing between energy levels also become larger in this case.

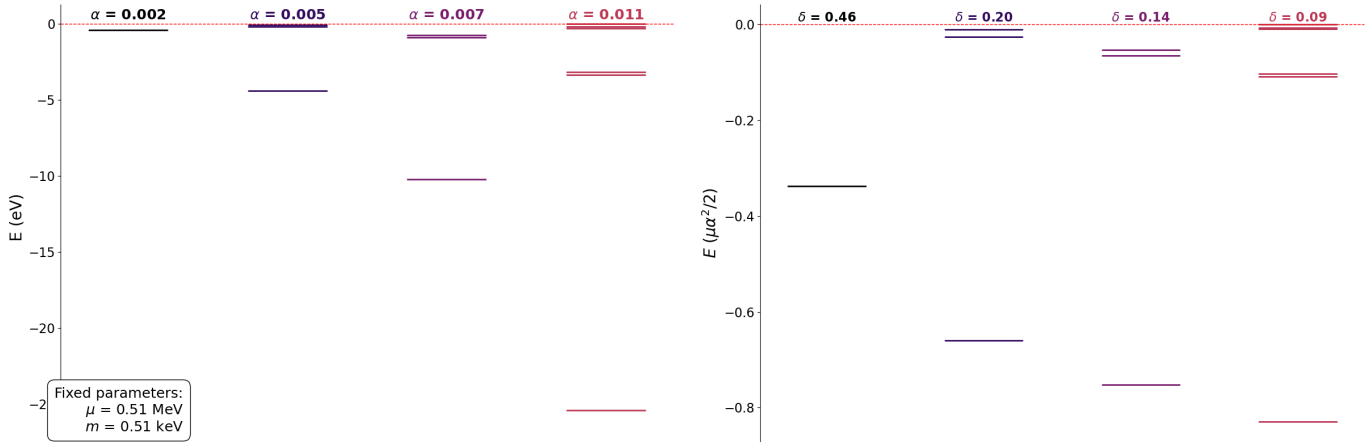

(a) (b)

Figure 4.8: The bound state energy levels as a function of α (left) and δ by varying α (right).

In the case of varying m, we see in Figure 4.9 that for a heavier mediator the energy levels become less negative.

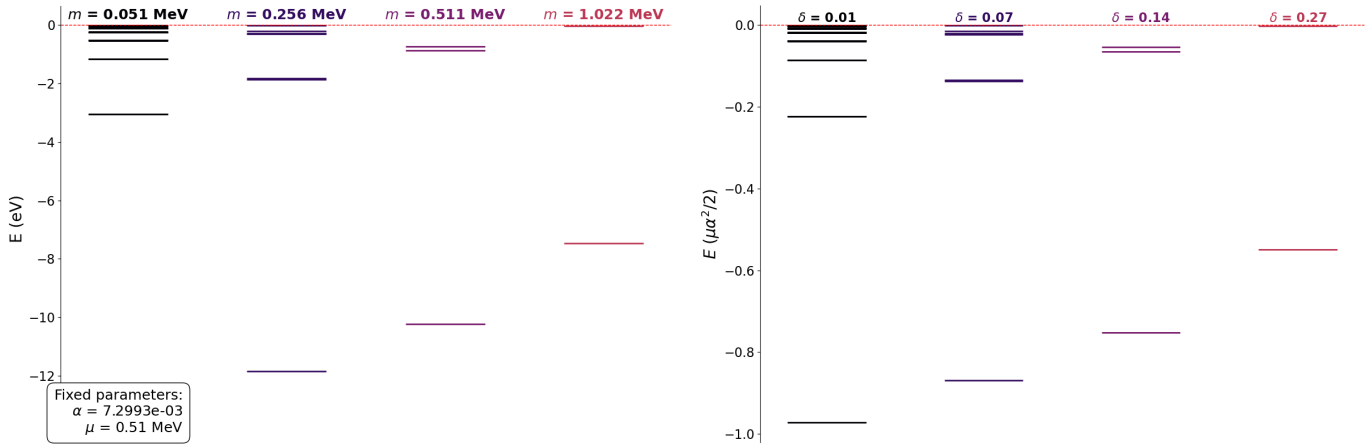

(a) (b)

Figure 4.9: The bound state energy levels as a function of m (left) and δ by varying m(right).

Lastly, varying μ results in Figure 4.10. Here again as expected, the heavier the mass of the constituents, the stronger bound the system is.

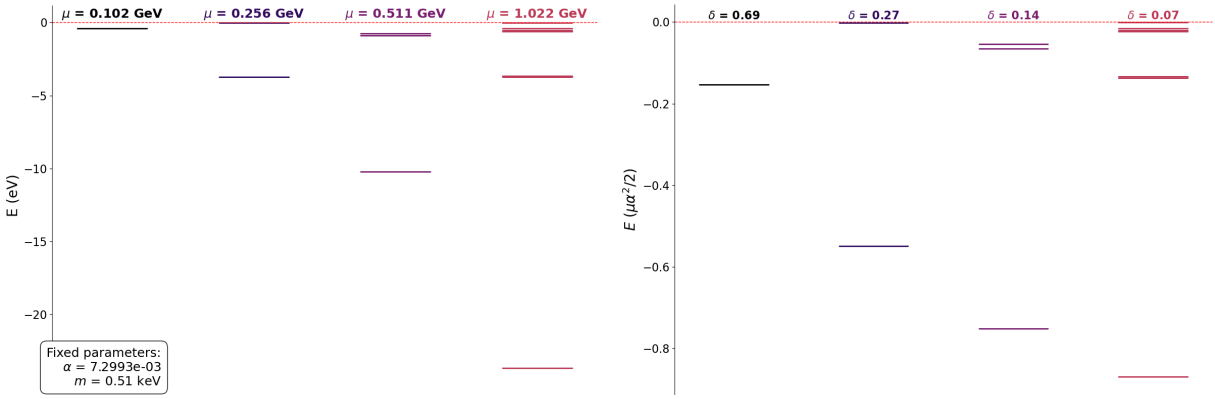

(a) (b)

Figure 4.10: The bound state energy levels as a function of μ (left) and δ by varying μ (right).

5 Dark Matter Bound State Production and Decay at Electron-Positron Colliders

Now we are in a position to start doing actual calculations. We are interested in the production and decay of dark matter bound states in electron-positron colliders.

5.1 Dark Matter Bound State Production

We start by considering the production of dark matter bound states. As we have seen before, the matrix element for producing the bound state can be calculated from the matrix element for producing the constituents. We will be interested in the lowest order processes that can contribute to the production. We consider two processes. The first is the production of a dark matter particle anti-particle pair together with a dark photon. The contributing diagrams are shown in Figure 5.1. Of course, there are also contributions from the diagrams where it is the electron or positron that radiates off the dark photon, but these are suppressed by an additional factor of ϵ.

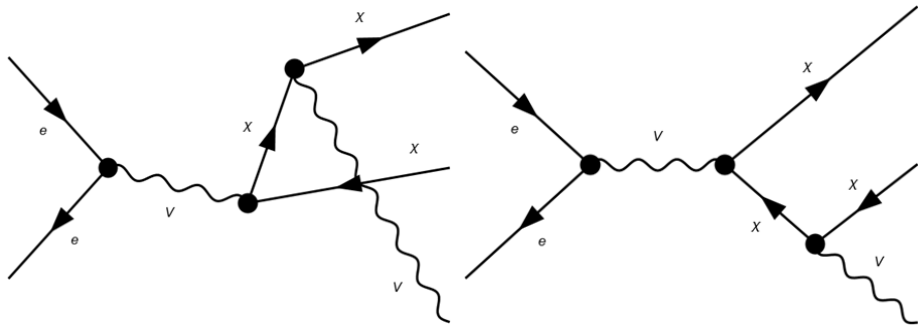

(a) (b)

Figure 5.1: The lowest order contributing diagrams for the process $e^+e^- \to \chi\bar{\chi}V$.

The other process we are interested in is that of the production of a dark matter particle anti-particle pair with an additional photon. The two lowest order contributing diagrams are shown in Figure 5.2.

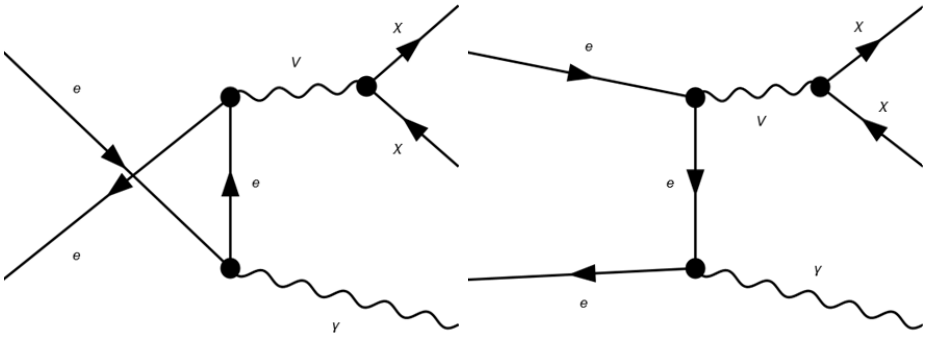

(a) (b)

Figure 5.2: The lowest order contributing diagrams for the process $e^+e^- \to \chi\bar{\chi}\gamma$.

By looking at the quantum numbers of our bound states, we can already say which of the two processes $e^+e^- \to \chi\bar{\chi}\gamma$ and $e^+e^- \to \chi\bar{\chi}V$ will contribute to its production. Our model

is invariant under parity and charge conjugation. This means we can use the C eigenvalues to determine which of the processes is allowed. For the bound state we have $P = (-1)^{L+1}$ and $C = (-1)^{L+S}$. If we look at the virtual dark photon in the two processes we know it has $C = -1$. This means that in the process $e^+e^- \to \chi\bar{\chi}V$ we need our final state bound state to have $C = 1$, such that together with the final state dark photon we have $C = (-1) \cdot 1 = -1$. This is only the case if $L + S$ is even. In the case of the process $e^+e^- \to \chi\bar{\chi}\gamma$ we need our bound state to have $C = -1$ to match the virtual dark photon. This happens only when $L + S$ is odd. Of course, we still need parity and angular momentum to be conserved, but with our C-parity argument we only have to calculate one process. If the matrix element turns out to be zero we know it can only be a higher order process that contributes to its production. These we will ignore here as they will be suppressed with respect to the other process that do happen at lowest order. For the first few L values the dominant process based on the C-parity argument is given in Table 3.

L	S	J^{PC}	Process
S	0	0^{-+}	$e^+e^- \to \chi\bar{\chi}V$
S	1	1^{--}	$e^+e^- \to \chi\bar{\chi}\gamma$
P	0	1^{+-}	$e^+e^- \to \chi\bar{\chi}\gamma$
P	1	0^{++}	$e^+e^- \to \chi\bar{\chi}V$
P	1	1^{++}	$e^+e^- \to \chi\bar{\chi}V$
P	1	2^{++}	$e^+e^- \to \chi\bar{\chi}V$
D	0	2^{-+}	$e^+e^- \to \chi\bar{\chi}V$
D	1	1^{--}	$e^+e^- \to \chi\bar{\chi}\gamma$
D	1	2^{--}	$e^+e^- \to \chi\bar{\chi}\gamma$
D	1	3^{--}	$e^+e^- \to \chi\bar{\chi}\gamma$

Table 3: The dominant process for producing bound states for the first few L values, based on the C-parity argument.

Now we will simplify the matrix element formula of Equation 3.31 for the different possible bound states.

We start with the case $L = 0$. In this case, Equation 3.31 is easily worked out and reduces to

$$\mathcal{M}_{BS}({}^{2S+1}S_J) = \frac{\sqrt{2M}}{2m}\mathrm{Tr}(f(0)P_{JM_J})\frac{R^*_{n0}(0)}{\sqrt{4\pi}}. \tag{5.1}$$

In the case of $L = 1$, Equation 3.31 reduces to

$$\mathcal{M}_{BS}({}^{2S+1}P_J) = -i\sqrt{\frac{3}{4\pi}}\frac{\sqrt{2M}}{2m}\sum_{M_L=-1}^{1}\sum_{M_S} C^{JM_J}_{1M_LSM_S}\mathrm{Tr}\left(\frac{\partial f(k)}{\partial k^\mu}\bigg|_{k=0} P_{SM_S}\right) R'^*_{n1}(0)\epsilon^\mu_{(M_L)}. \tag{5.2}$$

This still requires some work to get rid of the Clebsch-Gordan coefficients. The case without spin, i.e. the ${}^1P_1$ state is easy. In this case, the Clebsch-Gordan coefficients reduce to Kronecker deltas and the resulting matrix element is

$$\mathcal{M}_{BS}({}^1P_1) = -i\sqrt{\frac{3}{4\pi}}\frac{R'^*_{n1}(0)}{\sqrt{8m^3}}\mathrm{Tr}\left(\frac{\partial f(k)}{\partial k^\mu}\bigg|_{k=0}\gamma^5\right)\epsilon^\mu_{(M_J)}. \tag{5.3}$$

For the process $e^+e^- \to \chi\bar{\chi}\gamma$, this matrix element vanishes. This means that the production of the ${}^1P_1$ is suppressed with respect to other states. Intuitively, this makes sense, as we try to couple a $P = 1$ bound state to a $P = -1$ dark photon.

For $S = 1$ states the matrix element requires a bit more thought. We do here a similar procedure as we did earlier for rewriting the Clebsch-Gordan coefficients in terms of an inner product with spinors. However, this time we use polarization vectors. We write

$$C^{JM_J}_{1M_L1M_S} = \epsilon^{\mu*}_{(M_L)} M^{JM_J}_{\mu\nu} \epsilon^{\nu*}_{(M_S)}, \tag{5.4}$$

where we have introduced a two-index object $M^{JM_J}_{\mu\nu}$. Using the explicit Clebsch-Gordan coefficients from the literature for each combination (M_L, M_S) allows one to find the explicit form of $M^{JM_J}_{\mu\nu}$. The explicit form of $M^{JM_J}_{\mu\nu}$ can then be expressed in terms of outer products of polarization vectors. With this, it can be shown that

$$\sum_{M_J} M^{JM_J}_{\mu\nu} M^{JM_J*}_{\alpha\beta} = \begin{cases} \frac{1}{3}\Pi_{\mu\nu}\Pi_{\alpha\beta} & \text{if } J = 0 \\ \frac{1}{2}\left(\Pi_{\mu\alpha}\Pi_{\beta\nu} - \Pi_{\mu\beta}\Pi_{\nu\alpha}\right) & \text{if } J = 1 \\ \frac{1}{2}\left(\Pi_{\mu\alpha}\Pi_{\beta\nu} + \Pi_{\mu\beta}\Pi_{\nu\alpha}\right) - \frac{1}{3}\Pi_{\mu\nu}\Pi_{\alpha\beta} & \text{if } J = 2 \end{cases}. \tag{5.5}$$

Here $\Pi_{\mu\nu} = -g_{\mu\nu} + \frac{P_\mu P_\nu}{4m^2}$, this now allows us to do the polarization sum. Substituting Equation 5.4 back into the matrix element and performing the sums over M_S and M_L, using the completeness of the polarization vectors, we obtain the final form of the matrix element

$$\mathcal{M}_{BS}(^3P_J) = i\sqrt{\frac{3}{4\pi}}\frac{R'^*_{n1}(0)}{\sqrt{8m^3}}\mathrm{Tr}\left(\left.\frac{\partial f(k)}{\partial k^\mu}\right|_{k=0}\gamma_\alpha\right)\left(-g^{\alpha\rho} + \frac{P^\alpha P^\rho}{4m^2}\right) M^{JM_J}_{\rho\sigma}\left(-g^{\mu\sigma} + \frac{P^\mu P^\sigma}{4m^2}\right). \tag{5.6}$$

The highest L state we will focus on are the $L = 2$ states. In this case the matrix element formula becomes

$$\begin{aligned}\mathcal{M}_{BS}(^{2S+1}D_J) = &-\frac{1}{4}\frac{\sqrt{2M}}{2m}\sqrt{\frac{15}{2\pi}}\sum_{M_L M_S} C^{JM_J}_{2M_L SM_S}\mathrm{Tr}\left(\left.\frac{\partial^2 f(k)}{\partial k^{\mu_1}\partial k^{\mu_2}}\right|_{k=0} P_{SM_S}\right) \\ &\cdot R''^*_{n2}(0)\left(-g^{\mu_1\nu_1} + \frac{P^{\mu_1}P^{\nu_1}}{M^2}\right) M^{2M_L}_{\nu_1\nu_2}\left(-g^{\mu_2\nu_2} + \frac{P^{\mu_2}P^{\nu_2}}{M^2}\right).\end{aligned} \tag{5.7}$$

The case without spin is easily worked out, as the Clebsch-Gordan coefficients then become Kronecker deltas. The resulting matrix element is

$$\begin{aligned}\mathcal{M}_{BS}(^1D_2) = &-\frac{1}{4}\frac{1}{\sqrt{8m^3}}\sqrt{\frac{15}{2\pi}}\mathrm{Tr}\left(\left.\frac{\partial^2 f(k)}{\partial k^{\mu_1}\partial k^{\mu_2}}\right|_{k=0}\gamma^5\right) \\ &\cdot R''^*_{n2}(0)\left(-g^{\mu_1\nu_1} + \frac{P^{\mu_1}P^{\nu_1}}{M^2}\right) M^{2M_J}_{\nu_1\nu_2}\left(-g^{\mu_2\nu_2} + \frac{P^{\mu_2}P^{\nu_2}}{M^2}\right),\end{aligned} \tag{5.8}$$

where for $M^{2M_J}_{\nu_1\nu_2}$ the polarization sum is that of the previous section.

The $S = 1$ D-states again require some work to get rid of the Clebsch-Gordan coefficients. This time we rewrite them as

$$C^{JM_J}_{2M_L1M_S} = M^{2M_L*}_{\rho\sigma} N^{JM_J,\rho\sigma\lambda} \epsilon^*_{(M_S)\lambda}. \tag{5.9}$$

Here we have introduced the three index object $N^{JM_J,\rho\sigma\lambda}$ for which we need the polarization sums. Rewriting the Clebsch-Gordan coefficients this way allows us to do the sums over M_S and M_L, using in the M_L sum the $J = 2$ polarization sum for the two index objects we introduced for the P-states. The resulting matrix element is

$$\begin{aligned}\mathcal{M}_{BS}(^3D_J) = &-\frac{1}{\sqrt{8m^3}}\frac{1}{4}\sqrt{\frac{15}{2\pi}}\mathrm{Tr}\left(\left.\frac{\partial^2 f(k)}{\partial k^{\mu_1}\partial k^{\mu_2}}\right|_{k=0}\gamma^\alpha\right) R''^*_{n2}(0)\Pi^{\mu_1\nu_1}\Pi^{\mu_2\nu_2}\Pi_{\alpha\lambda} \\ &\cdot\left(\frac{1}{2}\left(\Pi_{\rho\nu_2}\Pi_{\nu_1\sigma} + \Pi_{\nu_1\rho}\Pi_{\sigma\nu_2}\right) - \frac{1}{3}\Pi_{\nu_1\nu_2}\Pi_{\sigma\rho}\right) N^{JM_J,\rho\sigma\lambda}.\end{aligned} \tag{5.10}$$

The polarization sums for the three index polarization tensors are known and can be worked out from the identities given in Ref. [21]. It can be shown that the contraction with the indexed objects outside of the trace in Equation 5.10 does not change the expression. Hence we conclude the same polarization sums must hold for our three index objects. The polarization sums are then given by

$$\sum_{M_J} N^{JM_J,\rho\sigma\lambda} N^{*JM_J,\mu\nu\kappa} = \begin{cases} \frac{3}{20}\Bigg(\Pi^{\rho\lambda}\left(\Pi^{\mu\kappa}\Pi^{\sigma\nu}+\Pi^{\nu\kappa}\Pi^{\sigma\mu}-\frac{2}{3}\Pi^{\mu\nu}\Pi^{\sigma\kappa}\right) \\ \quad +\Pi^{\sigma\lambda}\left(\Pi^{\mu\kappa}\Pi^{\rho\nu}+\Pi^{\nu\kappa}\Pi^{\rho\mu}-\frac{2}{3}\Pi^{\mu\nu}\Pi^{\rho\kappa}\right) \\ \quad -\frac{2}{3}\Pi^{\rho\sigma}\left(\Pi^{\mu\kappa}\Pi^{\lambda\nu}+\Pi^{\nu\kappa}\Pi^{\lambda\mu}-\frac{2}{3}\Pi^{\mu\nu}\Pi^{\lambda\kappa}\right)\Bigg) & \text{if } J=1 \\ \frac{1}{6M^2}\Bigg(\epsilon^{\alpha\sigma\lambda\beta}P_\alpha g_{\xi\beta}\left(\frac{1}{2}\left(\Pi^{\rho\mu}\Pi^{\iota\xi}+\Pi^{\rho\iota}\Pi^{\xi\mu}\right)-\frac{1}{3}\Pi^{\rho\xi}\Pi^{\mu\iota}\right)\epsilon^{\zeta\nu\kappa\eta}P_\zeta g_{\iota\eta} \\ \quad +\epsilon^{\alpha\sigma\lambda\beta}P_\alpha g_{\xi\beta}\left(\frac{1}{2}\left(\Pi^{\rho\nu}\Pi^{\iota\xi}+\Pi^{\rho\iota}\Pi^{\xi\nu}\right)-\frac{1}{3}\Pi^{\rho\xi}\Pi^{\nu\iota}\right)\epsilon^{\zeta\mu\kappa\eta}P_\zeta g_{\iota\eta} \\ \quad +\epsilon^{\alpha\rho\lambda\beta}P_\alpha g_{\xi\beta}\left(\frac{1}{2}\left(\Pi^{\sigma\mu}\Pi^{\iota\xi}+\Pi^{\sigma\iota}\Pi^{\xi\mu}\right)-\frac{1}{3}\Pi^{\sigma\xi}\Pi^{\mu\iota}\right)\epsilon^{\zeta\nu\kappa\eta}P_\zeta g_{\iota\eta} \\ \quad +\epsilon^{\alpha\rho\lambda\beta}P_\alpha g_{\xi\beta}\left(\frac{1}{2}\left(\Pi^{\sigma\nu}\Pi^{\iota\xi}+\Pi^{\sigma\iota}\Pi^{\xi\nu}\right)-\frac{1}{3}\Pi^{\sigma\xi}\Pi^{\nu\iota}\right)\epsilon^{\zeta\mu\kappa\eta}P_\zeta g_{\iota\eta}\Bigg) & \text{if } J=2 \\ \frac{1}{6}\Bigg(\Pi^{\rho\mu}\Pi^{\sigma\nu}\Pi^{\lambda\kappa}+\Pi^{\rho\mu}\Pi^{\sigma\kappa}\Pi^{\lambda\nu}+\Pi^{\rho\nu}\Pi^{\sigma\mu}\Pi^{\lambda\kappa} \\ \quad +\Pi^{\rho\nu}\Pi^{\sigma\kappa}\Pi^{\lambda\mu}+\Pi^{\rho\kappa}\Pi^{\sigma\nu}\Pi^{\lambda\mu}+\Pi^{\rho\kappa}\Pi^{\sigma\mu}\Pi^{\lambda\nu}\Bigg) \\ -\frac{1}{15}\Bigg(\Pi^{\rho\sigma}\Pi^{\lambda\kappa}\Pi^{\mu\nu}+\Pi^{\rho\sigma}\Pi^{\lambda\nu}\Pi^{\mu\kappa}+\Pi^{\rho\sigma}\Pi^{\lambda\mu}\Pi^{\nu\kappa} \\ \quad +\Pi^{\rho\lambda}\Pi^{\sigma\kappa}\Pi^{\mu\nu}+\Pi^{\rho\lambda}\Pi^{\sigma\nu}\Pi^{\mu\kappa}+\Pi^{\rho\lambda}\Pi^{\sigma\mu}\Pi^{\nu\kappa} \\ \quad +\Pi^{\sigma\lambda}\Pi^{\rho\kappa}\Pi^{\mu\nu}+\Pi^{\sigma\lambda}\Pi^{\rho\nu}\Pi^{\mu\kappa}+\Pi^{\sigma\lambda}\Pi^{\rho\mu}\Pi^{\nu\kappa}\Bigg) & \text{if } J=3 \end{cases} \tag{5.11}$$

Calculations for the ${}^3D_2$ state shows that the lowest order diagrams do not contribute.

These simplified matrix element formulas can now be directly applied to calculate differential cross sections and decay rates at electron-positron colliders.

5.2 Decay of Dark Matter Bound States

Now we take a look at the decay of bound states. We consider decays to dark photons only. Decays to standard model particles will be suppressed with factors of ϵ. We can again, to lowest order, consider two processes. The Feynman diagrams for these process are shown in figures 5.3 and 5.4.

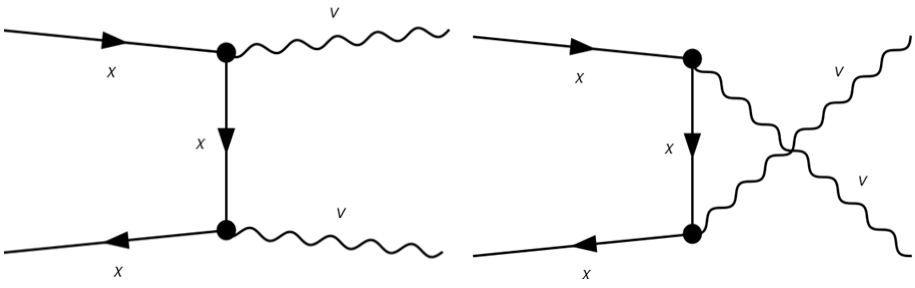

Figure 5.3: The lowest order contributing diagrams for the process $\chi\bar{\chi} \to 2V$.

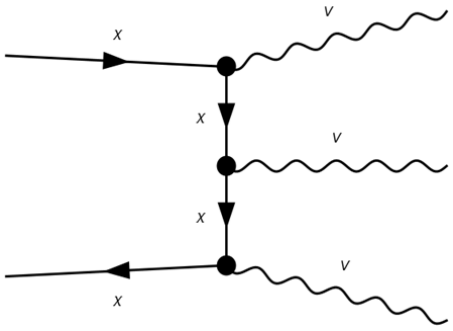

Figure 5.4: One of the six lowest order contributing diagrams for the process $\chi\bar{\chi} \to 3V$.

The different bound states can decay via one of these processes depending on their C-parity. In the case of a two dark photon final state we have $C = 1$. Bound states with $C = 1$, that is, $L + S$ even, can decay via this process. For the three dark photon final state, the final state has $C = -1$. Therefore, bound states with odd $L + S$ can decay via this process. The different dark matter bound states and the process through which they decay are given in tabulated in Table 4.

L	S	J^{PC}	Process
S	0	0^{-+}	$\chi\bar{\chi} \to 2V$
S	1	1^{--}	$\chi\bar{\chi} \to 3V$
P	0	1^{+-}	$\chi\bar{\chi} \to 3V$
P	1	0^{++}	$\chi\bar{\chi} \to 2V$
P	1	1^{++}	$\chi\bar{\chi} \to 2V$
P	1	2^{++}	$\chi\bar{\chi} \to 2V$
D	0	2^{-+}	$\chi\bar{\chi} \to 2V$
D	1	1^{--}	$\chi\bar{\chi} \to 3V$
D	1	2^{--}	$\chi\bar{\chi} \to 3V$
D	1	3^{--}	$\chi\bar{\chi} \to 3V$

Table 4: The dominant decay process for bound states for the first few L values, based on the C-parity argument.

The calculation of the matrix elements is done by simplifying Equation 3.32 like we did in the previous section. For the $C = 1$ states we find, in the bound state rest frame, the following decay rates.

$$\Gamma(^1S_0 \to 2V) = \frac{4\alpha_D^2 |R_{n0}(0)|^2 (m_\chi^2 - m_V^2)^{3/2}}{m_\chi (m_V^2 - 2m_\chi^2)^2}; \tag{5.12}$$

$$\Gamma(^3P_0 \to 2V) = \frac{24|R'_{n1}(0)|^2 \alpha_D^2 \sqrt{m_\chi^2 - m_V^2}\left(-8m_V^2 m_\chi^2 + 3m_V^4 + 6m_\chi^4\right)}{m_\chi \left(m_V^2 - 2m_\chi^2\right)^4}; \tag{5.13}$$

$$\Gamma(^3P_1 \to 2V) = \frac{16|R'_{n1}(0)|^2 \alpha_D^2 m_V^2 \left(m_\chi^2 - m_V^2\right)^{5/2}}{m_\chi^3 \left(m_V^2 - 2m_\chi^2\right)^4}; \tag{5.14}$$

$$\Gamma(^3P_2 \to 2V) = \frac{24|R'_{n1}(0)|^2 \alpha_D^2 \sqrt{m_\chi^2 - m_V^2}\left(-6m_V^2 m_\chi^2 + 3m_V^4 + 8m_\chi^4\right)}{5m_\chi \left(m_V^2 - 2m_\chi^2\right)^4}; \tag{5.15}$$

$$\Gamma(^1D_2 \to 2V) = \frac{64\alpha_D^2 |R''_{n2}(0)|^2 (m_\chi^2 - m_V^2)^{7/2}}{m_\chi (m_V^2 - 2m_\chi^2)^6}. \tag{5.16}$$

Here we have used that the bound state mass is approximately $2m_\chi$, i.e. we have neglected the binding energy.

These will prove to be important when considering whether or not bound states decay within detectors. For the three dark photon decay the calculation gets complicated and is not practical to do analytically. For the three dark photon decay of the $^3S_1$ decay one may refer to Ref. [8].

6 Dark Matter Bound States at Belle II

With a complete description of the dark matter bound states at our disposal, we can now take it to experiment. The first experiment we will look at is Belle II.

6.1 The Belle II Experiment

Belle II is an experiment located in Tsukuba, Japan. It is an electron-positron collider designed to study the properties of B-mesons. It operates at a center-of-mass energy of $\sqrt{s} = 10.58\,\text{GeV}$ [22]. A schematic view is given in Figure 6.1.

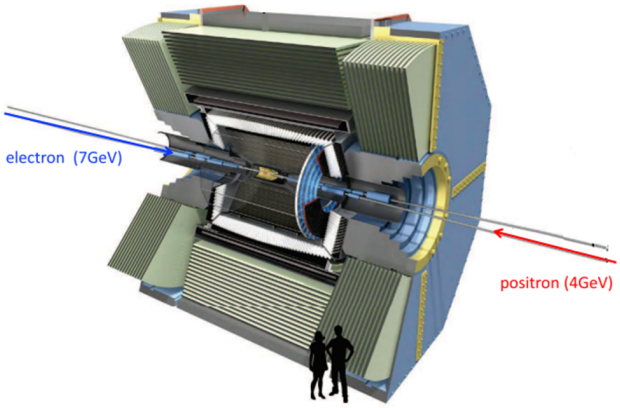

Figure 6.1: A schematic view of the Belle II experiment. The electron and positron beams have different energies, 7 GeV and 4 GeV respectively. This corresponds to a center-of-mass energy of $\sqrt{s} = 10.58\,\text{GeV}$. Figure take from Ref. [23].

Belle II will be the first experiment where we will look at the signatures left by dark matter bound states.

6.2 Producing Bound States

To examine the signatures left by dark matter bound states, we must first look at producing them at Belle II. The first step is to look at the possible bound states that can be produced. We note that the center-of-mass energy at which Belle II operates is $\sqrt{s} = 10.58\,\text{GeV}$. We are looking at producing $\chi\bar{\chi}$ bound states with mass $m_{\chi\bar{\chi}} \approx 2m_\chi$. Earlier we saw that bound states are produced via either of the processes $e^+e^- \to \chi\bar{\chi}V$ or $e^+e^- \to \chi\bar{\chi}\gamma$. In both cases almost all the mass of the final state particles is contained in the bound state, as $m_\gamma = 0$ and $m_V \ll m_\chi$, where the latter follows from the inequality for the requirement of bound state formation. Therefore, we must have $m_\chi \lesssim 5\,\text{GeV}$ if bound states can form at Belle II. Now we can take another look at the parameter space (α_D, m_χ), where $m_V = 100\,\text{MeV}$. This is shown in Figure 6.2.

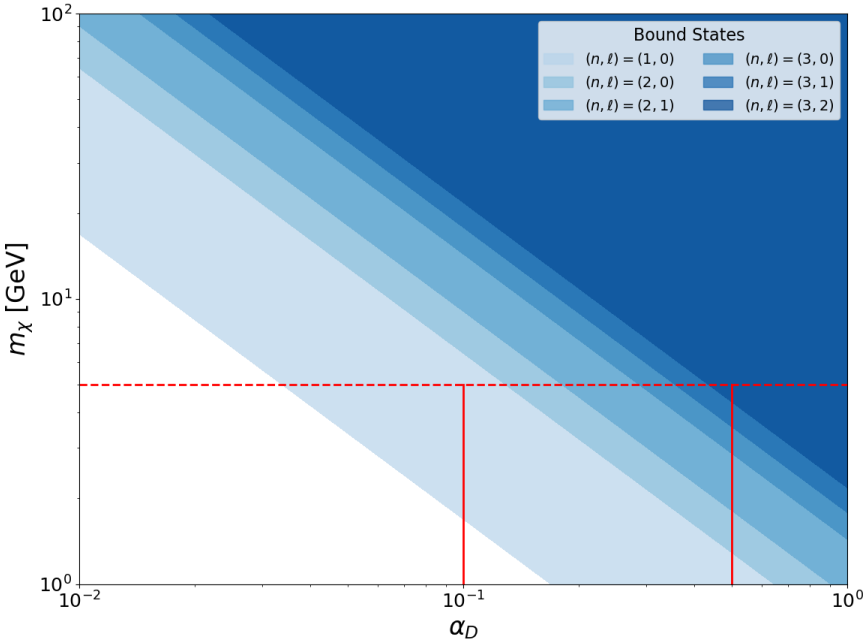

Figure 6.2: The parameter space with relevant benchmarks for Belle II. The red dashed line gives the value $m_\chi = 5\,\text{GeV}$ below which Belle II can produce bound states. The vertical red lines give two benchmarks for α_D, which will be studied.

We consider two benchmark values of α_D, $\alpha_D = 0.1$ and $\alpha_D = 0.5$. As can be seen from Figure 6.2, the stronger the interaction, the more bound states can form. We can look at the energy levels for the bound states and see if we can distinguish different bound states based on their invariant mass $m_{\chi\bar{\chi}} = 2m_\chi - E_B$, where E_B is the binding energy, i.e. the negative of the energy eigenvalue that follows from the Schrödinger equation. For $\alpha_D = 0.1$ we can only produce $n = 1$, $l = 0$ states, i.e. the ${}^1S_0$ and ${}^3S_1$ states. These we can not distinguish based on invariant mass, as they have the same energy eigenvalue. For the choice $\alpha_D = 0.5$ we can produce more bound states. The energy as a function of mass m_χ is shown in Figure 6.3.

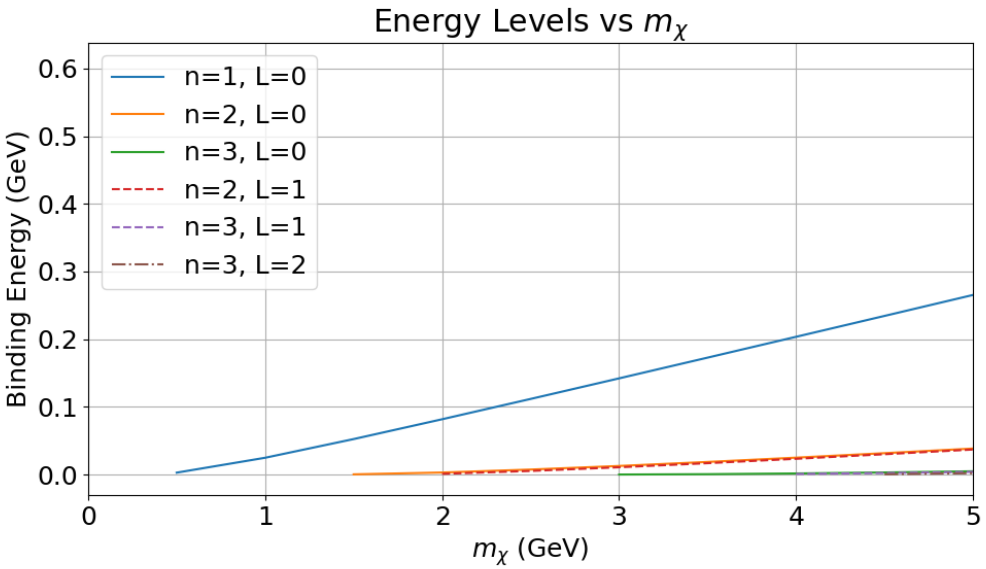

Figure 6.3: The binding energy levels of the different bound states for $\alpha_D = 0.5$ as a function of m_χ. The different lines start at the first sampled point (in 0.5 GeV steps) where the Yukawa potential supports the relevant bound state.

As a benchmark we use that Belle II can resolve invariant masses with a resolution of 10 MeV [24]. With this, we see from Figure 6.3 that we can distinguish between the different n states. For a given n value, the energy difference between different l values is too small to resolve. Now, we can look at the differential cross sections for producing the different bound states. We always do this in the center-of-mass frame of the electron-positron beams.

6.2.1 Differential Cross Sections for $\alpha_D = 0.1$

For the case of $\alpha_D = 0.1$, there are only two possible bound states that could be produced at Belle II for $m_\chi \lesssim 5\,\text{GeV}$, that is the ${}^1S_0$ state and the ${}^3S_1$ state. The differential cross sections for $m_\chi = 2\,\text{GeV}$ are shown in figures 6.4 and 6.5.

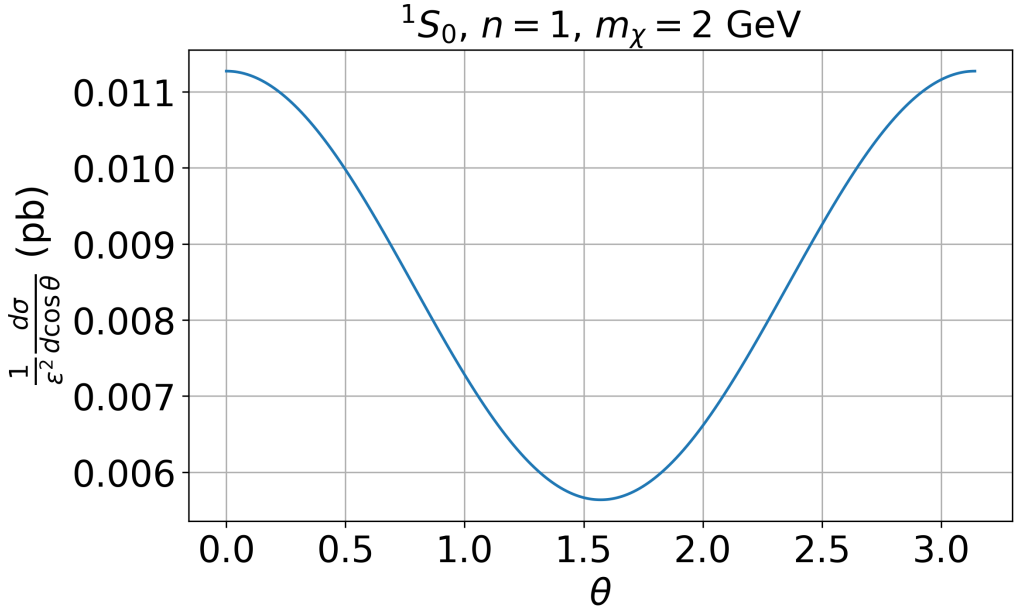

Figure 6.4: The differential cross section in units of picobarn for the process $e^+ + e^- \to^1 S_0 + V$. Here θ is the angle between the dark photon and the initial electron. The differential cross section is normalized by a factor of ϵ^2, which only constitutes an overall factor.

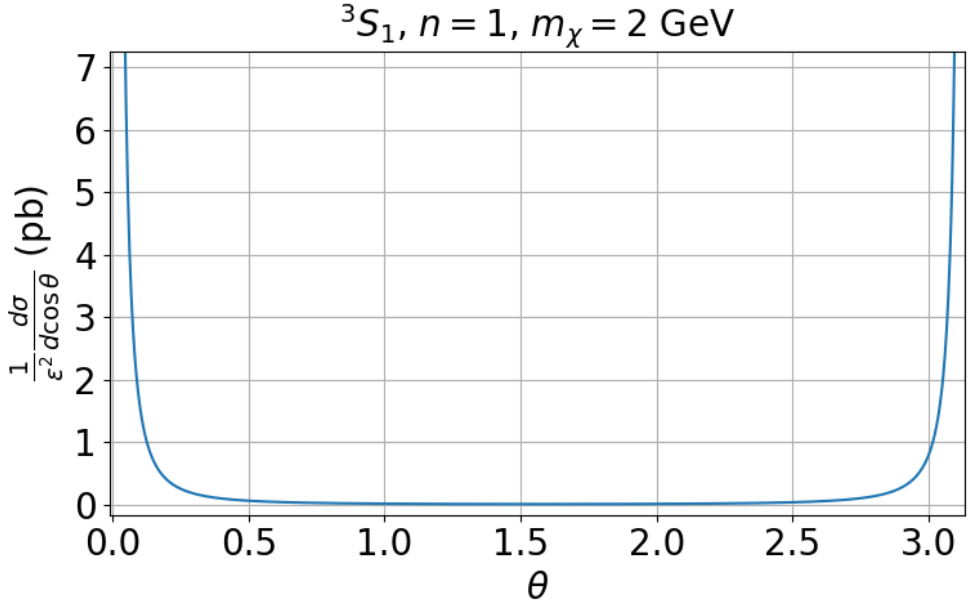

Figure 6.5: The differential cross section in units of picobarn for the process $e^+ + e^- \to^3 S_1 + \gamma$. Here θ is the angle between the photon and the initial electron. The differential cross section is again normalized by a factor of ϵ^2.

Before we interpret what these mean for detecting the bound states, it is important to note the difference in magnitude of these differential cross sections. The differential cross section for the $^3S_1$ production has a collinear divergence. We have not bothered to resolve this, because if we can measure the photon, the angle θ is not very near 0 or π anyway. It is, however, an important feature. For the $^1S_0$ production we have a cosine like shape, whereas the $^3S_1$ production shows a strong preference to produce along the beam axis. This means that in

this case we are able to distinguish between the bound states, when we reproduce the angular distributions in experiment, given we can detect the bound states. More on that later.

6.2.2 Differential Cross Sections for $\alpha_D = 0.5$

When we consider a stronger interaction, by setting $\alpha_D = 0.5$ there are many more bound states possible for masses $m_\chi \leq 5\,\text{GeV}$. Here we will consider three benchmarks for m_χ: $2\,\text{GeV}$, $3.5\,\text{GeV}$ and $5\,\text{GeV}$.

For $m_\chi = 2\,\text{GeV}$ there are three possible states $(n, l) = (1, 0), (2, 0), (2, 1)$, see figures 6.2 and 6.3. This means the following bound states, in the notation $n^{2S+1}L_J$ can be produced: 1^1S_0, 1^3S_1, 2^1S_0, 2^3S_1, $2^3P_{0,1,2}$. Here the $^1P_1$ state is absent as discussed before. The differential cross sections for these states are given in Figure 6.6.

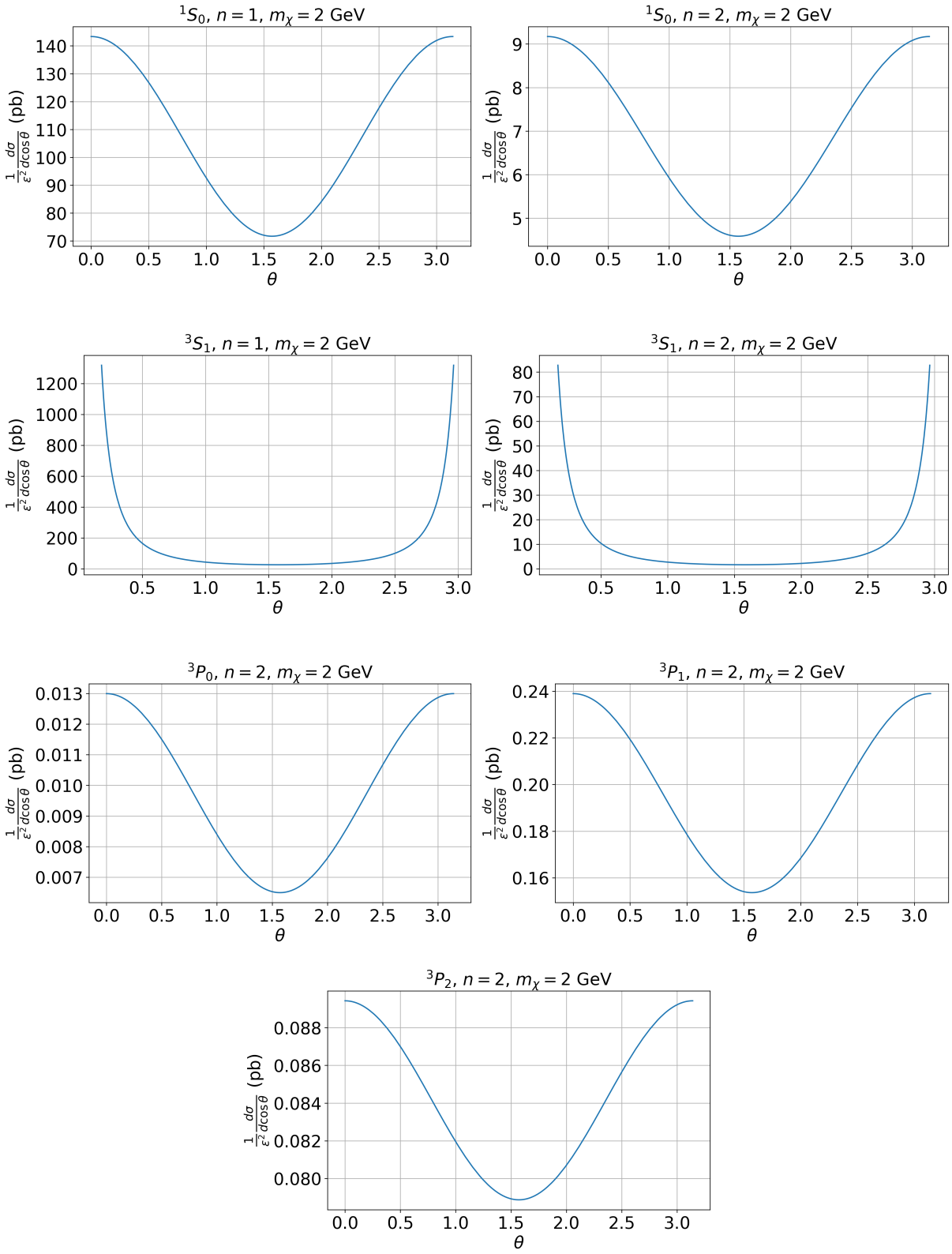

Figure 6.6: The differential cross sections for all possible bound states at Belle II for $m_\chi = 2\,\text{GeV}$, normalized by a factor of ϵ^2. The angle θ is the angle between the (dark) photon and the initial electron.

From the figure we see a clear distinction between the processes that are produced via $e^+e^- \to \chi\bar{\chi} + V$ and those that are produced via $e^+e^- \to \chi\bar{\chi} + \gamma$, the latter again having a collinear divergence. The different n states of a given bound state are indistinguishable based

on the shape of the differential cross section. The reason is that the difference between the n states in the differential cross section is in the wave function, that only gives an overall factor, and in the binding energy that is negligible compared to the mass of the $\chi\bar{\chi}$ pair. The binding energy difference between the $n = 1$ and $n = 2$ states are, however, greater than 10 MeV, see Figure 6.3. This means, we can distinguish based on the invariant mass. We cannot, however, distinguish between the ${}^1S_0$ states and the ${}^3P_J$ states based on the invariant mass or the differential cross sections.

If we increase the mass of the χ particle to $m_\chi = 3.5\,\text{GeV}$, there are nine possible bound states. Again from Figure 6.3 we see that with a resolution of $10MeV$ we can distinguish the invariant masses of the different n states. We cannot distinguish between L states this way. The differential cross sections for the possible bound states are shown in Figure 6.7.

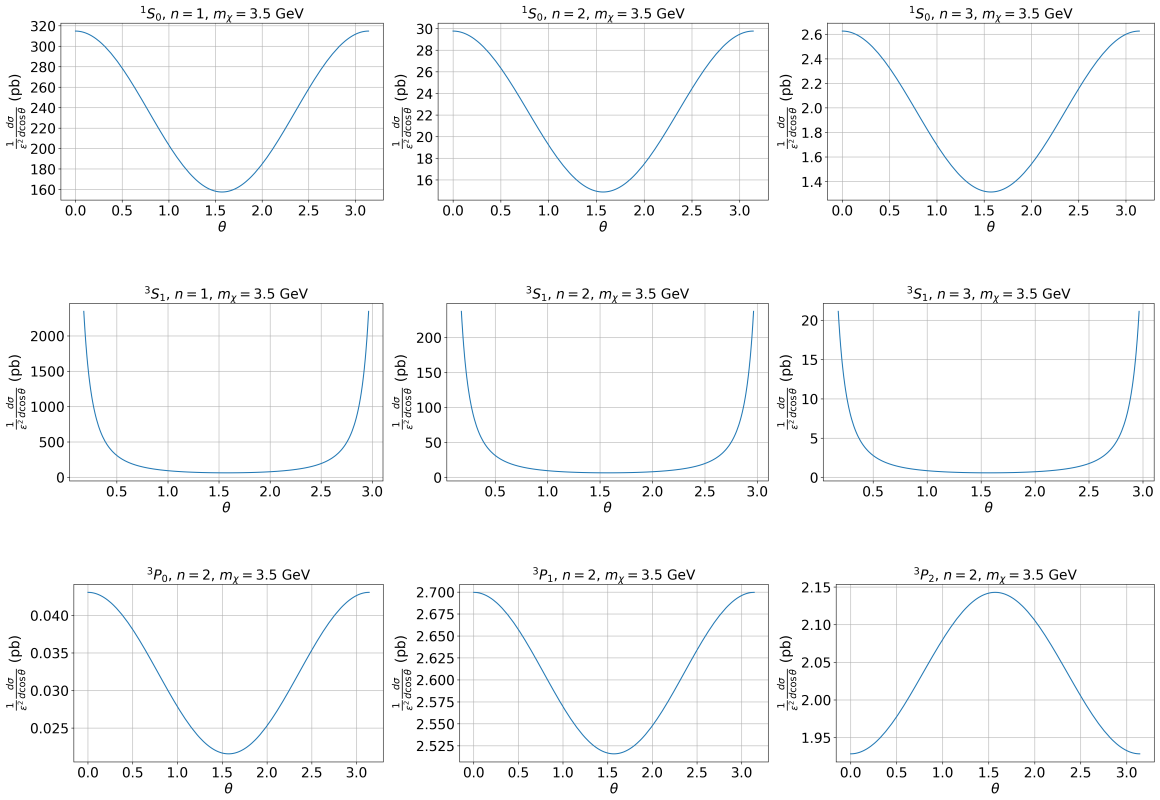

Figure 6.7: Differential cross sections of the nine possible bound states for $m_\chi = 3.5\,\text{GeV}$. θ is again the angle between the initial electron and the final state (dark) photon.

The content of this figure is almost the same as that in the case of $m_\chi = 2\,\text{GeV}$. The extra $n = 3$ states cannot be distinguish based on the differential cross sections from the lower n states, they can through their invariant mass as was mentioned before. The only difference is in the behavior of the ${}^3P_2$ state, which now peaks at $\theta = \pi/2$, i.e. normal to the beam axis. This allows us to distinguish this state from the other ${}^3P_J$ and S states, which was not the case when $m_\chi = 2GeV$.

The final mass we look at is $m_\chi = 5\,\text{GeV}$ for which there are still more bound states possible, fifteen in total. Compared to the case $m_\chi = 3.5\,\text{GeV}$ we now have D states and exited ${}^3P_J$ states. The differential cross sections for all these states are shown in Figure 6.8.

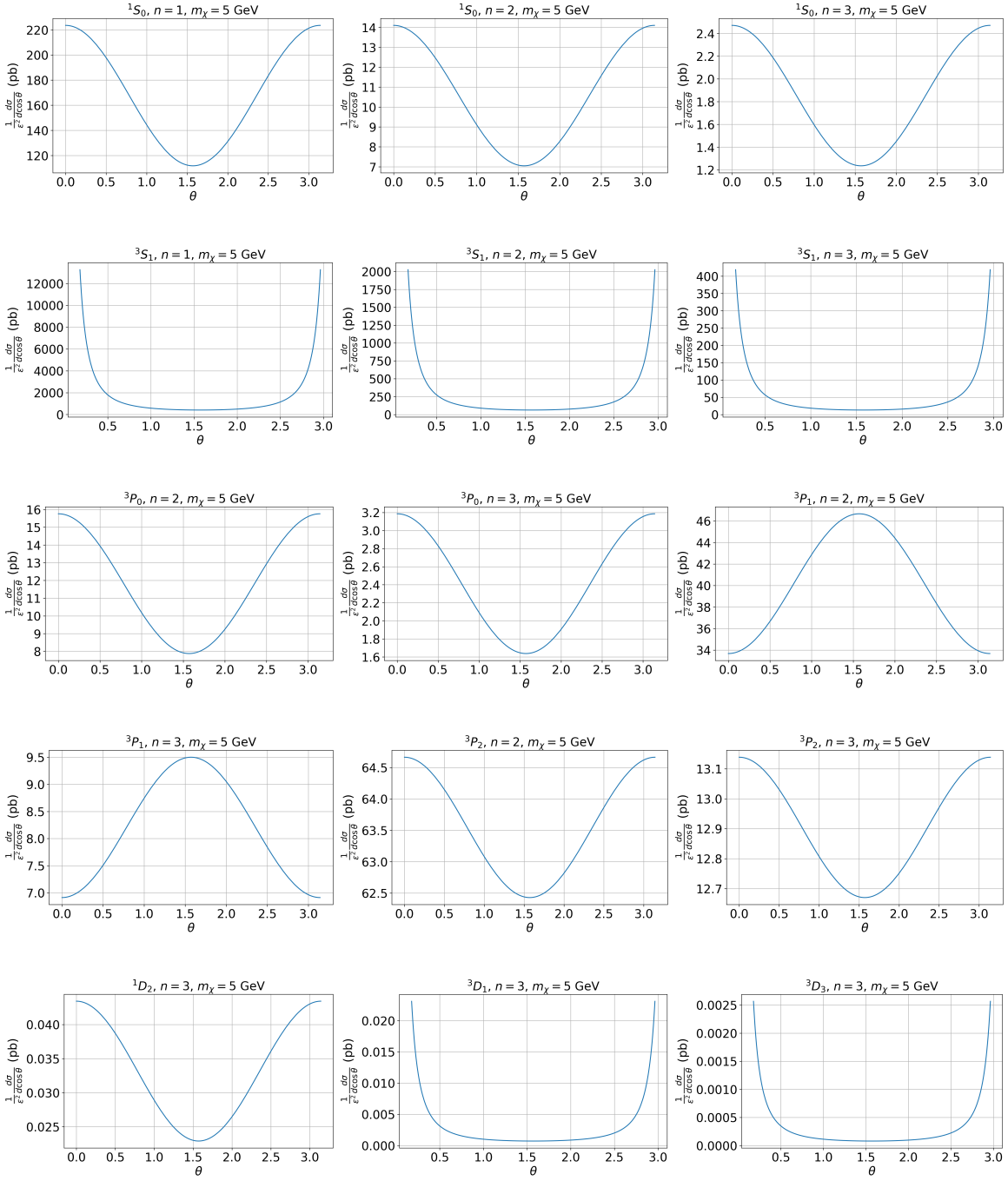

Figure 6.8: Differential cross sections of the fifteen possible bound states for $m_\chi = 5\,\text{GeV}$. θ is again the angle between the initial electron and the final state (dark) photon.

Just as before, the same distinction between the bound states based on their production process is possible, now with the $^1D_2$ state being indistinguishable from those that are produced via $e^+e^- \to \chi\bar{\chi} + V$ and the ^3D_J states being indistinguishable from those that are produced via $e^+e^- \to \chi\bar{\chi} + \gamma$. The $^3D_2$ states are not present, as discussed before. For $m_\chi = 5\,\text{GeV}$ the $^3P_1$ states behave differently from the other ^3P_J states, just as was the case for the $^3P_2$ states for $m_\chi = 2\,\text{GeV}$.

6.3 Detector Signatures

Now that we know that we can distinguish between certain states based on their invariant mass and their differential cross section, it is important to note that these depend on our ability to detect the bound state decay products. In the case of the process $e^+e^- \to \chi\bar{\chi} + \gamma$ we could, of course, detect the photon and, if the bound state decay products are sufficiently long-lived, use missing energy and momentum to reconstruct the rest. In the case where there are only particles of the dark sector, i.e. χ, $\bar{\chi}$ and V, we cannot extract all this information. Therefore, we will focus on detecting the bound state itself, or its decay products.

The first question we must then ask is whether the bound state decays within the detector or escapes. Earlier we discussed the possible decay channels of the different bound states, either to two or three dark photons to lowest order. In the case of the two dark photon decays we can do this calculation explicitly as we did in the previous section.

6.3.1 Detector Signatures for $\alpha_D = 0.1$

We start again by considering $\alpha_D = 0.1$, for which we only have the two $n = 1$, $L = 0$ states ${}^1S_0$ and ${}^3S_1$. The decay length of the ${}^1S_0$ state, as a function of m_χ in the center-of-mass frame of the electron-positron beams can be calculated using

$$L = \frac{p_{BS}^{CM}}{m_{BS}} \frac{1}{\Gamma}, \tag{6.1}$$

where the subscript BS indicates the bound state, and the superscript CM indicates that we consider the momentum in the center-of-mass frame. The decay width is given in the previous section. The result is given in Figure 6.9.

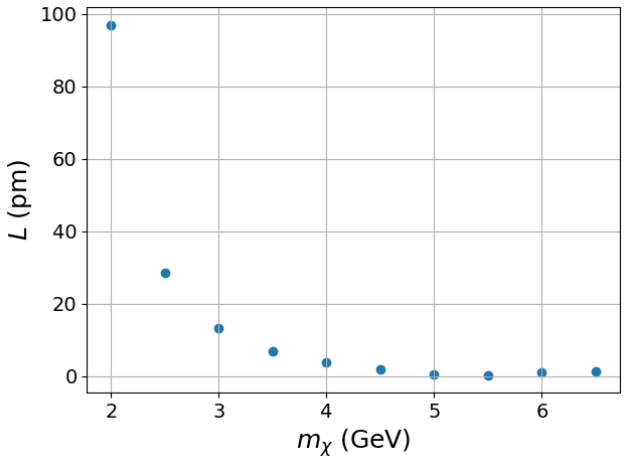

Figure 6.9: The decay length of the ${}^1S_0$ state produced via e^+e^- collisions as a function of m_χ for $\alpha_D = 0.1$. The decay length is of the order of picometers.

Belle II is able to resolve distances of the order of tens of micrometers[25]. Hence, the decay of the ${}^1S_0$ is prompt. Now the question becomes whether we can detect the bound state decay products. As discussed before, it is important to note that the $C = -1$ states decay to three dark photons and that such a decay is not easily calculated. Here we will assume the ${}^3S_1$ state also decays promptly.

Now we are interested in the decay products of the bound states in the center-of-mass frame. The decay products are dark photons. The dark photons are also unstable and decay to electron-positron pairs. For our benchmark value of $m_V = 100\,\text{MeV}$, this is the only possible decay. Other decay products are too heavy. The lightest alternative for decay to standard model particles is to a $\mu^+\mu^-$ pair or a pair of pions, both of which require an invariant mass of the dark photon that is larger than the benchmark of 100 MeV. Decay to dark matter particles, i.e. a $\chi\bar{\chi}$ pair is also not possible, because we consider the region of parameter space where bound states can form, which requires $m_\chi > m_V$. So the final question to be answered here is if we can detect the decay of the dark photon. We start in the rest frame of the dark photon and consider its decay to an electron-positron pair, the Feynman diagram of which is shown in Figure 6.10.

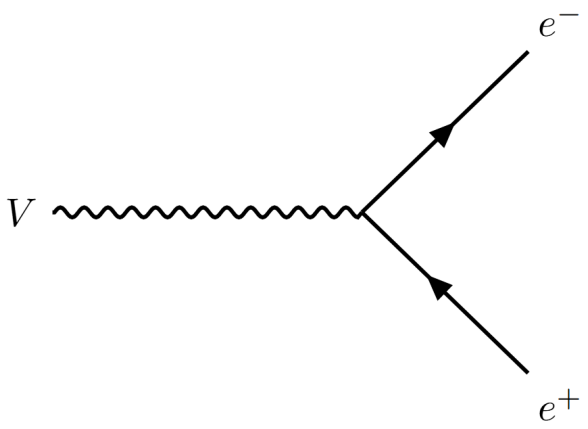

Figure 6.10: The lowest order contributing diagram to the decay of a dark photon to an electron-positron pair.

The decay width is easily calculated and is given by

$$\Gamma = \frac{\alpha\epsilon^2\sqrt{m_V^2 - 4m_e^2}(2m_e^2 + m_V^2)}{3m_V^2}, \tag{6.2}$$

where α is the fine structure constant. To examine the decay length of the dark photons we need to use Equation 6.2 together with Equation 6.1, where in the latter equation we, of course, use the dark photon mass and momentum. The hardest part here is to find the dark photon momentum in the CM frame. We examined the decay of the bound state in its rest frame. In the case of a decay to two dark photons the kinematics are fixed and we know exactly the dark photon four momentum. In the case that the bound state decays to three dark photons, we assume that the energy of the bound state is divided equally among the dark photons. The kinematics and the transformation to the CM frame are discussed in Appendix E. The resulting decay lengths as a function of m_χ, for the dark photons coming from the ${}^1S_0$ decay and those coming from the ${}^3S_1$ decay, are given in Figure 6.11.

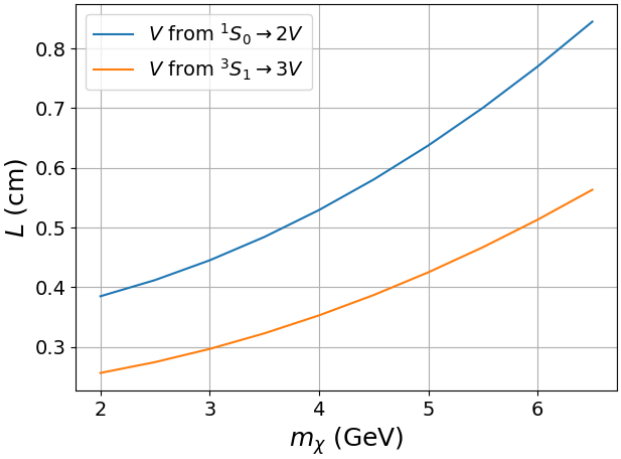

Figure 6.11: The decay lengths of the dark photons in the e^+e^- CM frame as a function of m_χ. Here the value $\epsilon = 10^{-4}$ is chosen.

From the figure we see that the decay length is on the order of tens of millimeters for all possible masses m_χ for which bound states can form at Belle II. Such values correspond to displaced vertices. We can look closer at the decay probability P using an exponential

$$P(x) = \frac{1}{L} e^{-x/L}, \tag{6.3}$$

where x is the distance traveled. This decay probability is shown in Figure 6.12 for a few values of m_χ.

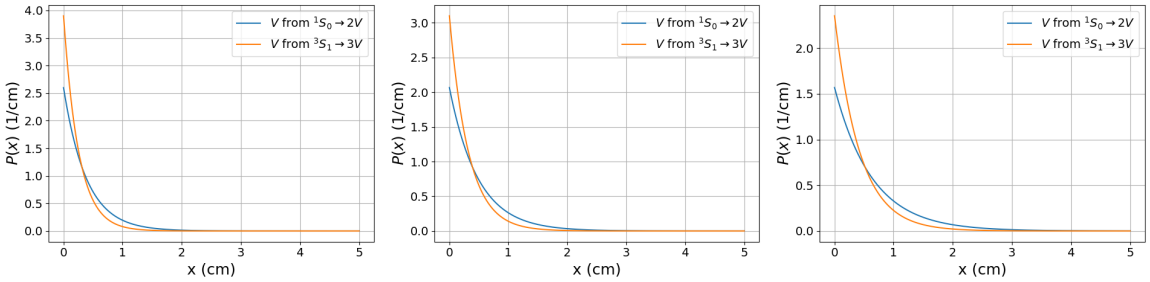

(a) $m_\chi = 2\,\text{GeV}$ (b) $m_\chi = 3.5\,\text{GeV}$ (c) $m_\chi = 5\,\text{GeV}$

Figure 6.12: The decay probability of the dark photons coming from bound state decays as a function of distance traveled.

From these figures we see that many dark photons decay near $x = 0$, but there is also a significant region away from $x = 0$ up to distances of $x = 1$-$2cm$. This means that dark matter bound states would have a clear signature at Belle II for our benchmarks. That is, two or three electron-positron pairs coming from displaced vertices.

One may generalize this to arbitrary ϵ. The decay width scales with $\frac{1}{\epsilon^2}$, and therefore the decay length does too. For arbitrary choices of ϵ the decay probability density then becomes

$$P(x, \epsilon) = \frac{\epsilon^2}{\tilde{L}} e^{-\epsilon^2 x/\tilde{L}}, \tag{6.4}$$

where $\tilde{L} = \epsilon^2 L$. So for smaller ϵ the distribution becomes flatter.

6.3.2 Detector Signatures for $\alpha_D = 0.5$

Now we will examine the detector signatures if the interaction is stronger, i.e. $\alpha_D = 0.5$. As mentioned before, there are now more bound states, and the possible bound states depend on the mass m_χ. We can repeat the analysis we did when $\alpha_D = 0.1$. We start again by looking at the decay lengths of the different bound states as a function m_χ. Again, we only do this for the states that decay to two dark photons. The decay length of these bound states are plotted in Figure 6.13.

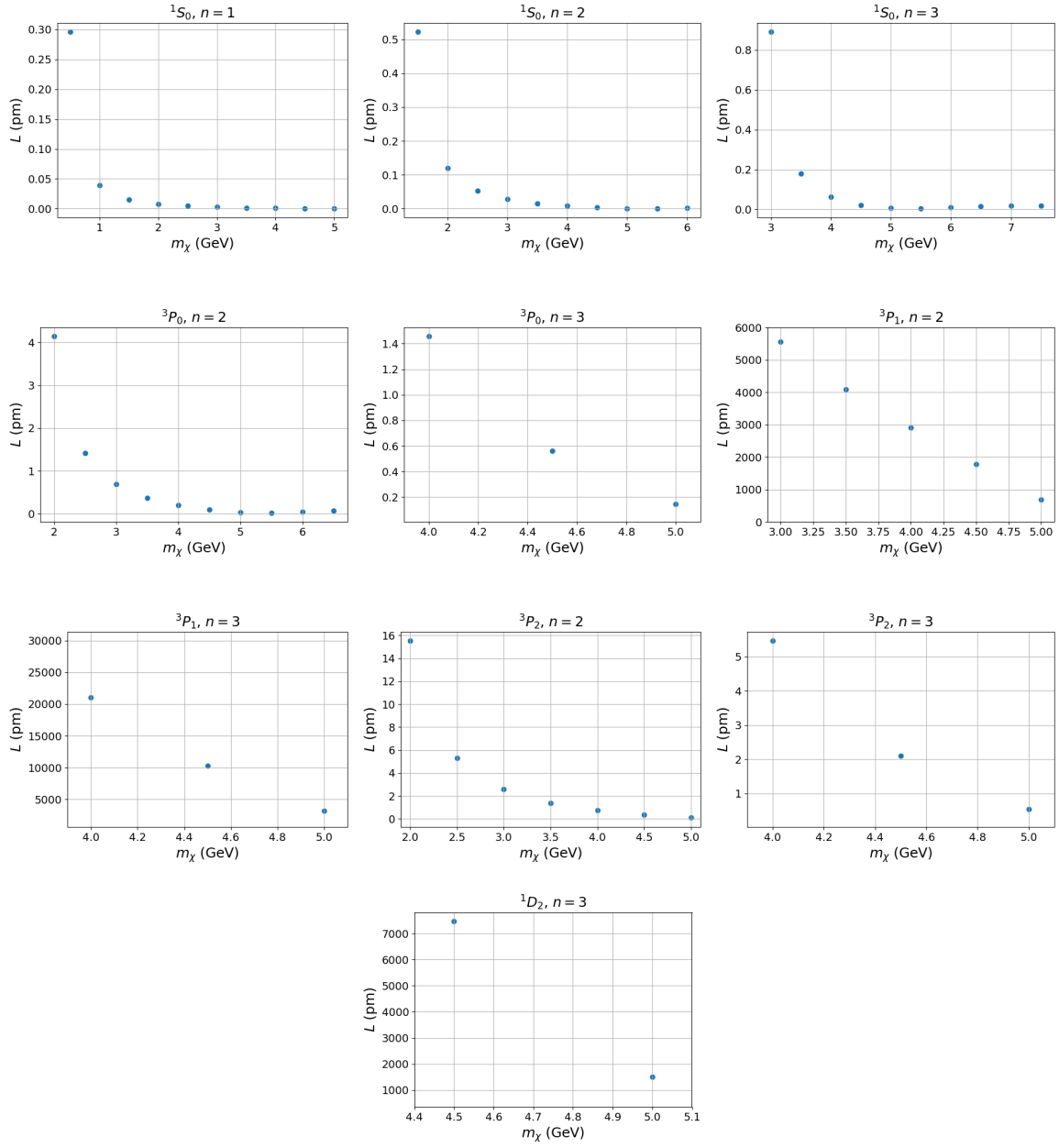

Figure 6.13: The decay lengths of the different bound states that could be formed at Belle II for $\alpha_D = 0.5$ as function of the mass m_χ. Only the values of m_χ for which each bound state can form is shown.

From the figure it is clear that the largest decay length is on the order of a few nanometer. Most have decay lengths on the order of picometers. Again, this corresponds to prompt decay. We assume that the bound states that decay to three dark photons also decay within the

detector. Now we will shift our focus to the decay products of the bound states. The decay lengths of the dark photons coming from the bound state decay are shown in Figure 6.14.

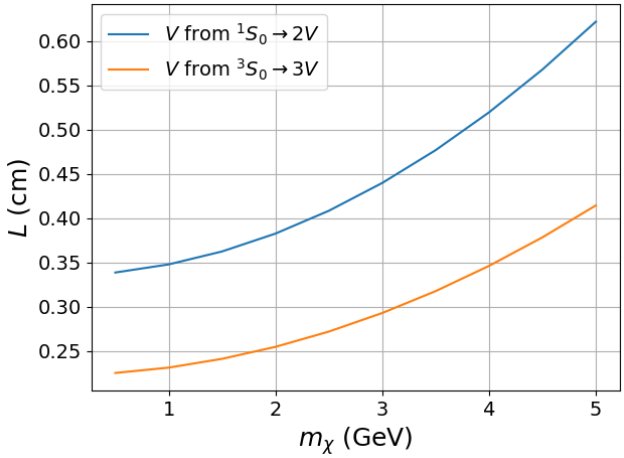

Figure 6.14: The decay length of the dark photons coming from the bound state decay for $\alpha_D = 0.5$.

Here, only the decay lengths of the dark photons coming from the $^1S_0$ and the $^3S_1$ decay are shown, with the same approximation for the three dark photon decays as before. The reason for only looking at these two decays is that the difference with the other states is minimal. This is clear from Equation 6.1. The decay lengths of the dark photons coming from the decay of different states only differ in their momentum in the center-of-mass frame. The momentum depends on the number of dark photons a bound state decays to, and on the bound state mass. The former introduces the difference between the decay lengths for the dark photons coming from the $BS \to 2V$ and $BS \to 3V$ decays. The mass difference between bound states comes from the different binding energies. As these are negligible compared to m_χ, P_V^{CM} and m_{BS} are approximately the same for all states with the same decay channel. From the figure we notice again that the decay length is on the order of tens of millimeters. Distances that are resolvable at Belle II. For three values of m_χ the decay probability density of the dark photons as a function of distance traveled is shown in Figure 6.15.

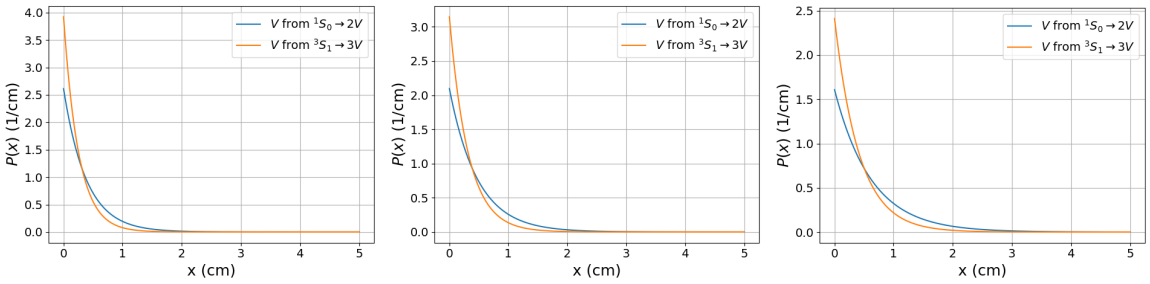

(a) $m_\chi = 2GeV$ (b) $m_\chi = 3.5GeV$ (c) $m_\chi = 5GeV$

Figure 6.15: The decay probability density of the dark photons coming from bound state decays as a function of distance traveled.

These results are almost identical to those we found for $\alpha_D = 0.1$. This makes sense as there is no α_D dependence in equations 6.1 and 6.2. The only differences are that in the case of $\alpha_D = 0.5$ bound states can form at lower masses m_χ and there are more bound states. The binding energies for the bound states differ for the different values of α_D, but they are still

negligible compared to m_χ. So also in the case $\alpha_D = 0.5$, and any other α_D for that matter, we would see electron-positron pairs coming from displaced vertices. Under the condition that α_D is such that the Yukawa potential supports bound states.

6.4 Summary of Distinguishable States and ϵ Requirement for Detection

We end our analysis of dark matter bound states at Belle II with a summary of which states can form and which can be distinguished for our benchmark parameters and discussing for what values of ϵ bound states can be observed at Belle II.

For $\alpha_D = 0.1$, there were only two bound states, 1^1S_0 and 1^3S_1 which were distinguishable based on their differential cross sections, no matter m_χ. Of course, m_χ should be such that bound states can exist and can be produced at Belle II.

For $\alpha_D = 0.5$ the (in)distinguishability is shown in Table 5. For our three benchmark values of m_χ the bound states that can be produced are shown. They are grouped by square brackets. States within the same bracket can not be distinguished based on invariant mass, when we have a resolution of 10 MeV. Within each bracket, curly brackets indicate indistinguishability based on the differential cross section.

m_χ [GeV]	**Grouped Bound States**
2.0	$\big[\{1^1S_0\},\ \{1^3S_1\}\big]$ $\big[\{2^1S_0,\ 2^3P_0,\ 2^3P_1,\ 2^3P_2\},\ \{2^3S_1\}\big]$
3.5	$\big[\{1^1S_0\},\ \{1^3S_1\}\big]$ $\big[\{3^1S_0\},\ \{3^3S_1\}\big]$ $\big[\{2^1S_0,\ 2^3P_0,\ 2^3P_1\},\ \{2^3S_1\},\ \{2^3P_2\}\big]$
5.0	$\big[\{1^1S_0\},\ \{1^3S_1\}\big]$ $\big[\{2^1S_0,\ 2^3P_0,\ 2^3P_2\},\ \{2^3S_1\},\ \{2^3P_1\}\big]$ $\big[\{3^1S_0,\ 3^3P_0,\ 3^3P_2,\ 3^1D_2\},\ \{3^3S_1,\ 3^3D_3,\ 3^3D_1\},\ \{3^3P_1\}\big]$

Table 5: Groupings of bound states for different dark matter masses m_χ. Square brackets group states indistinguishable in invariant mass; curly braces indicate further indistinguishability in angular or differential distributions.

To get an idea as to what values of ϵ result in visible dark matter bound states we will require 10 events as a benchmark. Our calculated cross sections are of the form $\epsilon^2\sigma_{\text{tot}}$, so we require

$$10 = \epsilon^2\sigma_{\text{tot}}\mathcal{L}_{\text{int}}, \tag{6.5}$$

where $\mathcal{L}_{\text{int}}$ is the integrated luminosity. So this equation is just the number of events calculated as the product of the integrated luminosity and the total cross section of the process of interest.

Our requirement for ϵ then becomes

$$\epsilon \geq \sqrt{\frac{10}{\sigma_{\text{tot}}\mathcal{L}_{\text{int}}}}. \tag{6.6}$$

The aim of Belle II is to reach an integrated luminosity of $\mathcal{L}_{\text{int}} = 50\ \text{ab}^{-1}$[22]. To get the total cross sections for the production of the different bound states we integrate the differential cross sections over the angle θ. For the differential cross sections with a collinear divergence we make an approximation by excluding parts at both ends of the interval and integrate over $\theta \in [\frac{10\pi}{180}, \frac{170\pi}{180}]$, which corresponds to excluding 10 degrees at both ends.

For $\alpha_D = 0.1$ the total cross sections and minimal ϵ to expect 10 events are given in Table 6.

State	$m_\chi = 2\,\text{GeV}$	$m_\chi = 3.5\,\text{GeV}$	$m_\chi = 5\,\text{GeV}$
1^1S_0	$\sigma = 0.0266,\ \epsilon \geq 2.7 \times 10^{-3}$	$\sigma = 0.158,\ \epsilon \geq 1.1 \times 10^{-3}$	$\sigma = 0.0718,\ \epsilon \geq 1.7 \times 10^{-3}$
1^3S_1	$\sigma = 0.166,\ \epsilon \geq 1.1 \times 10^{-3}$	$\sigma = 0.927,\ \epsilon \geq 4.6 \times 10^{-4}$	$\sigma = 9.11,\ \epsilon \geq 1.48 \times 10^{-4}$

Table 6: Total production cross sections (σ) and corresponding lower bounds on the kinetic mixing parameter (ϵ) for different bound states and dark matter masses m_χ. All cross sections are given in picobarn.

All of these values of ϵ fall within a region not excluded in Figure 2.1 for $m_V = 100\,\text{MeV}$. Values between $\epsilon \sim 10^{-3}$ and $\epsilon \sim 10^{-3.5} = 3.16 \cdot 10^{-4}$ fall within reach of what Belle II can observe, see the region in Figure 2.1 denoted Belle II. This indicates that the states 1^1S_0 and 1^3S_1 could be observed at Belle II for our benchmark values with the signatures as discussed before.

For $\alpha_D = 0.5$ we can do the same. The total cross sections and the minimum ϵ for 10 events are given in Table 7.

State	$m_\chi = 2$ **GeV**	$m_\chi = 3.5$ **GeV**	$m_\chi = 5$ **GeV**
1^1S_0	$(338,\ 2.43 \times 10^{-5})$	$(742,\ 1.64 \times 10^{-5})$	$(527,\ 1.95 \times 10^{-5})$
1^3S_1	$(429,\ 2.16 \times 10^{-5})$	$(804,\ 1.58 \times 10^{-5})$	$(4680,\ 6.54 \times 10^{-6})$
2^1S_0	$(21.6,\ 9.62 \times 10^{-5})$	$(70.1,\ 5.34 \times 10^{-5})$	$(33.2,\ 7.76 \times 10^{-5})$
2^3S_1	$(27.0,\ 8.61 \times 10^{-5})$	$(81.5,\ 4.95 \times 10^{-5})$	$(715,\ 1.67 \times 10^{-5})$
2^3P_0	$(0.0306,\ 2.56 \times 10^{-3})$	$(0.102,\ 1.40 \times 10^{-3})$	$(37.1,\ 7.34 \times 10^{-5})$
2^3P_1	$(0.617,\ 5.69 \times 10^{-4})$	$(8.19,\ 1.56 \times 10^{-4})$	$(126,\ 3.98 \times 10^{-5})$
2^3P_2	$(0.264,\ 8.70 \times 10^{-4})$	$(6.40,\ 1.77 \times 10^{-4})$	$(200,\ 3.17 \times 10^{-5})$
3^1S_0	–	$(6.19,\ 1.80 \times 10^{-4})$	$(5.82,\ 1.85 \times 10^{-4})$
3^3S_1	–	$(7.26,\ 1.66 \times 10^{-4})$	$(148,\ 3.68 \times 10^{-5})$
3^3P_0	–	–	$(7.58,\ 1.62 \times 10^{-4})$
3^3P_1	–	–	$(25.8,\ 8.81 \times 10^{-5})$
3^3P_2	–	–	$(40.5,\ 7.02 \times 10^{-5})$
3^1D_2	–	–	$(0.104,\ 1.39 \times 10^{-3})$
3^3D_1	–	–	$(0.00816,\ 4.95 \times 10^{-3})$
3^3D_3	–	–	$(0.000907,\ 1.49 \times 10^{-2})$

Table 7: Total production cross sections (in pb) and corresponding lower bounds on ϵ for each bound state, at different dark matter masses m_χ.

From this we observe that our benchmark value of $\epsilon = 10^{-4}$, in combination with $\alpha_D = 0.5$ and $m_V = 100\,\text{MeV}$, is sufficient to make many of these bound states observable at Belle II. However, it is important to note that $\alpha_D = 0.5$ is quite large and approaches the non-perturbative regime. This benchmark should therefore be interpreted more as an illustrative case for exploring the behavior of dark matter bound states than as a precise prediction for experimental outcomes.

7 Dark Matter Bound States at FCC-ee

After examining dark matter bound state production at Belle II, we now turn our attention to the FCC-ee experiment.

The Future Circular Collider (FCC) is a next-generation collider project proposed at CERN, envisioned to surpass all existing colliders in size and precision. It will consist of an underground circular tunnel with a circumference of 90.7 km, spanning the Franco–Swiss border. A feasibility report for the project was published in March 2025 [26, 27, 28]. The FCC will initially host an electron–positron collider (FCC-ee), designed to operate at center-of-mass energies between 90 GeV and 350 GeV. This phase is expected to begin in the late 2040s and run for approximately 15 years. In the longer term, the same infrastructure will be repurposed for the FCC-hh, a proton–proton and heavy-ion collider targeting collision energies of up to 100 TeV [29].

The FCC will not only provide deeper insights into the Standard Model but will also be sensitive to weakly coupled dark sectors and other candidates for physics beyond the Standard Model. Examples include heavy axions, dark photons, and long-lived particles [30]. This makes it the ideal environment to study our dark matter bound states.

7.1 Producing Bound States at FCC-ee

When considering bound state production at FCC-ee, we have much more energy than at Belle II. Consequently, the $Z-V$-mixing term, introduced in the Lagrangian of Equation 2.3, should be taken into account. This means that for the process $e^+e^- \to \chi\bar{\chi}V$, in addition to the diagrams shown in Figure 5.1, we must also include those where the intermediate propagator is a Z boson instead of a V. Similarly, for the process $e^+e^- \to \chi\bar{\chi}\gamma$, as shown in Figure 5.2, we should also account for diagrams where the propagator is a Z boson. Additionally, if the center-of-mass energy is sufficient, bound states that are produced via the latter process may also be produced via $e^+e^- \to \chi\bar{\chi}Z$. For the former process, replacing the external V with a Z boson would lead to an amplitude that is suppressed with an additional factor of ϵ. As we are interested in working in the non-relativistic limit, we will consider bound states with masses sufficiently close to the center-of-mass energy, such that the possibility of producing an on-shell Z boson is excluded.

As mentioned before, the FCC-ee experiment will operate at different center-of-mass energies. We will consider two runs. The first will be at the Z pole, i.e. $\sqrt{s} = 91.2$ GeV. The targeted integrated luminosity for this run is 125 ab^{-1}. The second run we consider is that at the center-of-mass energy $\sqrt{s} = 240$ GeV, where the expected integrated luminosity is 10.8 ab^{-1} [26]. These integrated luminosities will help us identify the range for ϵ for which dark matter bound state production processes are observable.

7.1.1 Z Pole Run

For the Z pole run at $\sqrt{s} = 91.2$ GeV we take a benchmark value $m_\chi = 35$ GeV to investigate the dark matter bound state production. We also set $\alpha_D = 0.1$. Together with $m_V = 100$ MeV we obtain $\delta = 0.0571$, which from Table 2 implies we can produce bound states up to $n = 4$, $L = 2$. However, we will keep our discussion to states up to $n = 3$.

When the center-of-mass energy is set to the Z mass, it will be the diagrams with the Z propagator that dominate over those with a V propagator. Because the experiment is tuned to

the Z mass, the propagator will feature a divergence for $\sqrt{s} = m_Z$. We remedy this by taking into account the finite life time of the Z boson via the Breit-Wigner formula [13]

$$\frac{1}{s - m_Z^2} \to \frac{1}{s - m_Z^2 + i m_Z \Gamma_Z}, \tag{7.1}$$

where Γ_Z is the decay width of the Z boson. The differential cross sections for the possible bound states for our benchmark values are shown in Figure 7.1.

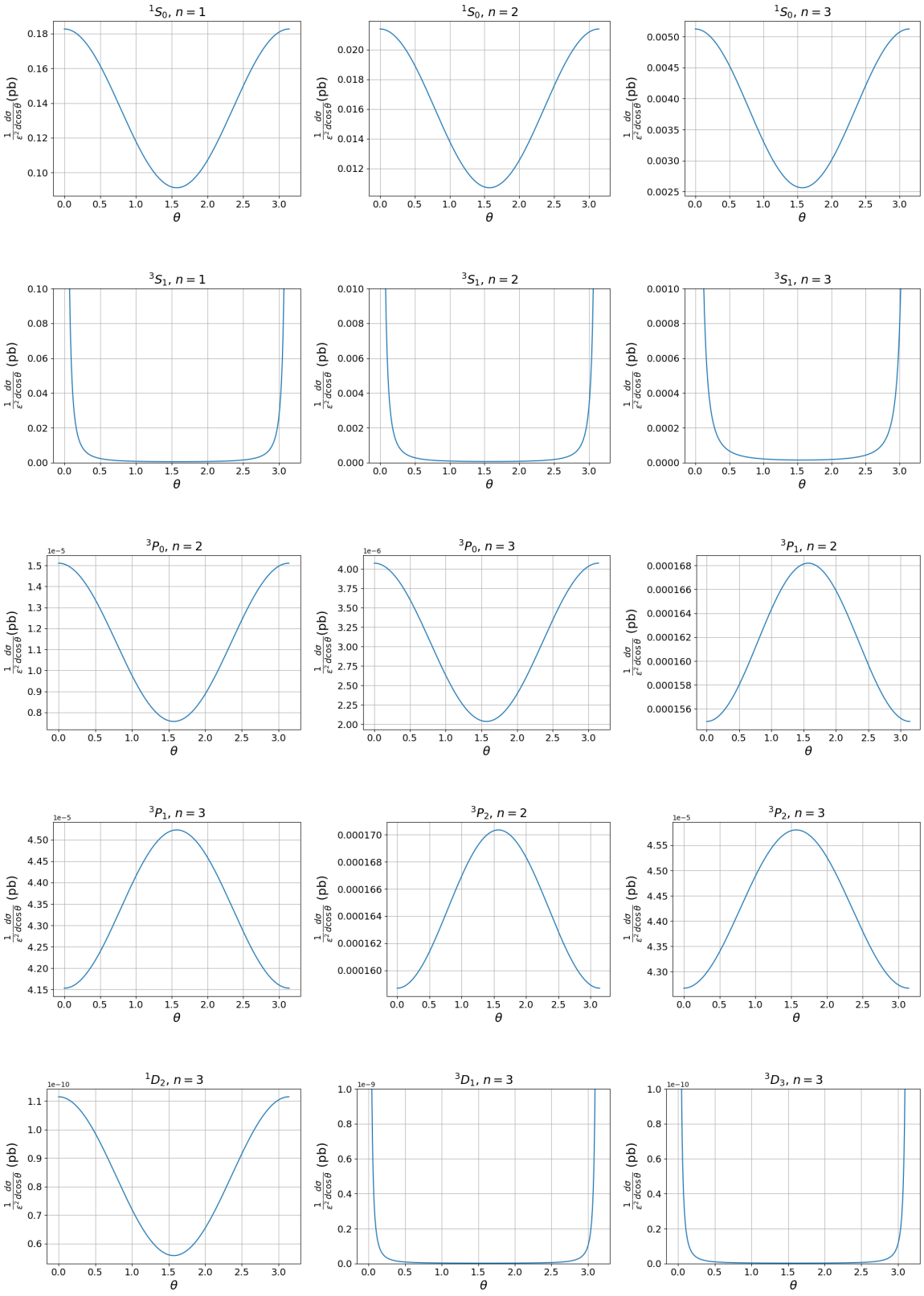

Figure 7.1: Differential cross sections for the possible bound states at FCC for $m_\chi = 35$ GeV, $\alpha_D = 0.1$, $m_V = 100$ MeV and $\sqrt{s} = 91.2$ GeV. The angle θ is the angle between the initial electron and the final (dark) photon. The differential cross sections are normalized by a factor ϵ^2.

As we are dealing with a collinear divergence for the processes that involve a photon, the

cutoff on the vertical axis is arbitrary and chosen such that the shape of the differential cross section is easily visible. This does not influence the rest of our discussion, as our predictions are not valid there anyway, because we have not resummed the divergent contributions. From the differential cross sections we can group the different states again in indistinguishable classes. We have n^1S_0 for $n = 1, 2, 3$ and the n^3P_0 for $n = 2, 3$ states as one group. Then the n^3P_J for $n = 2, 3$ and $J = 1, 2$ as the second group and lastly the n^3S_1 states for $n = 1, 2, 3$ and the ${}^3D_J$ states for $J = 1, 2$ as the last group. It is difficult to determine the precision of invariant mass measurements for a general process, as this is very much process dependent. It could be estimated from the expectations for other processes. FCC-ee is expected to have extraordinary precision for measurements of, for example, the Z mass[26]. Here we will make a conservative estimate of 100 MeV precision. The energy levels of the different states of the $\chi\bar{\chi}$ bound state for the parameters $m_\chi = 35$ GeV, $\alpha_D = 0.1$ and $m_V = 100$ MeV are shown in Figure 7.2.

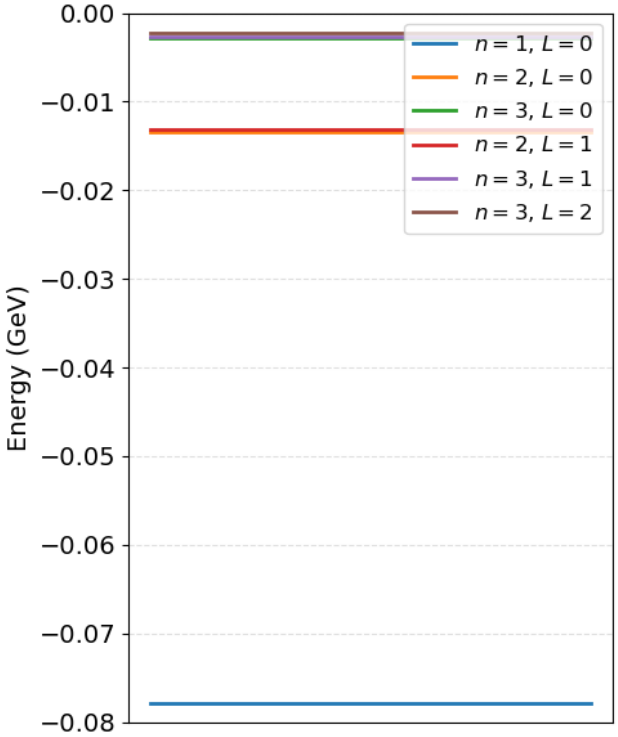

Figure 7.2: Energy levels of the different energy states of the bound state $\chi\bar{\chi}$ for the parameters $m_\chi = 35$ GeV, $\alpha_D = 0.1$ and $m_V = 100$ MeV.

Using our benchmark of 100 MeV precision, we could only distinguish between the different n states. The different L states within each n are indistinguishable on the basis of their mass.

Now that we know which states we can distinguish we will look at the values of ϵ needed to observe each bound state. We calculate the total bound state by integrating over the angle θ, where for the states with a collinear divergence we take out 10 degrees on each side of the interval. We use Equation 6.6 to determine the required values of ϵ to observe 10 events. We use here the goal of the FCC-ee experiment to reach an integrated luminosity of 125 ab^{-1} The total cross section for each state and the required ϵ to observe it is given in Table 8.

State $n^{2S+1}L_J$	σ_{tot} (pb)	$\epsilon \geq$	State $n^{2S+1}L_J$	σ_{tot} (pb)	$\epsilon \geq$
1^1S_0	0.430261	$4.31 \cdot 10^{-4}$	2^3P_1	$5.08 \cdot 10^{-4}$	$1.25 \cdot 10^{-2}$
2^1S_0	0.0504038	$1.26 \cdot 10^{-3}$	3^3P_1	$1.36 \cdot 10^{-4}$	$7.67 \cdot 10^{-3}$
3^1S_0	0.0120741	$2.57 \cdot 10^{-3}$	2^3P_2	$5.17 \cdot 10^{-4}$	$1.24 \cdot 10^{-2}$
1^3S_1	$6.883 \cdot 10^{-3}$	$3.41 \cdot 10^{-3}$	3^3P_2	$1.39 \cdot 10^{-4}$	$2.40 \cdot 10^{-2}$
2^3S_1	$7.241 \cdot 10^{-3}$	$3.32 \cdot 10^{-3}$	3^1D_2	$2.63 \cdot 10^{-10}$	17.4
3^3S_1	$1.739 \cdot 10^{-3}$	$6.78 \cdot 10^{-3}$	3^3D_1	$2.26 \cdot 10^{-11}$	59.5
2^3P_0	$3.56 \cdot 10^{-5}$	$4.74 \cdot 10^{-2}$	3^3D_3	$2.51 \cdot 10^{-12}$	178.5
3^3P_0	$9.60 \cdot 10^{-6}$	$9.13 \cdot 10^{-3}$			

Table 8: The minimum value for ϵ to expect 10 events of bound state production.

From this we see that for the 1^1S_0 state, the required value of ϵ for detection is of the same order of magnitude as the not excluded value $\epsilon = 10^{-4}$ we used as a benchmark. For the other S-wave and some P-wave states, the value of ϵ is somewhat larger, but still in a non-excluded region of Figure 2.1. For other states, it is one or more orders of magnitudes larger, which is in an excluded region in the (m_V, ϵ) space, see Figure 2.1. We should note, though, that these bounds are model specific. The additional complexity of dark matter particles and bound state formation could alter the bounds. Although larger integrated luminosities could in principle lower the required value of ϵ to achieve observability, the current benchmarks remain out of reach. Of course, it is possible to explore alternative benchmark values for α_D, m_χ and m_V that might yield observable signatures. However, in a given physical model, these parameters are fixed by nature. In this work, we examine a representative benchmark scenario for the FCC-ee run, not with the aim of optimizing observability, but to illustrate the potential experimental signatures to a realistic and presently allowed point in parameter space.

7.1.2 240 GeV Run

Now we turn our attention to the 240 GeV run planned for FCC-ee. This allows us to look at even heavier dark matter bound states. In this section we will consider $m_\chi = 100$ GeV and leave the other parameters unaltered, i.e. $\alpha_D = 0.1$ and $m_V = 100$ MeV. With these choices we have $\delta = 0.02$, which means we can produce bound states up to $n = 7$. Again, we will limit ourself to the discussion of the states up to $n = 3$. The differential cross sections for the production of the bound states up to $n = 3$ is given in Figure 7.3. Here we have taken into account both the V and Z propagator. We have not used the Breit-Wigner formula as we are far away from the Z pole.

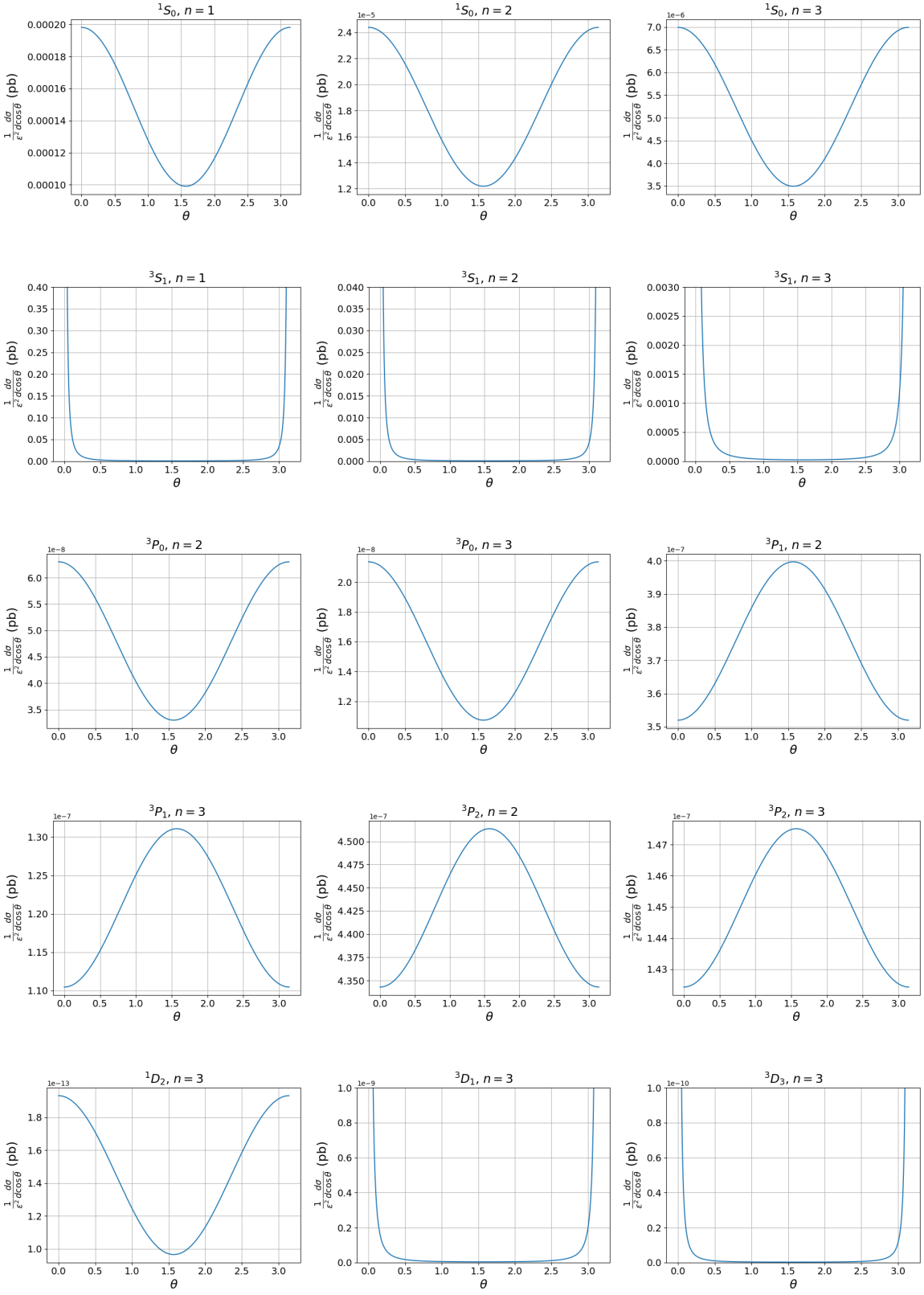

Figure 7.3: Differential cross sections for the production of dark matter bound states at FCC-ee for the $\sqrt{s} = 240$ GeV run. The angle θ is the angle between the initial electron and the final state (dark) photon.

From this figure we see that the differential cross sections exhibit the same behavior as for the Z pole run, allowing for the same distinction between those bound states produced via

$e^+e^- \to n^{2S+1}L_J + V$ and $e^+e^- \to n^{2S+1}L_J + \gamma$. Where within the group of bound states produced via the former process we can distinguish the n^3P_J states for $n = 2, 3$ and $J = 1, 2$ from the rest. Here we do not consider the process $e^+e^- \to n^{2S+1}L_J + Z$, as there is not enough center-of-mass energy to produce the Z on shell when we consider $m_\chi = 100$ GeV. For lighter dark matter bound states such a process could contribute. We choose to consider a benchmark value of m_χ such that the bound state mass is close to the center-of-mass energy, ensuring a non-relativistic bound state. To see whether we can distinguish states based on invariant mass we look at the energy eigenvalues that follow from the Schrödinger equation. The energy levels up to $n = 3, L = 2$ are shown in Figure 7.4.

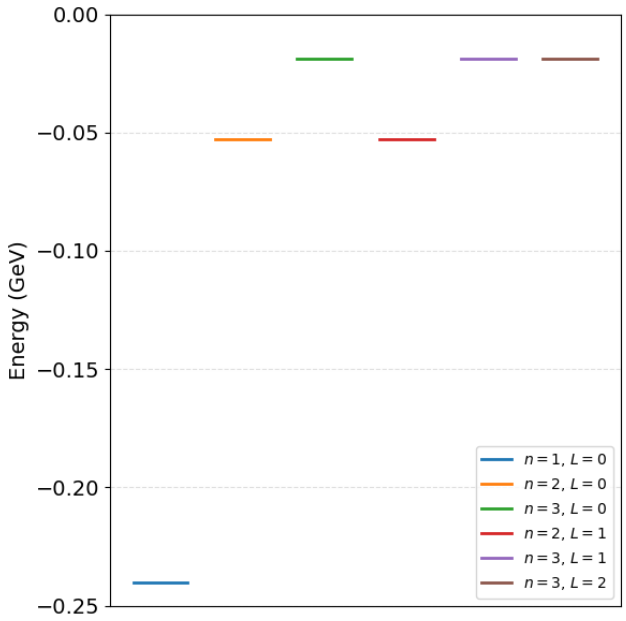

Figure 7.4: The energy levels for the different bound states with $m_\chi = 100$ GeV, $m_V = 100$ MeV and $\alpha_D = 0.1$. The energy levels are seperated horizontally to avoid overlap.

The energies could be distinguishable for different n values, if there is an accuracy of tens of MeV. To distinguish between the different L states for a given n, we would need MeV to sub-MeV precision.

For this run at $\sqrt{s} = 240$ GeV we have calculated the total cross sections for the production of the different bound states and calculated the minimal value of ϵ to expect 10 events, using the goal of an integrated luminosity of $\mathcal{L}_{\text{int}} = 10.8$ ab^{-1}. The cross sections and ϵ values are shown in Table 9.

State $n^{2S+1}L_J$	σ_{tot} (pb)	$\epsilon \geq$	State $n^{2S+1}L_J$	σ_{tot} (pb)	$\epsilon \geq$
1^1S_0	$4.67 \cdot 10^{-4}$	0.045	2^3P_1	$1.18 \cdot 10^{-6}$	0.886
2^1S_0	$5.74 \cdot 10^{-5}$	0.127	3^3P_1	$3.79 \cdot 10^{-7}$	1.563
3^1S_0	$1.65 \cdot 10^{-5}$	0.237	2^3P_2	$1.39 \cdot 10^{-6}$	0.816
1^3S_1	$7.504 \cdot 10^{-3}$	$1.11 \cdot 10^{-2}$	3^3P_2	$4.55 \cdot 10^{-7}$	1.427
2^3S_1	$9.345 \cdot 10^{-4}$	$3.14 \cdot 10^{-2}$	3^1D_2	$8.94 \cdot 10^{-11}$	101.770
3^3S_1	$2.685 \cdot 10^{-4}$	$5.87 \cdot 10^{-2}$	3^3D_1	$4.42 \cdot 10^{-11}$	144.7
2^3P_0	$1.51 \cdot 10^{-7}$	2.476	3^3D_3	$4.91 \cdot 10^{-12}$	434.3
3^3P_0	$5.04 \cdot 10^{-8}$	4.286			

Table 9: The minimum value for ϵ to expect 10 events of bound state production.

From this table we notice that we need ϵ to be orders of magnitude larger than our benchmark of $\epsilon = 10^{-4}$. These values of ϵ are already in an excluded region of the (m_V, ϵ) space, see Figure 2.1. Again, we use a physically motivated benchmark point. The aim is not to fine-tune parameters for optimal detectability, but rather to examine the expected detector signatures and assess the potential for experimental observation.

We could also consider other benchmark values, but once we, for example, consider lighter bound states we can no longer apply the non-relativistic approximation. This would require the Bethe-Salpeter formalism to make predictions.

7.2 Detector Signatures

To detect the dark matter bound states at FCC-ee we would again look for e^+e^- pairs, coming from bound states decaying to dark photons, which in turn decay to these electron-positron pairs. First we need to check whether the dark bound states decay inside of the detector. Again we look only at the decay lengths of the bound states that decay to two dark photons. The case of three dark photons is not easily calculated. The decay lengths for the two different runs we considered and the two benchmarks for m_χ are given in Table 10

State $n^{2S+1}L_J$	$\sqrt{s} = 91.2$ **GeV,** $m_\chi = 35$ **GeV**	$\sqrt{s} = 240$ **GeV,** $m_\chi = 100$ **GeV**
1^1S_0	0.31 pm	73 fm
2^1S_0	2.60 pm	589 fm
3^1S_0	10.8 pm	2.05 pm
2^3P_0	1.42 nm	0.32 nm
3^3P_0	5.27 nm	0.94 nm
2^3P_1	1.57 mm	2.86 mm
3^3P_1	5.81 mm	8.42 mm
2^3P_2	5.33 nm	1.19 nm
3^3P_2	19.8 nm	3.51 nm
3^1D_2	1.04 mm	0.16 mm

Table 10: Decay lengths of the different bound states to two dark photons, for $\alpha_D = 0.1$, $m_V = 100$ MeV and $\epsilon = 10^{-4}$ for the two FCC-ee runs. The bound states that decay to three dark photons are excluded here.

From this table, we conclude that the bound states decay well within the detector. The 2^3P_1, 3^3P_1 and 3^1D_2 states may even be observed as displaced for both runs. We assume that the bound states that decay to three dark photons show a similar behavior.

The next step is then to look at the decay products, i.e. the dark photons. The analysis here is almost identical to that done for Belle II. The only change is in the momentum of the bound state that decays to dark photons. Using the relevant momentum for the bound state, we find the following decay lengths for the dark photons in the center-of-mass frame for the Z run: 0.46 nm for the dark photons coming from the decay of 1^1S_0 and 0.31 nm for the dark photons coming from the decay of 1^3S_1. For the run at $\sqrt{s} = 240$ GeV we find 1.29 nm and 0.86 nm, respectively. The difference with decay lengths for higher n or L states is negligible as the only dependence of the state comes in the variable $m_{BS} = 2m_\chi - E_b$, where the binding energy is negligible compared to the mass m_χ. The decay probability density of the dark photons coming from the different decays, for the two runs are shown in Figure 7.5, where we used $\epsilon = 10^{-4}$.

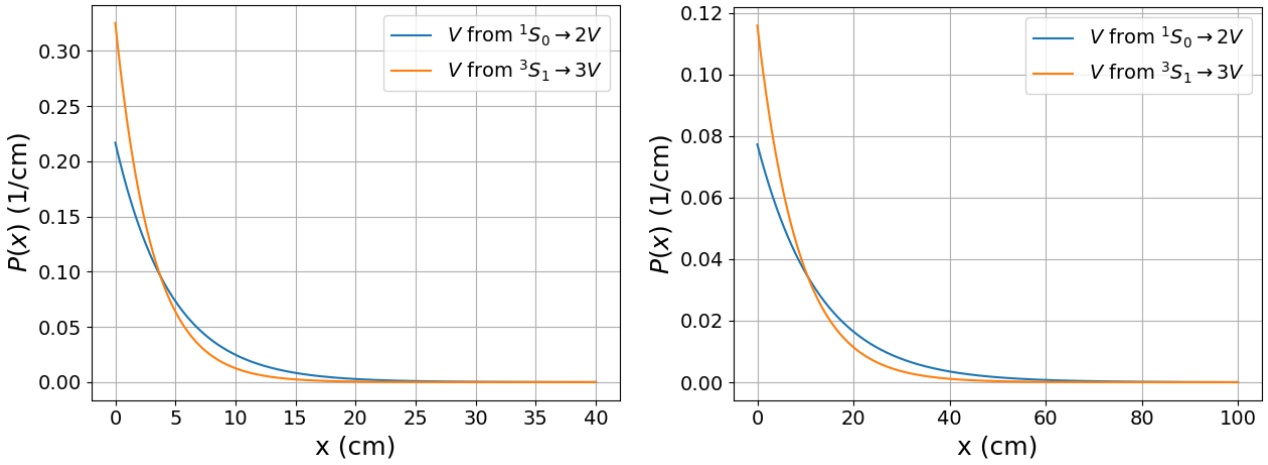

(a) $\sqrt{s} = 91.2$ GeV, $m_\chi = 35$ GeV

(b) $\sqrt{s} = 240$ GeV, $m_\chi = 100$ GeV

Figure 7.5: Decay probability densities for the dark photons coming from the $2V$ and $3V$ decay for the Z run (left) and the $\sqrt{s} = 240$ GeV run (right) for $\epsilon = 10^{-4}$, $m_V = 100$ MeV and $\alpha_D = 0.1$.

Here we see all dark photons decay on scales of (tens of) centimeters, which are resolvable distances at the FCC[26]. For experiment we would look for electron-positron pairs coming from displaced that reconstruct the invariant mass of the dark matter bound state. This may be generalized to values of ϵ for which bound states may be observed at FCC-ee, see tables 8 and 9. If we take $\epsilon > 10^{-4}$, as is needed to observe more and more bound states, the dark photons would decay faster. We consider the decay probability density as a function of distance traveled x and ϵ as in Equation 6.4. The probability of decaying within a distance a is given by

$$\mathbb{P}(x \leq a|\epsilon) = \int_0^a \frac{\epsilon^2}{\tilde{L}} e^{-\epsilon^2 x/\tilde{L}} \mathrm{d}x = 1 - e^{-\epsilon^2 a/\tilde{L}}. \tag{7.2}$$

The derivative with respect to ϵ is given by

$$\frac{\mathrm{d}}{\mathrm{d}\epsilon}\mathbb{P}(x \leq a|\epsilon) = \frac{2\epsilon a}{\tilde{L}} e^{-\epsilon^2 a/\tilde{L}} > 0. \tag{7.3}$$

Larger values of ϵ lead to a decay probability density more concentrated near the origin.

8 Conclusion

In this work, we examined dark matter bound states in the context of a dark sector composed of a dark photon and a dark fermion.

We derived general expressions for the production and decay matrix elements of bound states in the non-relativistic regime, given by equations 3.31 and 3.32. These formulas are broadly applicable and not restricted to the specific dark sector considered here.

The dark interaction was modeled by a Yukawa potential, and we numerically solved the corresponding radial Schrödinger equation (Equation 4.7). The code provided in Appendix B, was compared with known analytic solutions for the hydrogen atom, the harmonic oscillator, and an exact solution of the radial equation with a Yukawa potential. In all cases, the numerical solution was in excellent agreement with the exact results.

This numerical framework was then used to study experimental signatures of bound state production. At Belle II, we considered benchmark values of $m_V = 100\,\mathrm{MeV}$, $m_\chi \leq 5\,\mathrm{GeV}$, and $\epsilon = 10^{-4}$, which yielded a clear signal of displaced electron-positron pairs. For values of ϵ within the currently allowed range, several bound states could, in principle, be observed with the planned integrated luminosity of $\mathcal{L}_{\mathrm{int}} = 50\,\mathrm{ab}^{-1}$. In the case $\alpha_D = 0.1$, individual bound states could be distinguished, while for $\alpha_D = 0.5$, many more states appeared but many were experimentally indistinguishable. This regime approaches non-perturbative dynamics and should be interpreted with care.

At FCC-ee, the higher center-of-mass energy allows for the production of heavier dark matter bound states. We considered two benchmark runs with appropriate choices for m_χ, and identified several observable S-wave states. Observability of other states was limited due to constraints on ϵ. For bound states at FCC-ee, their presence is characterized by displaced electron-positron pair signatures.

Outlook

The methods developed in this work provide a foundation for more detailed studies of dark sector bound states. Future work could extend the numerical methods to include relativistic corrections and assess their impact on bound state properties and production rates. It would also be valuable to explore the role of bound states in cosmological settings, such as during dark matter freeze-out or dark recombination.

Experimentally, one could consider a broader range of parameter space, including larger mediator masses m_V, and study how this affects the production and decay of bound states and their signatures at different colliders. Additionally, applying these methods to more elaborate or realistic dark sector models, for example, with multiple mediators, broken symmetries, or extended particle content, could further illuminate the role of bound states. To give realistic predictions one would then also include numerical event simulations.

Appendix

A Derivation of Bound State Production Matrix Element

Here we will work out the final form of the matrix element formula for bound state production. The starting point is Equation 3.30

$$\begin{aligned}\mathcal{M}_{BS} =& \frac{\sqrt{2M}}{2m}\frac{1}{m^2}\sum_{n=0}^{\infty}\frac{1}{n!}\sum_{M_L M_S} C^{JM_J}_{LM_L SM_S}\mathrm{Tr}\left(\left.\frac{\partial^n f(\lambda)}{\partial\lambda^{\mu_1}\partial\lambda^{\mu_2}\cdots\partial\lambda^{\mu_n}}\right|_{\lambda=0} P_{SM_S}\right)\\ &\cdot\left(\int\frac{d^3\mathbf{k}}{(2\pi)^3}\lambda^{\mu_1}\lambda^{\mu_2}\cdots\lambda^{\mu_n}\psi^*_{LM_L}(\mathbf{k})\right).\end{aligned} \tag{A.1}$$

First we argue that the $n < L$ terms don't contribute. To see this we express $\lambda^{\mu_i} = k^{\mu_i}/m$ and rewrite

$$k^\mu = k\sum_{m=-1}^{1} c^\mu_{1m} Y^m_1(\hat{\mathbf{k}}), \tag{A.2}$$

which is just the spherical harmonic decomposition of the momentum components in spherical coordinates, defining $c^0_{1m} = 0$. Calculating the c^μ_{1m} explicitly one finds

$$c^\mu_{1m} = 2\sqrt{\frac{\pi}{3}}\epsilon^\mu_{(m)}, \tag{A.3}$$

where $\epsilon^\mu_{(m)}$ are just the polarization vectors of the bound state. Now, in the k integral, for n k^μ terms we get a product of n spherical harmonics

$$k^{\mu_1}k^{\mu_2}\cdots k^{\mu_n} \propto Y^{m_1}_1(\hat{\mathbf{k}})Y^{m_2}_1(\hat{\mathbf{k}})\cdots Y^{m_n}_1(\hat{\mathbf{k}}). \tag{A.4}$$

Since the spherical harmonics form a complete set, such a product of spherical harmonics can be rewritten as a linear combination of spherical harmonics. This can be achieved by the repeated use of the following formula [31]

$$Y^{m_1}_{l_1}(\theta,\phi)Y^{m_2}_{l_2}(\theta,\phi) = \frac{\sqrt{(2l_1+1)(2l_2+1)}}{4\pi}\sum_{l'=|l_1-l_2|}^{|l_1+l_2|}\sum_{m'=-l'}^{l'}\langle l_1 l_2 m_1 m_2|l'm'\rangle\langle l_1 l_2 00|l'0\rangle\sqrt{\frac{4\pi}{2l'+1}}Y^{m'}_{l'}(\theta,\phi). \tag{A.5}$$

The highest angular momentum spherical harmonic in this expansion is $l' = |l_1 + l_2|$. In the case we have n spherical harmonics all with $l_i = 1$, the highest contributing angular momentum term will be $l' = n$. Since we assumed $n < L$ there are no spherical harmonics with $l' = L$, and using the orthonormality of the spherical harmonics, there are no contributions from terms where $n < L$.

Next, we consider the $n = L$ term. We start with the complex conjugate of the inverse Fourier transform of the wave function. That is

$$\psi^*_{M_L L}(\mathbf{r}) = \int\frac{d^3k}{(2\pi)^3}e^{i\mathbf{k}\cdot\mathbf{r}}\psi^*_{M_L L}(\mathbf{k}). \tag{A.6}$$

We separate the Fourier transform of the wave function in a radial and angular part as usual, $\psi^*_{M_L L}(\mathbf{k}) = R^*_L(k)Y^{M_L *}_L(\hat{\mathbf{k}})$. The exponential term can be rewritten in terms of spherical harmonics [32]

$$e^{i\mathbf{k}\cdot\mathbf{r}} = 4\pi\sum_{\ell=0}^{\infty}\sum_{m=-\ell}^{\ell} i^\ell j_\ell(kr)Y^m_\ell(\hat{\mathbf{k}})Y^{m*}_\ell(\hat{\mathbf{r}}). \tag{A.7}$$

Here, $j_\ell(kr)$ are the spherical Bessel functions. Working out the inverse Fourier transform from this results in

$$R_L^*(r) = \frac{4\pi}{(2\pi)^3} i^L \int_0^\infty dk j_L(kr) R_L^*(k) k^2. \tag{A.8}$$

Now we take the L-th derivative with respect to r and evaluate at $r = 0$ to find

$$\frac{d^L}{dr^L} R_L^*(r)\bigg|_{r=0} = \frac{4\pi}{(2\pi)^3} i^L \int_0^\infty dk \left(\frac{\partial^L}{\partial r^L} j_L(kr)\right)\bigg|_{r=0} R_L^*(k) k^2. \tag{A.9}$$

Then using

$$\left(\frac{\partial^L}{\partial r^L} j_L(kr)\right)\bigg|_{r=0} = \frac{2^{-1-L} k^L \sqrt{\pi}\Gamma(1+L)}{\Gamma(L+\frac{3}{2})} \tag{A.10}$$

and rewriting we find

$$\int_0^\infty dk R_L^*(k) k^{2+L} = \frac{(2\pi)^3}{4\pi i^L} \frac{\Gamma(L+\frac{3}{2}) 2^{1+L}}{\sqrt{\pi}\Gamma(1+L)} \frac{d^L}{dr^L} R_L^*(r)\bigg|_{r=0}. \tag{A.11}$$

Here we need to make an important observation. The left-hand side is exactly the radial part of the momentum integral in our matrix element formula. This means that we have all the ingredients to calculate the term $n = L$ in the matrix element formula.

Lastly, we observe that since we are working in the non-relativistic limit, we expand in a small parameter k/m. Subsequent terms in the sum will contribute less and less. As we have shown that $n = L$ is the smallest value of n that contributes, we can state that the $n = L$ term is the dominant contribution in our non-relativistic approximation. Even though we have an integral over all momenta, the momentum space wave function has no support for high momenta in the non-relativistic limit.

B Python Code

Below is the Python code used to determine solutions of the radial Equation 4.7 numerically.

```
import numpy as np
import matplotlib.pyplot as plt
from scipy.linalg import eigvalsh_tridiagonal
from scipy.linalg import eigh_tridiagonal




alpha_D=0.1                    #Interaction strength, Yukawa=-alpha_D/r e^{-mr}
MV=0.1             #Mediator mass, see Yukawa potential expressed in GeV
mchi=100                   #Dark fermion mass
mu = mchi/2                    #reduced mass of the system in units of GeV
a_0=1/(mu*alpha_D)
print("With the chosen parameters delta = {:5.4f}".format(MV*a_0))

critical_lengths = {(1, 0): 1.1906124207,(2, 0): 0.3102092834,(2, 1):
    0.220118,(3, 0): 0.139450295,(3, 1): 0.11265,(3, 2): 0.0913384,(4, 0):
    0.0788281106,(4, 1): 0.067827,(4, 2): 0.058099,(5, 0): 0.0505831707,(5,
    1): 0.045155,(5, 2): 0.0400197,(6, 0): 0.035183478,(6, 1): 0.0321562,(6,
    2): 0.0291623,(7, 0): 0.02586938,(7, 1): 0.024026435,(7, 2):
    0.0221591,(8, 0): 0.0198221,(8, 1): 0.01862667,(8, 2): 0.01738685,(9, 0):
     0.0156708,(9, 1): 0.0148561,(9, 2): 0.01399716,}

def get_present_states(delta):
    present_states = []
    for (n, l), crit in critical_lengths.items():
        if delta < crit:
            present_states.append((n, l))
    return present_states

print(get_present_states(MV*a_0))

def plot(r, densities, eigenvalues, num_wavefunctions=3):
    plt.xlabel('r ($a_{0}$)')
    plt.ylabel(r'$P_{nl}(r)$ $(a_0)$')

    # Ensure we don't try to plot more wavefunctions than there are
       eigenvalues
    num_wavefunctions = min(num_wavefunctions, len(eigenvalues))

    # Generate labels for the wavefunctions
    energies = ['E = {: >5.6f} GeV'.format(eigenvalues[i].real) for i in
       range(num_wavefunctions)]

    # Plot each density
    for i in range(num_wavefunctions):
        if eigenvalues[i]<0:
            plt.plot(r/a_0, a_0*densities[i], label=energies[i])

    plt.legend()
    plt.show()
    return

N = 10000
l = 2
r = np.linspace(2e-15, 0.0, N, endpoint=False)*5067730.178*10**9 #Converting
```

```
    meters to GeV^{-1}
49
50
51  a = np.abs(r[1] - r[0])
52
53  laplace_main_diag = -2.0 / a**2 * np.ones(N)
54  laplace_off_diag = 1.0 / a**2 * np.ones(N - 1)
55
56  angular_term_main_diag = l * (l + 1) / r**2
57  potential_term_main_diag = -(alpha_D / r) * np.exp(-MV * r)
58
59  main_diag = -1 / (2.0 * mu) * (laplace_main_diag - angular_term_main_diag) +
        potential_term_main_diag
60  off_diag = -1 / (2.0 * mu) * laplace_off_diag
61  eigenvalues, eigenvectors =eigh_tridiagonal(main_diag, off_diag,
       eigvals_only=False, select='i', select_range=(0,6), check_finite=True,
       tol=0.0, lapack_driver='auto')
62
63  #sort eigenvalue and eigenvectors
64  eigenvectors = np.array([x for _, x in sorted(zip(eigenvalues, eigenvectors.
       T), key=lambda pair: pair[0])])
65  eigenvalues = np.sort(eigenvalues)
66
67  #Normalizing the eigenvectors
68  for i in range(len(eigenvectors)):
69      Norm=0
70      for j in eigenvectors[i]:
71          Norm += np.abs(j)**2
72      eigenvectors[i]=eigenvectors[i]/np.sqrt(np.abs(r[0]-r[1])*Norm)
73
74  #compute probability density for each eigenvector
75  densities = [np.absolute(eigenvectors[i, :])**2 for i in range(len(
       eigenvalues))]
76
77
78
79  plot(r, densities, eigenvalues, num_wavefunctions=5)
80
81  Psi0sq = (1/(4*np.pi))*np.abs((densities[0][-1])/(r[-1]**2))#Valid if l=0
82  dR0sq= (((np.sqrt(densities[0][-2])-2*np.sqrt(densities[0][-1]))/(2*(r
       [-1]**2)))**2)#valid if l=1
83  ddR0sq = (((-np.sqrt(densities[0][-3])+3*np.sqrt(densities[0][-2])-3*np.sqrt
       (densities[0][-1]))/(3*(r[-1]**3)))**2)#valid if l=2
84
85  print(eigenvalues[0],";",eigenvalues[1],";",eigenvalues[2],";",eigenvalues
       [3],";",eigenvalues[4])
```

Listing 1: Python code to solve the radial equation numerically

C Reproducing Known Results

To test the code for accuracy, we can compare the results from the discretization procedure with those of exactly solvable problems with spherically symmetric potentials, such as the hydrogen atom and the 3D harmonic oscillator. We will also compare the results from the approximation with those of an exact power series solution to the problem of the radial equation with a Yukawa potential.

C.1 The Coulomb Potential

The Coulomb potential describes the bound state of a hydrogen atom. It is one of the few realistic models that is exactly solvable. The exact solution is given by the following formula [16]

$$\psi_{nlm} = \sqrt{\left(\frac{2}{na_0}\right)^3 \frac{(n-l-1)!}{2n(n+l)!}} e^{-\frac{r}{na_0}} \left(\frac{2r}{na_0}\right)^l L_{n-l-1}^{2l+1}\left(\frac{2r}{na_0}\right) Y_l^m(\theta,\phi). \tag{C.1}$$

Here L_{n-l-1}^{2l+1} are the associated Laguerre polynomials and a_0 is the Bohr radius. From this, the radial wave functions are easily found. The radial wave functions for the first three lowest n values are given in Table 11.

n	**l**	**Radial wave function** $R_{nl}(r)$
1	0	$R_{10}(r) = 2\left(\frac{1}{a_0}\right)^{3/2} e^{-\frac{r}{a_0}}$
2	0	$R_{20}(r) = \frac{1}{\sqrt{2}}\left(\frac{1}{a_0}\right)^{3/2}\left(1-\frac{r}{2a_0}\right) e^{-\frac{r}{2a_0}}$
2	1	$R_{21}(r) = \frac{1}{2\sqrt{6}}\left(\frac{1}{a_0}\right)^{3/2}\left(\frac{r}{a_0}\right) e^{-\frac{r}{2a_0}}$
3	0	$R_{30}(r) = \frac{2}{3\sqrt{3}}\left(\frac{1}{a_0}\right)^{3/2}\left(1-\frac{2r}{3a_0}+\frac{2}{27}\left(\frac{r}{a_0}\right)^2\right) e^{-\frac{r}{3a_0}}$
3	1	$R_{31}(r) = \frac{8}{27\sqrt{6}}\left(\frac{1}{a_0}\right)^{3/2}\left(1-\frac{r}{6a_0}\right)\left(\frac{r}{a_0}\right) e^{-\frac{r}{3a_0}}$
3	2	$R_{32}(r) = \frac{4}{81\sqrt{30}}\left(\frac{1}{a_0}\right)^{3/2}\left(\frac{r}{a_0}\right)^2 e^{-\frac{r}{3a_0}}$

Table 11: Radial wave functions $R_{n,l}(r)$ of the hydrogen atom for $n = 1, 2, 3$ and corresponding allowed values for l.

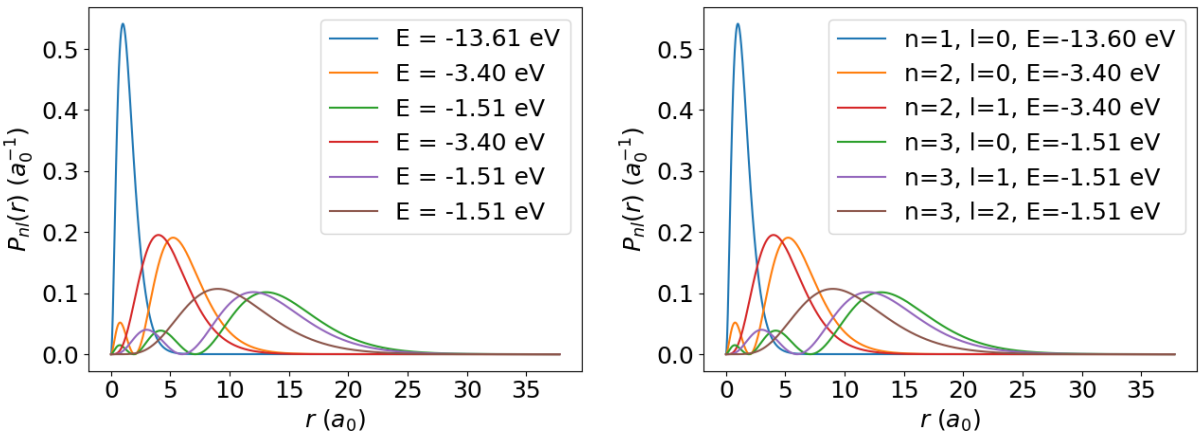

(a) (b)

Figure C.1: Comparison of the radial probability densities of the hydrogren atom. On the left the result of the code is shown with $N = 6000$, on the right the exact solutions are shown.

These tabulated radial wave functions can be converted to radial probability densities using

$$P_{nl}(r) = r^2 |R_{nl}(r)|^2. \tag{C.2}$$

The probability densities are plotted in Figure C.1(b). The results from the numerical calculation are given in Figure C.1(a). Visually this looks like a very good approximation. To take a closer look we can consider the relative error between the probability densities, and see how they change with the choice of N. The relative error in the radial probability density between the exact solution and the numerical approach is shown in Figure C.2.

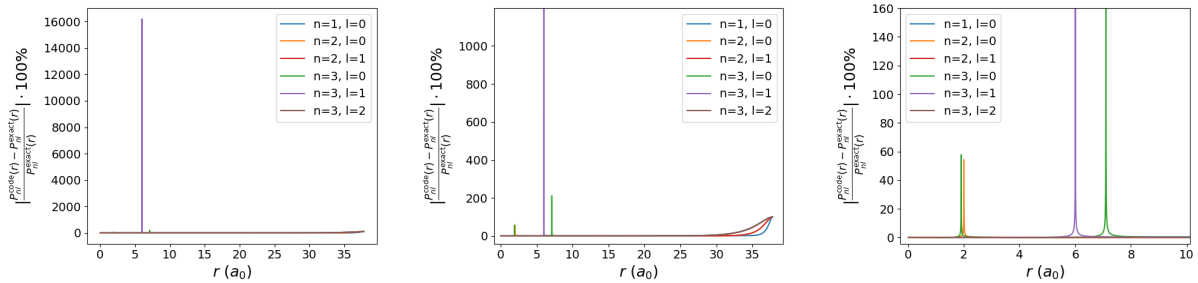

(a) (b) (c)

Figure C.2: Relative error between the numerical approach and the exact solution calculated using $\left|\frac{P_{nL}^{Code}(r) - P_{nL}^{Exact}(r)}{P_{nL}^{Exact}(r)}\right| \cdot 100\%$. From left to right the plot is zoomed in more. Peaks here correspond to the comparison of extremely small values which leads to large error.

These plots have some interesting features. First is the behavior of the relative error as r goes to $r \approx 35a_0$, the relative error becomes large. This is a feature all of the radial probabilities share, albeit to a much smaller extent for the higher energy states. The reason here is the comparison of extremely small values. The maximum error for $(n, l) = (1, 0)$ occurs when we compare a probability density on the order of 10^{-26} from the numerical approach to one on the order of 10^{-30} from the exact solution. For all practical purposes the radial probability density is zero here, so we ignore this error.

The other errors occur in certain peaks. The interesting thing here is that these large error peaks have the same origin as those as r becomes large. The peaks occur precisely where we

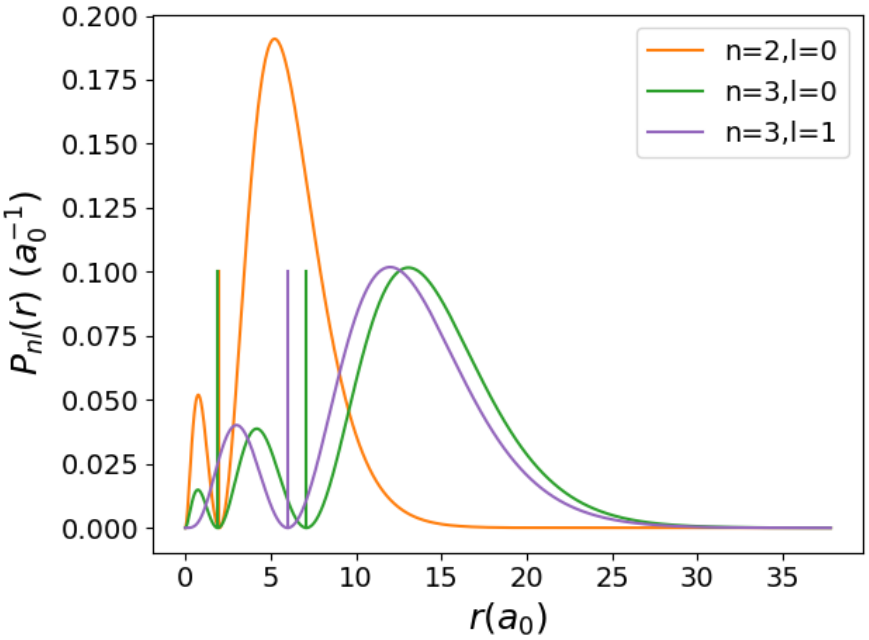

Figure C.3: Locations of the error peaks, compared to the locations of the zeroes of the probability density functions.

expect the radial probability density to become zero. This is seen easily when we overlay the locations of these peaks over the radial probability densities. The results of this are shown in Figure C.3.

An important note is that the point $r = 0$ is excluded from the figures and the boundary condition ensures that there the probability densities are zero, meaning no such error can occur here. Because of this, the peaks do not give a good indication of the accuracy of the method. As we are especially interested in the behavior of $|R(r)|^2$ and $|R'(r)|^2$ near the origin, looking at the error there as a function of N is a better idea. To determine the accuracy for the values of $|R(0)|^2$, we only consider the S-wave states, as for all other states this quantity is zero, as discussed in Section 4.1.2. The accuracy in terms of N is shown in Figure C.4.

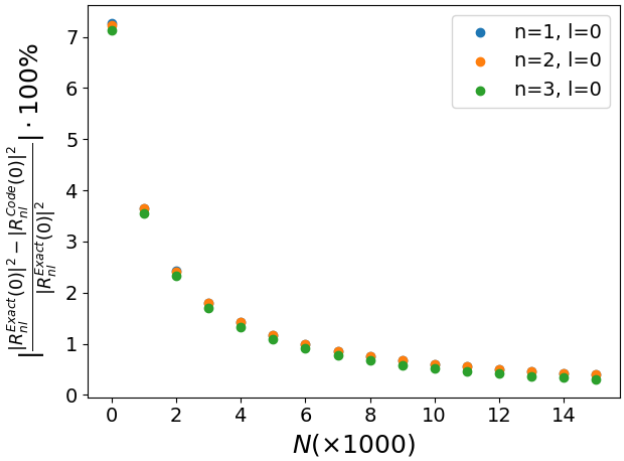

Figure C.4: The relative error between the numerical and exact calculation of the quantity $|R(0)|^2$ as a function of N calculated using $\left|\frac{|R_{nL}^{Exact}(0)|^2 - |R_{nL}^{Code}(0)|^2}{|R_{nL}^{Exact}(0)|^2}\right| \cdot 100\%$. As can be seen, the greater the chosen value of N the better the approximation.

For $|R'(0)|^2$ we know that it is only non-zero for P-wave states. Repeating the above analysis, we find the result given in Figure C.5.

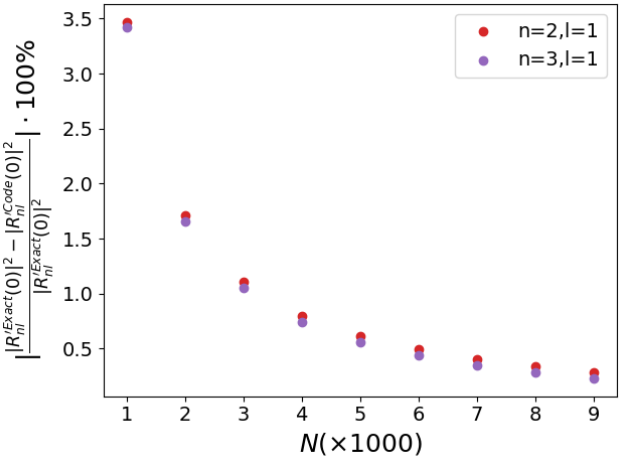

Figure C.5: The relative error between the numerical and exact calculation of the quantity $|R'(0)|^2$ as a function of N. As can be seen, the greater the chosen value of N the better the approximation.

What is immediately clear from this analysis is that the bigger N, the better the approximation becomes, as was expected.

C.2 The 3D Harmonic Oscillator

The 3D harmonic oscillator is another exactly solvable system against which the numerical approach can be tested. In this case the potential is given by

$$V(r) = \frac{1}{2}\mu\omega^2 r^2, \tag{C.3}$$

where ω is the angular frequency of the oscillator. The exact wave functions are then given by [31]

$$\psi_{klm}(r,\theta,\phi) = \sqrt{\sqrt{\frac{2\nu^3}{\pi}}\frac{2^{k+2l+3}k!\nu^l}{(2k+2l+1)!!}}r^l e^{-\nu r^2} L_k^{(l+1/2)}(2\nu r^2) Y_l^m(\theta,\phi), \tag{C.4}$$

where $\nu = \frac{\mu\omega}{2}$. For the energy levels, we have

$$E = \omega(2k + l + \frac{3}{2}). \tag{C.5}$$

The principal quantum number is related to k and l via $n = 2k + l$, where $k \in \{0, 1, 2, \ldots\}$. In the case of the harmonic oscillator we only have even (odd) l values, for even (odd) n values. For the first few wave functions the radial probability density $r^2|R_{nl}(r)|^2$ is shown Figure C.6.

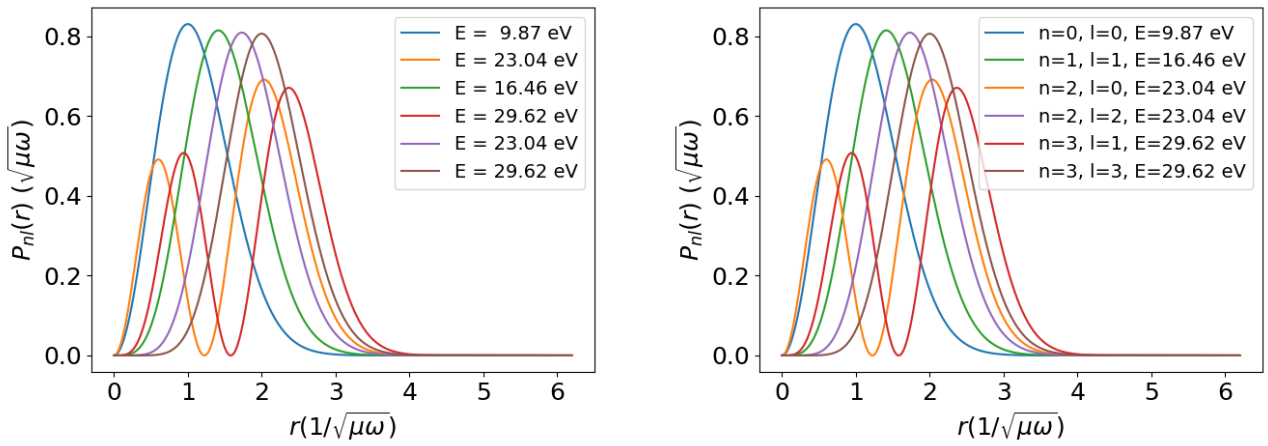

(a) (b)

Figure C.6: The radial probability densities $r^2|R_{nl}(r)|^2$ for the harmonic oscillator with $\omega = 10^{16}$ rad/s ≈ 6.582 eV. In (a) the result from the numerical approach is shown. In (b) the exact solutions are shown.

Here we again see that the numerical approach seems to give a good approximation. We can repeat the analysis as done for the hydrogen case and look at the relative error between the two cases, the result of this is shown in Figure C.7. The same behavior as in the hydrogen case

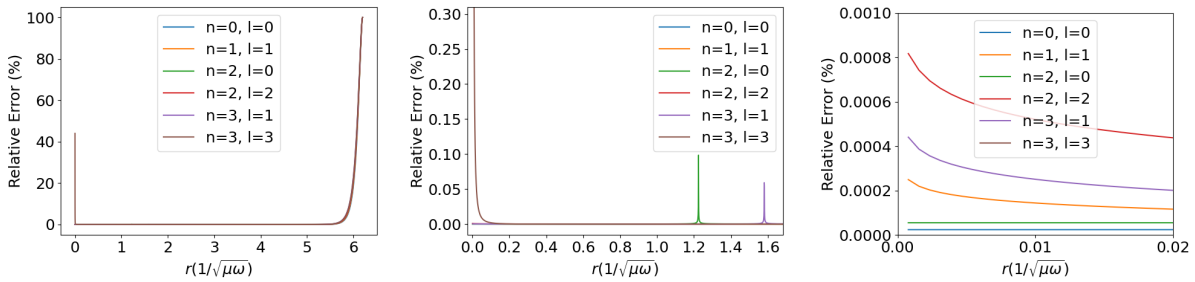

(a) (b) (c)

Figure C.7: Relative error in the radial probability density between the numerical approach and the exact solution of the harmonic oscillator. From left to right the plot is zoomed in more. Peaks here correspond to the comparison of extremely small values which leads to large error

is observed. As r becomes large, we compare incredibly small numbers that for all practical purposes are zero. This leads to large errors, as we are limited by the accuracy of the code. There are again peaks, which correspond to the roots of the probability densities. This time, the $r = 0$ point becomes problematic, too. The origin of the error here is the same; we compare incredibly small numbers. Fortunately, it is only $l \neq 0$ functions that behave like this near the origin, we already know from our earlier analysis in Section 4.1.2 that $|R(0)|^2 = 0$ for $l \neq 0$, so this does not lead to problems. However, the precision of these probability densities would become important, once we consider the absolute value squared of the l^{th} derivative of $R(r)$, evaluated at the origin. As the errors are extremely small near the origin, we do not run into problems here. The analysis of the accuracy of $|R(0)|^2$ as a function of N is given in Figure C.8.

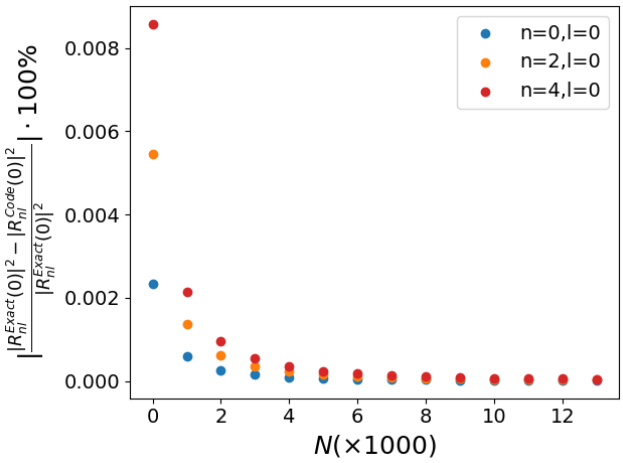

Figure C.8: Relative error in the quantity $|R(0)|^2$ between the numerical and exact solutions for the harmonic oscillator. The relative error is small and decreases with increasing N.

The behavior is exactly what we would expect and the same as what we have seen in the hydrogen case; the larger N, the better the approximation.

D Exact and Numerical Radial Probability Density for Varying δ

Below is illustrated how increasing δ closer to the continuum results in the exact solution of Ref. [19] diverging from the numerical calculations.

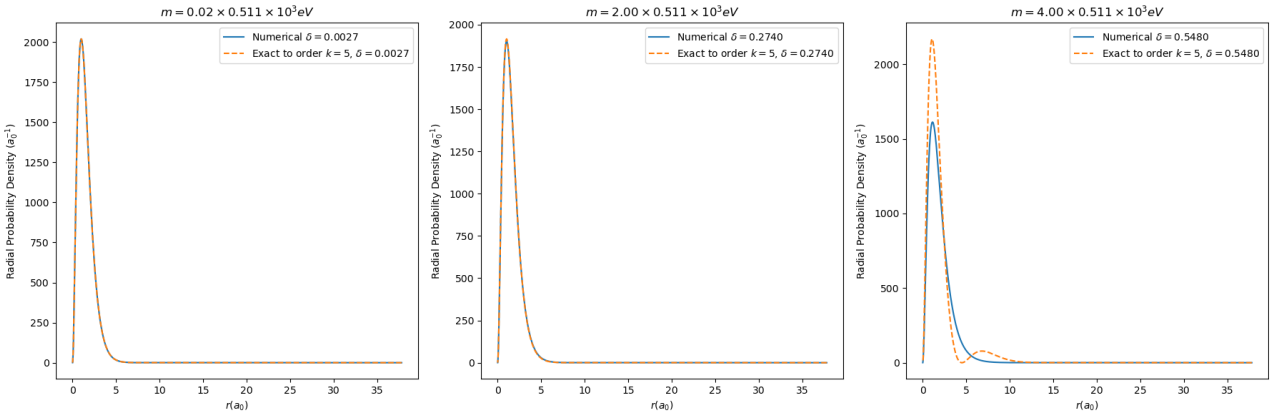

Figure D.1: Comparison of $n = 1, L = 0$ states as calculated numerically and in Ref. [19], for varying δ. δ is varied by varying the mediator mass m.

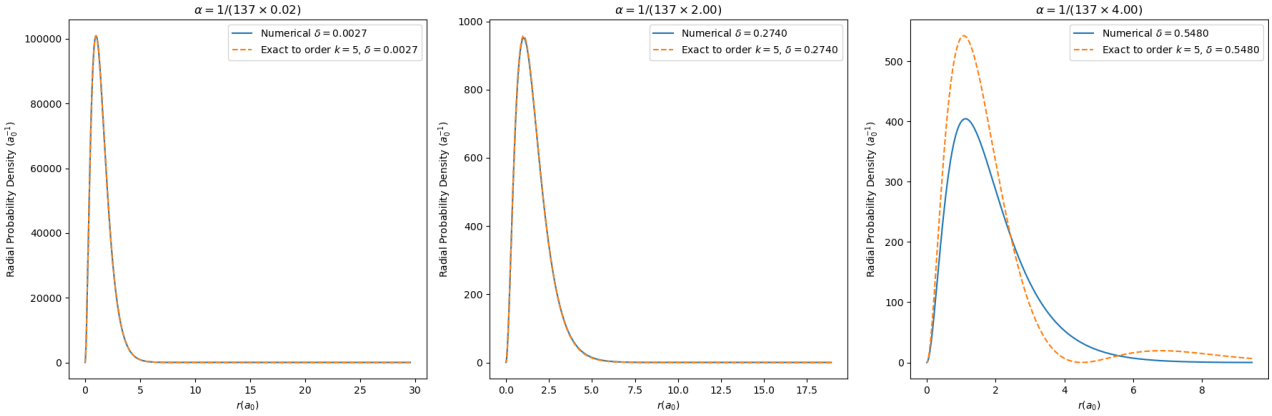

Figure D.2: Comparison of $n = 1, L = 0$ states as calculated numerically and in Ref. [19], for varying δ. δ is varied by varying the interaction strength α.

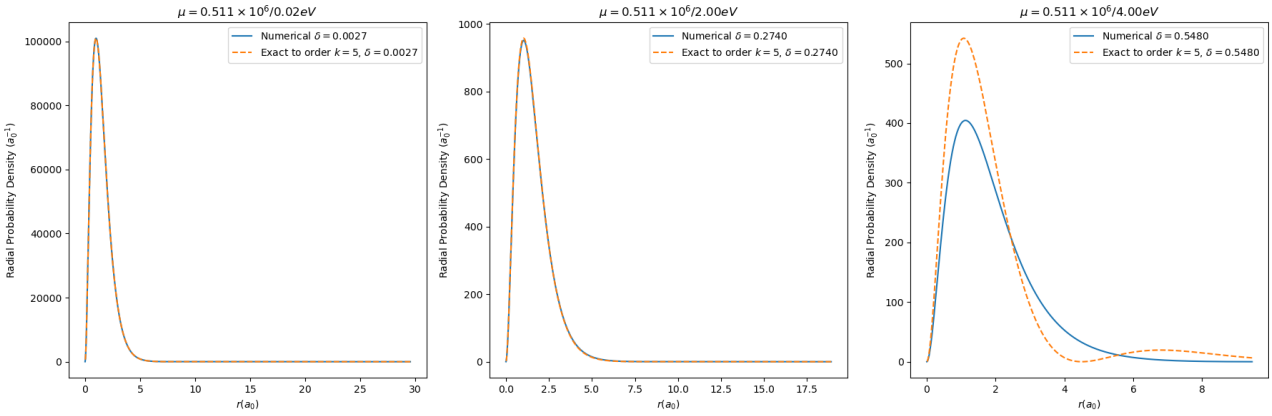

Figure D.3: Comparison of $n = 1, L = 0$ states as calculated numerically and in Ref. [19], for varying δ. δ is varied by varying the reduced mass μ.

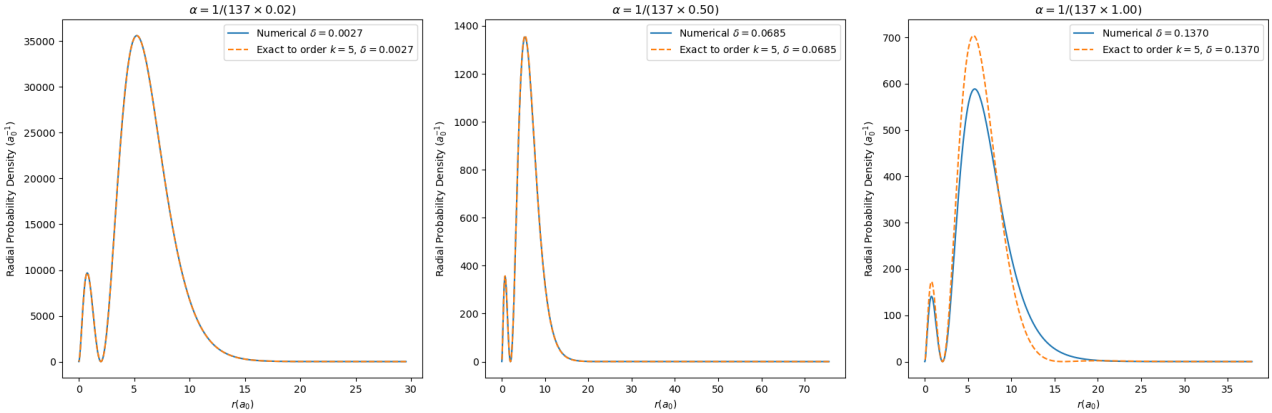

Figure D.4: Comparison of $n = 2, L = 0$ states as calculated numerically and in Ref. [19], for varying δ. δ is varied by varying the interaction strength α.

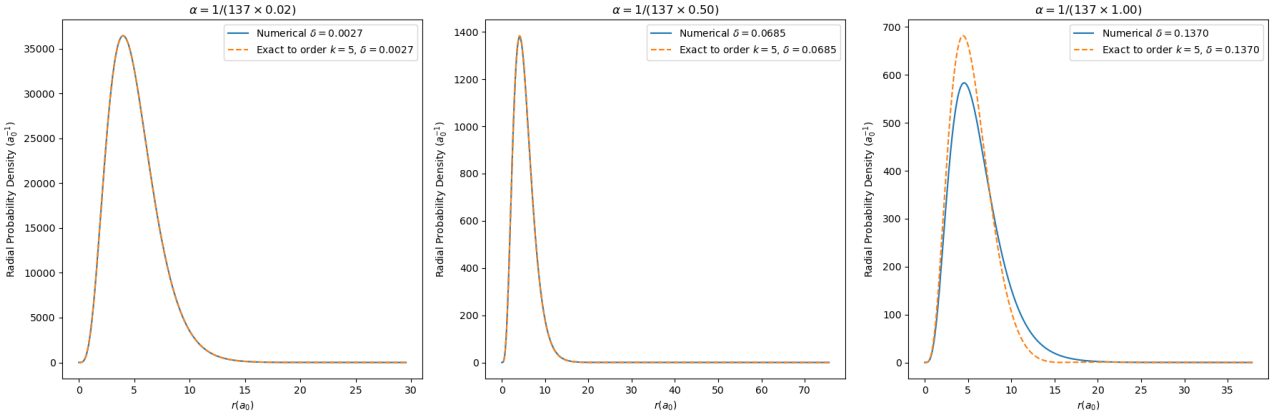

Figure D.5: Comparison of $n = 2, L = 1$ states as calculated numerically and in Ref. [19], for varying δ. δ is varied by varying the interaction strength α.

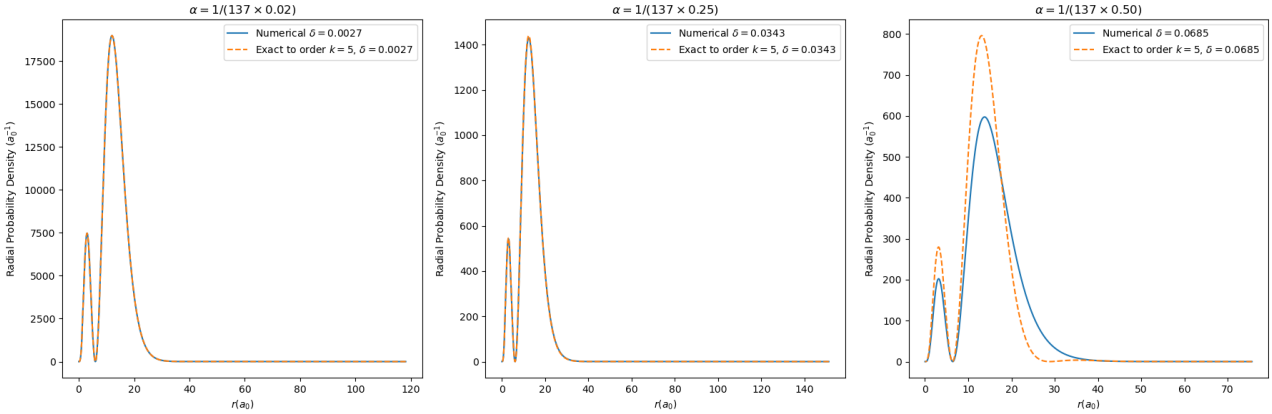

Figure D.6: Comparison of $n = 3, L = 1$ states as calculated numerically and in Ref. [19], for varying δ. δ is varied by varying the interaction strength α.

E Kinematics of Dark Photons

Here we will work out the momentum of the dark photon in the electron-positron center-of-mass frame. The dark photons originate from the bound state that decays. We consider this decay in the rest frame of the bound state. Its four momentum is then

$$p^{\mu}_{BS} = \begin{pmatrix} m_{BS} \\ 0 \\ 0 \\ 0 \end{pmatrix} \tag{E.1}$$

When it decays n_V to dark photons with momenta k^{μ}_i and $i \in \{1, \ldots, n_V\}$, energy momentum conservation requires

$$\sum_i k^0_i = m_{BS} \tag{E.2}$$

and

$$\sum_i \mathbf{k}_i = 0. \tag{E.3}$$

To use Equation E.2 we make our first approximation and assume that the energy of the bound state is equally divided among the dark photons. In the case of the decay to two dark photons this is exact, in the case of the decay to three dark photons this is an approximation. With this, the spatial momentum of the dark photon in the bound state rest frame becomes

$$|\mathbf{k}_i| = \sqrt{\left(\frac{m_{BS}}{n_V}\right)^2 - m_V^2}. \tag{E.4}$$

, where n_V is the number of dark photons. Now we will adopt the following notation $x^{\text{frame}}_{\text{particle}}$, where x will be any quantity we are interested in, frame will be BS for the bound state rest frame or CM for the center-of-mass frame and particle will be either BS to indicate the bound state or V to indicate the dark photon. In the CM frame the bound state has momentum

$$\mathbf{p}^{CM}_{BS} = \gamma m_{BS} \boldsymbol{\beta}_{BS} = E^{CM}_{BS} \boldsymbol{\beta}_{BS}.$$

To boost from the bound state rest frame to the center-of-mass frame we will need the boost described by $\boldsymbol{\beta}_{BS}$. Now we take our four momentum of a dark photon $k^{BS,\mu}_V$ and split the spatial part $\mathbf{k}^{BS}_V$ in a part parallel to $\boldsymbol{\beta}_{BS}$ and a part normal to it, that is

$$\mathbf{k}^{BS}_V = \mathbf{k}^{BS}_{V\perp} + \mathbf{k}^{BS}_{V\parallel},$$

where

$$\mathbf{k}^{BS}_{V\parallel} = (\mathbf{k}^{BS}_V \cdot \hat{\mathbf{n}})\hat{\mathbf{n}},$$

and $\hat{\mathbf{n}} = \frac{\boldsymbol{\beta}_{BS}}{\beta_{BS}}$. Upon boosting, the normal component remains unchanged. The parallel component transforms like

$$\mathbf{k}^{CM}_{V\parallel} = \gamma \boldsymbol{\beta}_{BS} k^{BS,0}_V + \gamma \mathbf{k}^{BS}_{V\parallel}$$

and

$$k^{CM,0}_V = \gamma \left(k^{BS,0}_V + \mathbf{k}^{BS}_V \cdot \boldsymbol{\beta}_{BS} \right),$$

where γ is the Lorentz factor determined by β_{BS}, i.e. $\gamma = E^{CM}_{BS}/m_{BS}$. The total transformation is then given by

$$k^{CM,\mu}_V = \begin{pmatrix} \gamma \left(k^{BS,0}_V + \mathbf{k}^{BS}_V \cdot \boldsymbol{\beta}_{BS} \right) \\ \mathbf{k}^{BS}_V + \left((\gamma - 1) \frac{\mathbf{k}^{BS}_V \cdot \boldsymbol{\beta}_{BS}}{\beta^2_{BS}} + \gamma k^{BS,0}_V \right) \boldsymbol{\beta}_{BS} \end{pmatrix} \tag{E.5}$$

From this we find the magnitude of the dark photon momentum to be given by

$$\begin{aligned}|\mathbf{k}_V^{CM}|^2 =&|\mathbf{k}_V^{BS}|^2 + 2\left(\frac{E_{BS}^{CM}}{m_{BS}} - 1\right)|\mathbf{k}_V^{BS}|^2\cos^2\alpha + 2\frac{|\mathbf{k}_V^{BS}||\mathbf{p}_{BS}^{CM}|}{n_V}\cos\alpha \\ &+ \left(\frac{E_{BS}^{CM}}{m_{BS}} - 1\right)^2|\mathbf{k}_V^{BS}|^2\cos^2\alpha + \frac{|\mathbf{p}_{BS}^{CM}|^2}{n_V^2} + 2\left(\frac{E_{BS}^{CM}}{m_{BS}} - 1\right)\frac{|\mathbf{k}_V^{BS}|}{n_V}|\mathbf{p}_{BS}^{CM}|\cos\alpha.\end{aligned} \tag{E.6}$$

Here, the angle α is the angle between the boost direction and the dark photon momentum in the bound state rest frame. We have no information on this angle, since we do not do extensive simulations in which we could sample the space, we will average the quantity $|\mathbf{k}_V^{CM}|$ over the solid angle when using it, that is

$$|\mathbf{k}_V^{CM}| \equiv \frac{1}{4\pi}\int \mathrm{d}\Omega|\mathbf{k}_V^{CM}|(\alpha). \tag{E.7}$$

The bound state energy and momentum in the CM frame follow from the kinematics of its production process, i.e. $e^+e^- \to BS + X$, where $X = \gamma, V, Z$.

References

[1] F. Zwicky. "Die Rotverschiebung von extragalaktischen Nebeln". In: *Helv. Phys. Acta* 6 (1933), pp. 110–127. DOI: 10.1007/s10714-008-0707-4.

[2] V C Rubin and W K Ford Jr. "ROTATION OF THE ANDROMEDA NEBULA FROM A SPECTROSCOPIC SURVEY OF EMISSION REGIONS." In: *Astrophys. J. 159: 379-403(Feb 1970).* (Jan. 1970). DOI: 10.1086/150317. URL: https://www.osti.gov/biblio/4148861.

[3] R. D. Peccei and H. R. Quinn. "CP Conservation in the Presence of Instantons". In: *Phys. Rev. Lett.* 38 (1977), pp. 1440–1443.

[4] Scott Dodelson and Lawrence M. Widrow. "Sterile neutrinos as dark matter". In: *Phys. Rev. Lett.* 72 (1994), pp. 17–20.

[5] Gerard Jungman, Marc Kamionkowski, and Kim Griest. "Supersymmetric dark matter". In: *Physics Reports* 267.5 (1996), pp. 195–373. ISSN: 0370-1573. DOI: https://doi.org/10.1016/0370-1573(95)00058-5. URL: https://www.sciencedirect.com/science/article/pii/0370157395000585.

[6] B. Holdom. "Two U(1)'s and Epsilon Charge Shifts". In: *Phys. Lett. B* 166 (1986), pp. 196–198.

[7] M. J. Strassler and Kathryn M. Zurek. "Echoes of a hidden valley at hadron colliders". In: *Phys. Lett. B* 651 (2007), pp. 374–379.

[8] Haipeng An et al. "Probing the Dark Sector with Dark Matter Bound States". In: *Physical Review Letters* 116.15 (Apr. 2016). ISSN: 1079-7114. DOI: 10.1103/physrevlett.116.151801. URL: http://dx.doi.org/10.1103/PhysRevLett.116.151801.

[9] Jim Alexander et al. *Dark Sectors 2016 Workshop: Community Report.* 2016. arXiv: 1608.08632 [hep-ph]. URL: https://arxiv.org/abs/1608.08632.

[10] Martin Bauer, Patrick Foldenauer, and Joerg Jaeckel. "Hunting all the hidden photons". In: *Journal of High Energy Physics* 2018.7 (July 2018). ISSN: 1029-8479. DOI: 10.1007/jhep07(2018)094. URL: http://dx.doi.org/10.1007/JHEP07(2018)094.

[11] Gaia Lanfranchi, Maxim Pospelov, and Philip Schuster. "The Search for Feebly Interacting Particles". In: *Annual Review of Nuclear and Particle Science* 71.1 (Sept. 2021), pp. 279–313. ISSN: 1545-4134. DOI: 10.1146/annurev-nucl-102419-055056. URL: http://dx.doi.org/10.1146/annurev-nucl-102419-055056.

[12] Johann H. Kühn, Jean Kaplan, and El Ghali Oudrhiri Safiani. "Electromagnetic annihilation of e+e into quarkonium states with even charge conjugation". In: *Nuclear Physics B* 157.1 (1979), pp. 125–144. ISSN: 0550-3213. DOI: https://doi.org/10.1016/0550-3213(79)90055-5. URL: https://www.sciencedirect.com/science/article/pii/0550321379900555.

[13] Michael Edward Peskin and Daniel V. Schroeder. *An Introduction to Quantum Field Theory.* Reading, USA: Addison-Wesley (1995) 842 p. Westview Press, 1995.

[14] David J Griffiths. *Introduction to elementary particles; 2nd rev. version.* Physics textbook. New York, NY: Wiley, 2008. URL: https://cds.cern.ch/record/111880.

[15] A. Petrelli et al. "NLO Production and Decay of Quarkonium". In: *Nucl.Phys.B514:245-309,1998* (July 1997). DOI: 10.1016/S0550-3213(97)00801-8. arXiv: hep-ph/9707223 [hep-ph].

[16] David J. Griffiths and Darrell F. Schroeter. *Introduction to quantum mechanics*. Third edition. Cambridge ; New York, NY: Cambridge University Press, 2018. ISBN: 978-1-107-18963-8.

[17] William Shepherd, Tim M. P. Tait, and Gabrijela Zaharijas. "Bound states of weakly interacting dark matter". In: *Physical Review D* 79.5 (Mar. 2009). ISSN: 1550-2368. DOI: 10.1103/physrevd.79.055022. URL: http://dx.doi.org/10.1103/PhysRevD.79.055022.

[18] C. Quigg and Jonathan L. Rosner. "Quantum mechanics with applications to quarkonium". In: *Physics Reports* 56.4 (1979), pp. 167–235. ISSN: 0370-1573. DOI: https://doi.org/10.1016/0370-1573(79)90095-4. URL: https://www.sciencedirect.com/science/article/pii/0370157379900954.

[19] M Napsuciale and S Rodríguez. "Bound states of the Yukawa potential from hidden supersymmetry". In: *Progress of Theoretical and Experimental Physics* 2021.7 (June 2021), 073B03. ISSN: 2050-3911. DOI: 10.1093/ptep/ptab070. eprint: https://academic.oup.com/ptep/article-pdf/2021/7/073B03/39456304/ptab070.pdf. URL: https://doi.org/10.1093/ptep/ptab070.

[20] K. F. Riley, M. P. Hobson, and S. J. Bence. *Mathematical Methods for Physics and Engineering: A Comprehensive Guide*. 3rd ed. Cambridge University Press, 2006.

[21] L. Bergström, H. Grotch, and R. W. Robinett. "D-wave quarkonium production and annihilation decays: Formalism and applications". In: *Phys. Rev. D* 43 (7 Apr. 1991), pp. 2157–2160. DOI: 10.1103/PhysRevD.43.2157. URL: https://link.aps.org/doi/10.1103/PhysRevD.43.2157.

[22] T. Abe et al. *Belle II Technical Design Report*. 2010. arXiv: 1011.0352 [physics.ins-det]. URL: https://arxiv.org/abs/1011.0352.

[23] Belle II Collaboration. *Presentation at MPP Munich Workshop 2023*. https://indico.mpp.mpg.de/event/2308/contributions/4092/attachments/3414/3799/Belle2NumberingSchem pdf. Accessed: 2025-06-30. 2023.

[24] Patrick Ecker. "Search for a dark Higgs boson produced in association with inelastic dark matter at the Belle II experiment". PhD thesis. Karlsruhe Institute of Technology (KIT), 2024.

[25] K. Adamczyk et al. "The design, construction, operation and performance of the Belle II silicon vertex detector". In: *Journal of Instrumentation* 17.11 (Nov. 2022), P11042. ISSN: 1748-0221. DOI: 10.1088/1748-0221/17/11/p11042. URL: http://dx.doi.org/10.1088/1748-0221/17/11/P11042.

[26] Wolfgang Bartmann et al. *Future Circular Collider Feasibility Study Report Volume 1: Physics and Experiments*. 2025. DOI: 10.17181/CERN.9DKX.TDH9. URL: http://cds.cern.ch/record/2928193.

[27] Michael Benedikt et al. *Future Circular Collider Feasibility Study Report Volume 2: Accelerators, technical infrastructure and safety*. 2025. DOI: 10.17181/CERN.EBAY.7W4X. URL: http://cds.cern.ch/record/2928793.

[28] Johannes Gutleber, Luisa Ulrici, and Timothy Paul Watson. *Future Circular Collider Feasibility Study Report Volume 3: Civil Engineering, Implementation and Sustainability*. 2025. DOI: 10.17181/CERN.I26X.V4VF. URL: http://cds.cern.ch/record/2928194.

[29] CERN. *Future Circular Collider*. https://home.cern/science/accelerators/future-circular-collider. Accessed: 2025-07-09. 2025.

[30] CERN Courier. "FCC: The physics case". In: *CERN Courier* (2021). Accessed: 2025-07-10. URL: https://cerncourier.com/a/fcc-the-physics-case/.

[31] J. J. Sakurai and Jim Napolitano. *Modern Quantum Mechanics*. 3rd ed. Cambridge University Press, 2020.

[32] Rami Mehrem. *The Plane Wave Expansion, Infinite Integrals and Identities involving Spherical Bessel Functions*. 2011. arXiv: 0909.0494 [math-ph]. URL: https://arxiv.org/abs/0909.0494.